Instabilities in Arrays of Coupled SQUIDs

J.W. Dunstan

Department of Physics
Royal Holloway University of London

September 2019

A thesis submitted in partial fulfilment for the degree of Doctor of Philosophy

Declaration

I confirm that the work presented in this thesis is my own. Where information has been derived from other sources, I confirm this has been indicated in the thesis.

J.W. Dunstan

Abstract

Previous work [1] on chains of RF SQUIDs has exposed repeatable hysteretic jumps in the frequency modulation curve. In this thesis we show that this may be explained by a nearest neighbour interaction between the SQUIDs in the chain. Further modelling shows that these jumps arise from hysteresis in the flux configuration of the array. This hysteresis may be present even for $\beta_{\mathrm{L}} < 1$.

We find that the behaviour of each SQUID is dependent on its position within the array even for an array of identical SQUIDs. Studies of the behaviour of different length arrays shows qualitatively different behaviour for different array lengths. We explore the sensitivity of the array to deviation in SQUID parameters such as loop area and critical current in different coupling regimes. We show that the effect of the coupling may be alleviated by the increasing the loop inductance of the SQUIDs away from the array edge.

Subsequently, we present the results of an experiment designed to provide clearer data in order to understand the effect of the coupling. The sample consisted of a short nanoSQUID array in a resonator. Comparisons to the theory show some agreement, although the nanoSQUIDs exhibited a high degree of hysteresis in the current phase relation at both milliKelvin temperatures and temperatures approaching T_{c}.

Acknowledgements

I would like to thank Professor Phil Meeson for the opportunity to work in his research group at RHUL. I would like to thank the people who helped with my work, including Dr Connor Shelly, as well as my fellow Ph.D. students; Tom Dixon, Katie Porsch and, in particular, George Long. My time at RHUL would not have been as enjoyable without the attendants of 3 o'clock tea. They know who they are. I would also like to thank the people in the RHUL physics department for creating a pleasant environment in which to work.

I would also like to thank Esther Lewis for her support.

Contents

List of Figures

Chapter 1

Introduction to the Field and the Thesis

The development of quantum technologies is necessarily dependent on the detection of the state of a qubit, often via photon detection. To achieve this an incoming weak signal must interact with a nonlinearity in order that it be either directly amplified or stimulate a secondary detectable signal. In a superconducting architecture the most common nonlinearities are the Josephson junction and the nanobridge [2], neglecting for a moment the nonlinear kinetic inductance of the superconductor itself [3]. Both Josephson junctions and nanobridges can be implemented either directly or put into a superconducting loop to form a SQUID. The SQUID geometry has the advantage of being tuneable by an applied magnetic field.

Placing the nonlinear element into a resonator allows for the interaction time between photon and nonlinearity to be increased. The increased interaction time can be used to improve sensitivity at the expense of measurement speed and bandwidth. The greater sensitivity allows for precise measurements of the functional form of the nonlinearity.

It is common to fabricate samples in which the nonlinear elements are grouped in arrays. This design can be useful for many reasons, including the development of metamaterials, where an incident wave is modulated on a scale less than the wavelength [4], or for parametric amplifiers [5]. It is therefore important to understand how these elements behave both separately and collectively. In our work the nonlinear element employed is the RF SQUID.

An array of interacting SQUIDs has potential applications in the development of quantum simulators [6] and metamaterials [4, 7, 8, 9, 10, 11]. Understanding how the coupling strength depends on the spacing of the SQUIDs is also important for the design and engineering of future superconducting

devices that aim to exploit the high nonlinearity of an array in applications such as photon detectors.

The first of these applications; quantum simulators, is a field of much current interest since it presents an opportunity to deepen our understanding of quantum mechanics by performing simulations that are not feasibly achievable in classical systems. A quantum system has a number of degrees of freedom that scales exponentially with the number of particles [12, 13].

Quantum simulators were first proposed in 1982 Feynman [14], who argued that a quantum system with controllable parameters could be used to model the behaviour of a more complicated quantum system since it would have access to an exponentially scaling number of degrees of freedom, thus avoiding the exponential resource blow-up encountered in a classical system. This idea led to the birth of the field of quantum computing which allows access to a range of algorithms, exploiting the quantum effects of entanglement and superposition. These algorithms include Grover's and Shor's algorithms, which are not achievable classically [12]. A classical computer is not a universal Turing machine, since it can only run a subset of possible algorithms.

The second notable application is in the development of technologies based on metamaterials. In a classical case a metamaterial is a material that is engineered to have properties that are not observable in nature. These properties include bending waves to achieve sub-wavelength focusing or to create invisibility cloaks and creating media with negative refractive index and hyperbolic dispersion [15]. This can be achieved by periodically modulating a wave on a scale smaller than the wavelength.

A quantum metamaterial is the extension of a classical metamaterial into the quantum regime. The optical properties of a quantum metamaterial are described by both Maxwell's equations and the Schrödinger equation. Quantum metamaterials are comprised of quantum coherent unit elements which can be directly controlled. The global coherence must be maintained for the duration of the electromagnetic pulse [7, 11]. A one dimensional quantum metamaterial can be formed of an array of qubits in a transmission line [11]. Quantum metamaterials have applications in lasing [11] and single photon detection [8] as well as exhibiting phenomena such as superradiance [10].

Recent parametric amplifier designs [5, 16, 17, 18] employ arrays of SQUIDs in order to amplify an incoming weak signal. The incoming weak signal interacts with a nonlinearity causing it to mix with waves at other frequencies. This wave mixing allows for amplification.

Performing a binomial expansion of the nonlinearity allows us to examine the dominant mixing processes. If the quadratic term is dominant we will observe three wave mixing. Similarly, the cubic

coefficient relates to four wave mixing. Of these regimes the three wave mixing regime is favourable, in part due to its inherently greater wave-nonlinearity interaction [19].

The choice of SQUIDs over other nonlinear elements, such as Josephson junctions, allows the nonlinearity to be biased by an externally applied magnetic field. Biasing the system allows the symmetry of the nonlinearity to be tuned. Tuning allows us to alter the ratio of the quadratic and cubic coefficients in order to operate in the three wave mixing regime.

Three wave mixing is where the pump frequency is at approximately twice the signal frequency,

$$\omega_{\mathrm{p}} = \omega_{\mathrm{s}} + \omega_{\mathrm{i}}, \tag{1.1}$$

where ω_{p} is the pump frequency, ω_{s} is the signal frequency and ω_{i} is the frequency of the idler tone. The idler tone is generated as a consequence of energy conservation [20]. Since the pump tone is well separated from the signal tone it may be filtered out of the subsequent measurement effectively.

As a consequence of momentum conservation we obtain the phase matching condition

$$\boldsymbol{K}_{\mathrm{p}} = \boldsymbol{K}_{\mathrm{s}} + \boldsymbol{K}_{\mathrm{i}}, \tag{1.2}$$

where $\boldsymbol{K}_{\mathrm{p,s,i}}$ corresponds to the wave-vectors of the pump, signal and idler. This condition is satisfied in a non-dispersive medium [20]. For maximum gain the waves should remain coherent. In real mediums chromatic dispersion means that this is not possible. Therefore dispersion engineering is often necessary. Dispersion engineering limits the operable bandwidth of devices. In the three wave mixing regime the gain is dependent on the quadratic nonlinearity and the phase matching is dependent on the cubic nonlinearity. The coefficients can therefore be independently [5] tuned, reducing the need for dispersion engineering.

In SQUID array based devices the precision of tuning is important, since it dictates the mixing conditions. Therefore it is important to fully understand the behaviour of SQUID arrays coupled to a transmission line.

We have explored the behaviour of a resonator containing an array of closely packed RF SQUIDs. Because the SQUIDs were closely packed the mutual inductance between them is non-negligible. Closely packing the SQUIDs gives a concentrated region with an increased nonlinear inductance.

The nonlinearity mediates the interaction between the between selected modes of the resonator, as is necessary for the period doubling bifurcation style detector [21], and useful for parametric amplifiers [22]. Measuring the frequency modulation curve of this resonator exposed some unexpected results; the curve exhibited repeatable and power independent hysteretic jumps even for SQUIDs with a dimensionless inductance, β_{L}, less than unity. This behaviour is in contrast to the expected behaviour of SQUIDs, which is reviewed in section 2.4. These jumps could be explained by accounting for the interaction between the magnetic moments (or circulating currents) of adjacent SQUIDs. This interaction allows energy to be stored in the magnetic field, and means that at given flux bias points there may be multiple metastable states of the flux configuration of the array. The jumps can then be thought of as the energy changing between the interacting moments and the SQUID.

The effect of the interaction between neighbouring SQUIDs in arrays is currently not well understood. Recent work considers long arrays of noninteracting SQUIDs [23, 24, 25], whilst avoiding the inductive interaction between adjacent SQUIDs. Other work neglects the edge effect, an approximation only valid for long arrays [22]. Our approach differs from this in that we study the modification to the nonlinear inductance created by the introduction of the coupling. We study the dependence of the resulting behaviour on the array length.

This thesis will describe modelling and measurements of the inductance of coupled RF SQUID arrays. An overview of the background physics is given as a starting point. The modelling work arises due to previous experimental work at RHUL, an overview of which is given in section 2.7.2. In these measurements some unexpected effects were observed.

Chapter 3 describes a separate experiment on a sample containing well separated, uncoupled SQUIDs. The measurements were performed by a previous student. Subsequent modelling performed by me allows us to use this data to quantify the homogeneity of the magnetic field used to bias the SQUIDs. This is necessary for our understanding of the physics in the case of coupled SQUID arrays, and is useful in order to contrast the behaviour of coupled and uncoupled SQUIDs.

A model for the behaviour of the coupled SQUIDs is given in chapter 4. This is extended to make predictions about the flux configuration of the array in chapter 5. In chapters 6 and 7 we describe further measurements performed to better evaluate the model.

The appendix A serves as a manual for the code built by me in order to perform the measurements described in this thesis. The appendix B gives the python code used in the numerical simulations.

Chapter 2

Review of the Basic Theory

Nonlinear superconducting systems underpin the work presented in this thesis. As such, this chapter will review the basic theories. The nonlinear elements described in this work are the Josephson junction and the nanobridge. These may be connected in parallel configurations to allow for the creation of SQUIDs.

2.1 Superconductivity

Superconductivity is a phenomena whereby some materials exhibit both perfect conductivity and perfect diamagnetism at temperatures below some material dependent critical temperature.

The origin of the behaviour lies in a small attractive force between electrons in the material. The force is the result of an electron-phonon interaction. Regardless of the strength of the electron attraction some electron pairs will form. The pairs are called Cooper pairs. The paired electrons will have opposite spins. Since a pair will have integer spin, it will behave as a boson rather than a fermion, and therefore will not obey the Pauli exclusion principle. Therefore pairs may occupy the same quantum state. This allows for the formation of a gap in the energy states of the Cooper pairs. At sufficiently low temperatures the Cooper pairs will sit in an energy state below the energy gap. This means there is a minimum collision energy required to break the pair. The energy gap inhibits normal resistivity [26].

Since the Cooper pair condensate consists of bosons, which are indistinguishable, the wave function describing them will extend throughout the media in a globally quantum coherent manner [26]. This coherence allows us to construct circuitry containing many electrons that behave in a coherent quantum

mechanical manner.

The Ginzburg-Landau theory has been shown to be a limit of the BCS theory [26]. The Ginzburg-Landau theory is based on the theory of second order phase transitions. It describes the motion of the centre of mass of the superconducting electron pairs using a pseudo-wavefunction, ψ, representing the order parameter. By minimising the free energy of the field they derived an expression akin to the Schrödinger equation, but with added nonlinear terms [26].

2.2 Josephson Junctions

The Josephson effect was predicted in 1962 by B.D. Josephson [27]. The Josephson effect is a manifestation of the fundamentally quantum phenomenon of tunnelling exhibited at a macroscopic scale. There is a nonlinear interaction of the superconducting condensates either side of the junction. The nonlinear inductance of the Josephson junction underpins most of the work in the field of superconducting devices. Applications include parametric amplification [3, 5, 22, 28], bifurcation based photon detection [21, 29, 30] and qubit design [31, 32], amongst many others.

Josephson junctions are formed of 2 layers of superconducting material joined by an insulating or normal metal link. Cooper pairs are able to tunnel through the weak link, leading to some non-classical phenomena. The behaviour of a Josephson junction in the absence of an applied voltage is described by the DC Josephson effect. The AC Josephson effect describes the behaviour of the junction under the application of a potential difference across the barrier.

Since the wave function is continuous and smooth throughout the medium, upon interaction with a barrier the solution to the Ginzburg-Landau equation is one of exponential decay. Here we have assumed the barrier to be of uniform height. The exponential decay results in an amplitude difference between the wave-functions either side of the junction. A current, I, proportional to the phase difference, δ, will flow through the junction with no potential difference:

$$I \propto \delta \tag{2.1}$$

In the A.C. Josephson effect, the Josephson junction will oscillate at a frequency proportional to the

potential difference across it:

$$\omega_{\mathrm{J}} = \frac{2e}{\hbar}\Delta V. \tag{2.2}$$

The Josephson equations are [27],

$$I(t) = I_{\mathrm{c}} \sin(\delta(t)), \tag{2.3}$$

$$\Delta V(t) = \frac{\hbar}{2e}\frac{\partial \delta(t)}{\partial t}, \tag{2.4}$$

where I_{c} is the critical current of the junction and e is the electron charge. They can be found by ensuring continuity of the wave function and its derivative across the boundaries [26]. The AC Josephson effect corresponds to the tunnelling of a Cooper pair across the barrier with photon emission. The DC effect describes tunnelling without photon emission [27].

The Josephson junction has a nonlinear inductance. This can be found from the Josephson relations. Inductance, L, is defined as

$$\Delta V(t) = L\frac{\partial I}{\partial t}, \tag{2.5}$$

where $\Delta V(t)$ is the potential generated and I is the current through the inductor. Equating equation 2.5 with equation 2.4 gives

$$L\frac{\partial I}{\partial t} = \frac{\hbar}{2e}\frac{\partial \delta(t)}{\partial t}. \tag{2.6}$$

Using equation 2.3 we find

$$\frac{\partial I}{\partial t} = \frac{\partial \delta(t)}{\partial t} I_{\mathrm{c}} \cos(\delta(t)). \tag{2.7}$$

Substituting equation 2.7 into equation 2.6 and rearranging yields the Josephson inductance, L_{J},

$$L_{\mathrm{J}} = \frac{\Phi_0}{2\pi I_{\mathrm{c}} \cos(\delta)}, \tag{2.8}$$

where $\Phi_0 = \dfrac{h}{2e}$ is the magnetic flux quantum.

2.3 Weak Links

A weak link is formed when two superconducting electrodes are connected by conductive materials. Weak links differ from tunnel junctions in that the conduction is not reliant on tunnelling phenomena.

Like a tunnel junction weak links have a nonlinear current phase relationship. As such they can be used for applications such as parametric amplification [33].

Weak links can be formed by in many ways, including sandwiching normal conductors between superconducting electrodes, suppressing superconductivity in part of the superconducting wire or narrowing the wire [34]. Superconductivity may be suppressed either by using the proximity effect by putting a normal metal close to the superconducting wire or by ion doping. A narrowing of the wire in a Dayem bridge pattern [34] relies on the increased current density to approach the critical current density in a region of the superconductor. These constriction based structures are called nanobridges. They may have uniform or varied film thickness. It has been shown that variable thickness bridges may have some favourable current phase characteristics [35].

An advantage of the nanobridge structure is the ease of fabrication. Rather than the multilayer or oxidation processes typically involved in tunnel junction fabrication, nanobridges may be fabricated using either electron beam lithography and reactive ion etching or focussed ion beam lithography to thin a section of a superconducting wire.

Nanobridges have been inserted into superconducting loops to form nanoSQUIDs [35, 36]. An advantage of nanoSQUIDs over SQUIDs based on tunnel junctions is that due to the nanoSQUID size, the flux focussing arising from the Meissner effect can be minimised, resulting in better flux coupling. The terminology nanoSQUID will be used to refer to a SQUID containing a nanobridge.

The weak links relevant to this work are the nanobridges. The remainder of this section therefore will focus on such constriction based weak links.

Since nanobridges are not reliant on tunnelling, their behaviour is expected to be distinct from that of tunnel junctions. It has been shown that variable thickness bridges of a length less than the coherence length will have current phase relationships most akin to conventional tunnel junctions [34, 35, 37]. To exhibit an approximate sinusoidal current phase relationship the effective length of the nanobridge should be smaller than the coherence length, ξ, of the superconductor. The effective length, l_{eff}, is the length over which the current concentration is greater than half of its maximum value [34]. The effective length describes the nonlinear region of the superconducting wire. In general this is longer than the bridge length.

In BCS theory the coherence length scales with temperature according to,

$$\xi(T) = \frac{\xi(0)}{\sqrt{1 - T/T_{\mathrm{c}}}}, \tag{2.9}$$

where T_{c} is the critical temperature of the superconductor [26], $\xi(0) = \sqrt{\xi_0 l_{\mathrm{mf}}}$, l_{mf} is the mean free path and ξ_0 is the coherence length at $T = 0$. The temperature dependence of the coherence length means that the nanobridges have a finite temperature window in which they can be well described by the short bridge theory. For niobium $\xi_0 = 38\,\mathrm{nm}$ [38].

The current phase relationship for a short bridge in the dirty limit was derived by I.O. Kulik and A.N. Omel'Yanchuk in 1975 [39]. It is given by,

$$I(\delta) = \frac{\pi\Delta}{eR_{\mathrm{N}}} \cos\left(\frac{\delta}{2}\right) \operatorname{arctanh}\left[\sin\left(\frac{\delta}{2}\right)\right], \tag{2.10}$$

where R_{N} is the normal state resistance, Δ is the superconducting gap and e is the electron charge. This will be referred to as the KO-1 theory. The structure is described as dirty if the mean free path is much less than the effective constriction length, $l_{\mathrm{mf}} \ll l_{\mathrm{eff}}$. This condition tends to be satisfied. The mean free path is limited by diffuse scattering from the film surface [34].

The KO-1 theory comes from neglecting all but the gradient term of the Usadel equations [34,39,40]. This approximation is valid providing that the bridge is sufficiently small.

The KO-1 theory can be used as a limit describing ideal operation of a superconducting weak link.

Where the coherence length and the scale of the nanobridge are not comparable the current phase relationship may become approximately linear and highly hysteretic [37].

In general the current phase relationship is highly sensitive to the geometry of the bridge. It is possible to numerically solve the Usadel equations for the geometry of the bridge [35]. This has been done by Vijay et al. [37] for a range of bridge geometries. Their results are shown in figure 2.1. Their model shows that the current phase relationship for uniform thickness bridges of width 0.75ξ does not approach the KO-1 limit, even down to lengths of $20\,\mathrm{nm}$. The longer the bridge the more linear and hysteretic the current phase relationship becomes. They have been able to alleviate the hysteresis to some extent by thickening the electrodes connecting to the bridge. Nanobridges with thickened electrodes will be referred to here as 3D bridges.

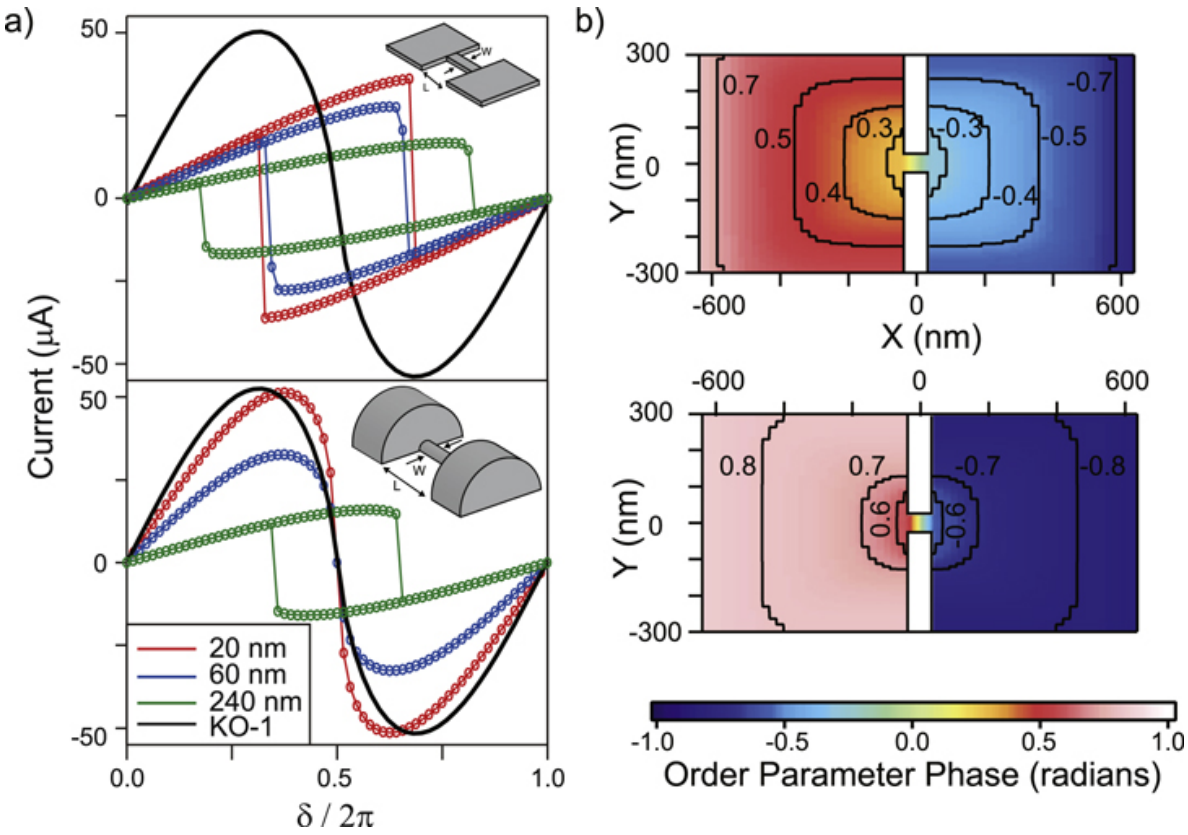

Figure 2.1: a) The modelled current phase relations for nanobridges of different lengths. The top and bottom panel correspond to 2D and 3D bridges respectively. The current phase relation for the 3D bridges resembles the KO-1 curve (black line) most closely. b) The phase across the bridge for 2D and 3D bridges. In the 2D bride the phase drop is not well localised to the bridge. Taken from [35].

As well as the hysteresis in the current phase relation, figure 2.1 also shows that the phase drop of a 2D bridge is not well localised to the bridge. This means that the length of the junction becomes poorly defined [35]. This is illustrated in figure 2.1. In a sufficiently small SQUID geometry the delocalisation of the phase drop may result in interference between the bridges. The localisation of the phase drop can be improved by thickening the electrodes connecting to the bridge. The thickened electrodes are modelled as half-cylinders of radius $300\,\mathrm{nm}$ [37]. This can be achieved by employing a double angle material deposition using an appropriate mask and angle such that the second evaporation lands only on the walls of the resist mask defining the constriction whilst still landing on the electrodes.

In long bridges, where the phase drop in the constriction is comparable to that in the electrodes it is possible to model the current phase relationship of a DC nanoSQUID considering only flux quantisation and neglecting the Josephson effect [41]. This produces a triangular current phase relation centred on 0 applied flux. This has been shown experimentally by Faucher et al [42].

At low temperatures the nanobridges exhibit a thermal hysteresis distinct from the electrical hysteresis. As the critical current is passed the bridge becomes resistive. This leads to power dissipation in the bridge creating a hotspot. The hotspot is maintained by continued dissipation in the bridge. The current must then be lowered to a current at which the bridge becomes superconducting again. This current is called the re-trapping current. It is generally lower than the critical current [43]. At sufficiently high current the heating will cause the superconductivity of the whole loop to be lost. This is called the heat saturation current. If the heat saturation current is low then it will limit the power range over which the device can operate [43].

It is possible to decrease the thermal hysteresis by capping the bridges in a layer of normal metal. This helps reduce hotspot generation. It also limits the McCumber parameter therefore reducing electrical hysteresis [36]. Typically the caps are fabricated from gold or tungsten.

Another consideration in the design of nanobridges is the ratio of the electrode to the constriction width. If the electrodes are more than 2-3 times the width of the constriction, eddy currents may allow flux vortices to penetrate the bridge [41]. The penetration of eddy currents into the bridge may cause a suppression of the flux modulation depth of a nanoSQUID [42].

Since the coherence length is a function of temperature it is possible to reduce some of the hysteresis by operating the devices within a certain temperature range [2]. The critical current of the nanobridge is more strongly temperature dependent than the re-trapping current. This means that operating at a temperature close to T_c, where the critical current and the re-trapping current are close, will also help to reduce thermal hysteresis [2].

In principle, nanobridges present an easy to fabricate alternative to Josephson junctions. In practice however, they are likely to exhibit both electrical and thermal hysteresis. In order to reduce thermal hysteresis it is possible to add a cap of normal metal to the bridge to aid in power dissipation. Electrical hysteresis may be alleviated by fabricating short 3D bridges, where the electrodes undergo an additional evaporation step in order to thicken them with respect to the bridge. Such bridges are well described by the KO-1 theory.

2.4 SQUIDs

Embedding a Josephson junction or a weak link in a superconducting loop allows the junction to be biased by an externally applied magnetic field. This system is called a SQUID. The ability to bias with an externally applied magnetic field as opposed to a DC current is a useful feature if the element is embedded in a resonator, where DC currents are reflected by the input capacitor. This section will focus on RF SQUIDs, which contain a single Josephson junction shorted by a superconducting loop. The generalisation of the theory outlined in this section to describe SQUIDs containing weak links is achieved by substituting the Josephson current phase relation for that of the weak link.

A superconducting wavefunction exists in the superconducting material. Ensuring the condensate wavefunction is single valued results in a phase quantisation condition given by [26, 44]

$$\delta + 2\pi \frac{\Phi_{\text{int}}}{\Phi_0} = 2\pi n, \tag{2.11}$$

where δ is the phase drop across the junction, Φ_{int} is the total flux in the loop.

The phase drop, δ, across the junction results in a super-current, I,

$$I = I_{\text{c}} \sin(\delta) = -I_{\text{c}} \sin\left(2\pi \frac{\Phi_{\text{int}}}{\Phi_0}\right). \tag{2.12}$$

Combining equations 2.11 and 2.12 allows us to relate the field applied to the loop, Φ_{ext}, to the flux inside the loop,

$$\Phi_{\text{int}} = \Phi_{\text{ext}} - L_{\text{g}} I_{\text{c}} \sin\left(2\pi \frac{\Phi_{\text{int}}}{\Phi_0}\right), \tag{2.13}$$

where L_{g} is the geometric inductance of the loop.

It is useful to define the reduced flux, which will be denoted by a lowercase ϕ_x:

$$\phi_x = 2\pi \frac{\Phi_x}{\Phi_0}. \tag{2.14}$$

This allows us to write equation 2.13 in terms of phase as

$$\phi_{\text{ext}} = \phi_{\text{int}} + \beta_{\text{L}} \sin(\phi_{\text{int}}), \tag{2.15}$$

where we have introduced the dimensionless inductance

$$\beta_{\mathrm{L}} = 2\pi \frac{L_{\mathrm{g}} I_{\mathrm{c}}}{\Phi_0}. \tag{2.16}$$

Similarly to Josephson junctions, SQUIDs also have a nonlinear inductance. This is given by [45]

$$L = L_{\mathrm{g}} \frac{\partial \Phi_{\mathrm{int}}}{\partial \Phi_{\mathrm{ext}}} \equiv L_{\mathrm{g}} \frac{\partial \phi_{\mathrm{int}}}{\partial \phi_{\mathrm{ext}}}. \tag{2.17}$$

The geometric inductance of a square, washer-like SQUID may be estimated from the hole area using the empirical expression [46, 47],

$$L_{\mathrm{g}} \approx 1.25 \mu_0 \sqrt{A} \approx \left(1.57 \times 10^{-6}\,\mathrm{Hm}^{-1}\right) \times \sqrt{A}, \tag{2.18}$$

where μ_0 is the permeability of a vacuum and A is the hole area. This expression neglects the junction inductance and the slit inductance, however it gives a reasonable approximation providing the SQUID has comparable height and width. A more rigorous derivation can be performed using Maxwell's equations [48].

2.5 Resonators

A resonator is a system that has a natural frequency of oscillation. In an LC circuit the energy is periodically exchanged between the inductor and the capacitor, thus acting as a resonator. The frequency of the oscillation is given by $\omega = 1/\sqrt{LC}$. The lumped element model of a transmission line describes a transmission line as the summation of infinitesimal LC circuits.

There are may possible geometries of transmission line. This section will discuss the properties of coplanar waveguides (CPW).

2.5.1 Coplanar Waveguides

A CPW is often the favoured type of transmission line for the development of superconducting quantum technologies because they are easily fabricated by optical lithography and because it is straightforward to integrate components into the transmission line where they strongly couple to the propagating

electromagnetic waves [33]. Because they are characterised by properties per unit length the CPW is scalable over different length scales. Because the ground planes shield the centre line from external fields, the CPW geometry does not suffer greatly from radiative losses; the quality factor is limited by dielectric losses [49].

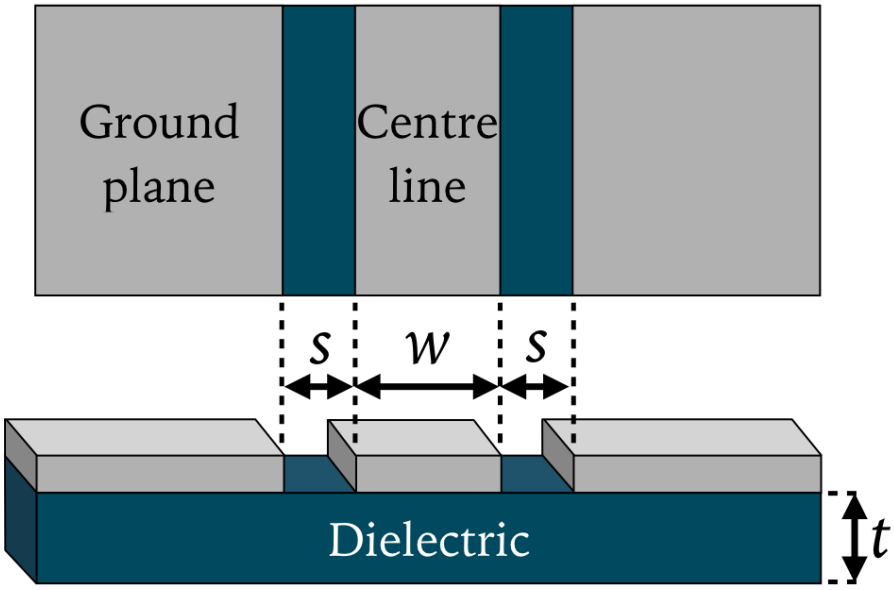

Figure 2.2: Diagram of a CPW transmission line. The top panel shows a top down view. The lower panel shows the side view.

A diagram of a CPW is shown in figure 2.2. The CPW is formed by a conductive centre line of width w separated by a width s from 2 ground planes. These are deposited onto a dielectric substrate of thickness t. This structure supports the propagation of quasi-transverse electromagnetic waves providing that the wavelengths are much greater than the transverse dimensions of the CPW [50].

The speed of light is given by,

$$c = \frac{1}{\sqrt{\varepsilon_0 \mu_0}}, \tag{2.19}$$

where ε_0 is the permittivity of free space and μ_0 is the permeability of a vacuum. In a transmission line constructed of non-magnetic materials with a permittivity of $\varepsilon = \varepsilon_0 \varepsilon_{\text{eff}}$, where ε_{eff} is the effective

permittivity, the phase velocity will be reduced to,

$$\nu_{\text{ph}} = \frac{c}{\sqrt{\varepsilon_{\text{eff}}}}. \tag{2.20}$$

The impedance of a transmission line is normally designed to be $50\,\Omega$. The impedance of a CPW is given by,

$$Z_0 = \sqrt{\frac{L'}{C'}} = \frac{1}{C'\nu_{\text{ph}}} \tag{2.21}$$

where L' and C' are the inductance and capacitance per unit length of the CPW. Conformal mapping techniques [51, 52] allow us to find the inductance and capacitance per unit length. Providing $t \approx s$, these are given by [49, 51, 52],

$$L' = \frac{\mu_0 K(\kappa')}{4K(\kappa)} \tag{2.22}$$

$$C' = \frac{4\varepsilon_0\varepsilon_{\text{eff}} K(\kappa)}{K(\kappa')} \tag{2.23}$$

where $K(\kappa)$ is the elliptical integral of the first kind, $\kappa = \frac{w}{w+2s}$ and $\kappa' = \sqrt{1-\kappa}$. Here we have assumed that the total inductance per unit length is approximately equal to the magnetic inductance. Since the magnetic inductance is typically 2 orders of magnitude larger than the kinetic inductance this assumption is typically satisfied [52]. These expressions can be used to determine the characteristic impedance and phase velocity of the transmission line.

2.5.2 CPW Resonators

If the impedance of a transmission line is not uniform, any incident radiation will be reflected from the impedance mismatch. This reflection results in interference in a manner similar to a Fabry-Pérot interferometer. Therefore, it is possible to define a resonator by interrupting a transmission line by a capacitor at 2 points. The current and voltage distributions for the first three modes of such a system are shown in figure 2.3. There is a $\pi/2$ phase difference between the voltage and the current of each mode. The current distribution has nodes at the capacitors. The second mode has a current node at the centre of the resonator. The second mode will therefore not couple to any inductive element positioned at the centre of the array.

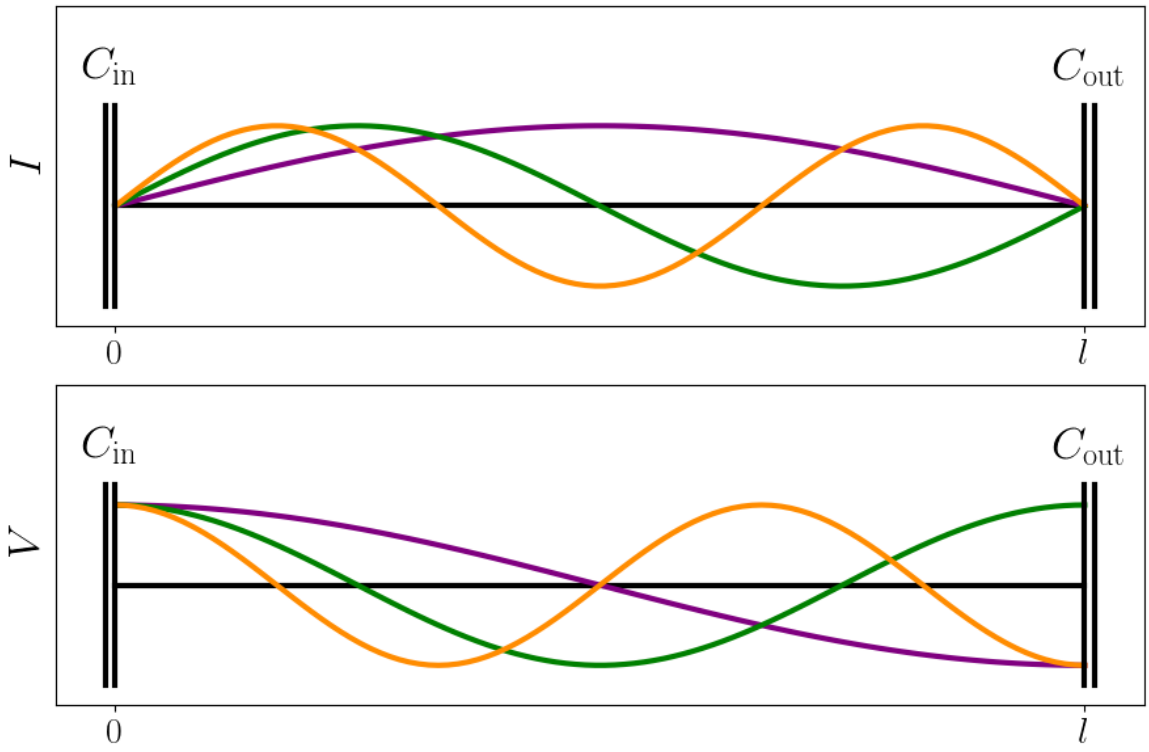

Figure 2.3: The current (top) and voltage (bottom) distributions over the length of a CPW resonator for the first three modes of a resonator with infinite quality factor. The second mode has a current node at the centre of the resonator. The purple, green and orange lines correspond to the first second and third modes respectively.

Since $c = f\lambda$, the condition describing the fundamental resonance of a CPW resonator is given by,

$$f_n = \frac{n\nu_{\text{ph}}}{2l} = \frac{n}{2l\sqrt{L'C'}}, \tag{2.24}$$

where n is the order of the mode, and we have used equation 2.21 to write this in terms of the electrical properties of the CPW. At frequencies close to the resonant frequency equation 2.24 can be written in terms of the total inductance, $L_{\text{tot}} = 2L'l/n^2\pi^2$, and capacitance, $C = C'l/2$, of the resonator [49],

$$f_{\text{res}} = \frac{1}{2\pi\sqrt{L_{\text{tot}}C}}. \tag{2.25}$$

Thus we have found expressions for the characteristic impedance, phase velocity, total capacitance and total inductance of a CPW resonator.

2.5.3 Nonlinear Resonators

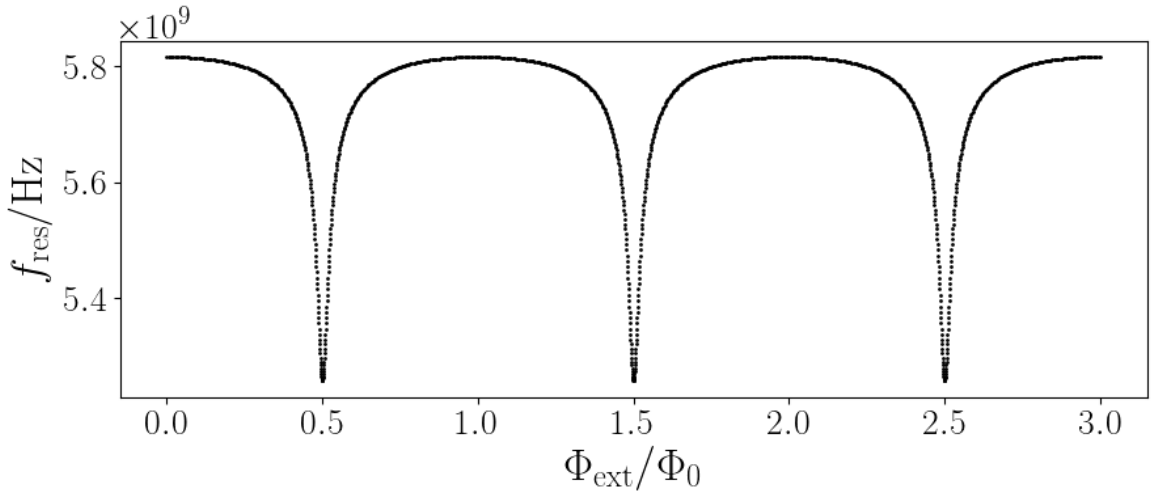

Figure 2.4: A calculated frequency modulation curve for a SQUID in a cavity with f_0=5.9 GHz. In this example the SQUID has $\beta_{\mathrm{L}} = 0.8$ and a participation ratio of $a = 0.017$. This corresponds to a geometric inductance of $L_{\mathrm{g}} = 3 \times 1.11 \times 10^{-11}\,\mathrm{H} = 3.33 \times 10^{-11}\,\mathrm{H}$ and a resonator inductance of $L_{\mathrm{res}} = 6.41 \times 10^{-10}\,\mathrm{H}$.

It is possible to probe the inductance of a SQUID with high precision by embedding it in a CPW resonator. Using a high quality factor superconducting CPW resonator allows the resonant frequency of the oscillator to be precisely measured. The resonator also increases the interaction time between the electromagnetic waves and the nonlinear inductance of the SQUID devices, resulting in an enhanced sensitivity to the nonlinear inductance. Measurements of the resonant frequency of such a system will give a high precision measurement of the inductance of the SQUID due to the increased wave-nonlinearity interaction time.

Substituting equation 2.15 into 2.17 and combining with equation 2.25 gives,

$$\begin{aligned} f_{\mathrm{res}} &= \frac{1}{2\pi\sqrt{L_{\mathrm{res}}C}} \frac{1}{\sqrt{1 + \frac{L_{\mathrm{g}}/L_{\mathrm{res}}}{1+\beta_{\mathrm{L}}\cos(\phi_{\mathrm{int}})}}} \\ &= \frac{f_0}{\sqrt{1 + \frac{a}{1+\beta_{\mathrm{L}}\cos(\phi_{\mathrm{int}})}}}. \end{aligned} \tag{2.26}$$

Figure 2.4 shows the resonant frequency of a resonator containing a SQUID as a function of applied field. The parameters used for the figure have been chosen to correspond to the sample measured in chapter 7. The participation ratio, a, determines the contribution of the SQUID inductance to the total

inductance of the resonator. The participation ratio is therefore a measure of the frequency modulation depth, and hence, the tunability of a resonator.

2.5.4 The Fano Resonance

The amplitude response of a resonant system around each resonant mode is typically characterised by a Lorentzian line-shape. If the discrete transmission state of a resonant system is coupled to a channel allowing transmission of a continuum of states the system will instead be characterised by a Fano resonance [53]. A Fano resonance is asymmetric around the resonant mode [54]. This is in contrast to the symmetric Lorentzian function. The line-shape is described by [55],

$$F(f) = F_0 \frac{\left[q + 2\left(f - f_{\text{res}}\right)/\Gamma\right]^2}{1 + \left[2\left(f - f_{\text{res}}\right)/\Gamma\right]^2}, \tag{2.27}$$

where f_{res} is the resonant frequency, $\Gamma = f_{\text{res}}/Q$ is the line-width, F_0 is a fitting parameter and q is an asymmetry parameter describing the ratio of the discrete and continuous transmission amplitudes.

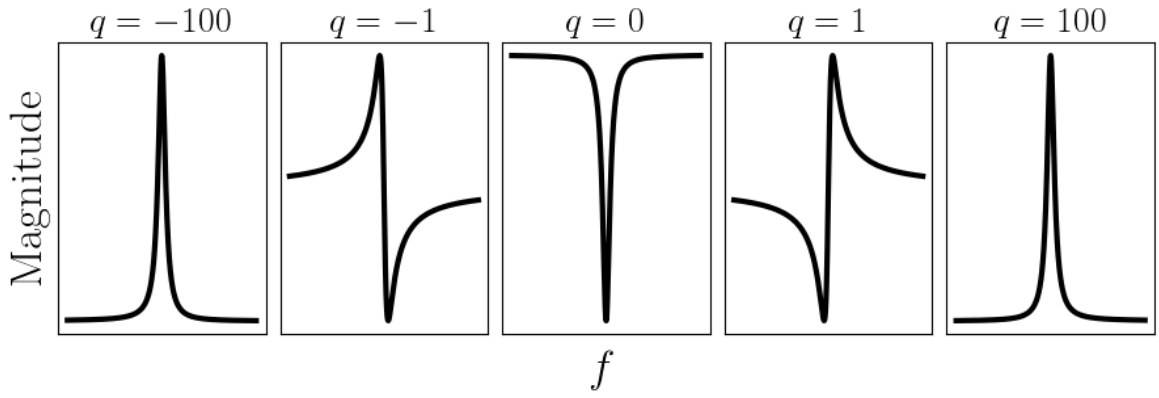

Figure 2.5: Fano resonances plotted for values of asymmetry parameter, q. If $|q| \gg 1$ the transmision is almost purely discrete, resulting in a near Lorentzian line-shape. If $|q| \approx 1$, the transmission of the discrete and continuous channels is comparable and the asymmetry is maximised.

The Fano resonance is plotted for a range of values of q in figure 2.5. The curve is highly asymmetric for values of $|q| \approx 1$. At $|q| \gg 1$ the transmission is mostly through the resonant channel resulting in a near Lorentzian line-shape.

The origin of the coupling to a continuum of states is likely to be poor ground plane uniformity.

2.6 Bifurcations

If a system has two stable states of oscillation it may switch between them. The switching event is called a bifurcation. This section will describe the Duffing bifurcation and the ostensible Volcano bifurcation, both of which were observed in the experiment described in chapter 7.

2.6.1 The Duffing Bifurcation

A Duffing oscillation arises from the introduction of a cubic nonlinearity into the equation of motion of a harmonic oscillator. The equation of motion is given by

$$\ddot{x} = \frac{F}{M}\cos\omega t - 2\Gamma\dot{x} - \omega_0^2 x - \rho x^3, \tag{2.28}$$

where Γ is the damping factor, ω is the drive frequency, ω_0 is the natural oscillation angular frequency, F is the driving frequency, M is the particle mass and ρ is the coefficient of the cubic nonlinearity.

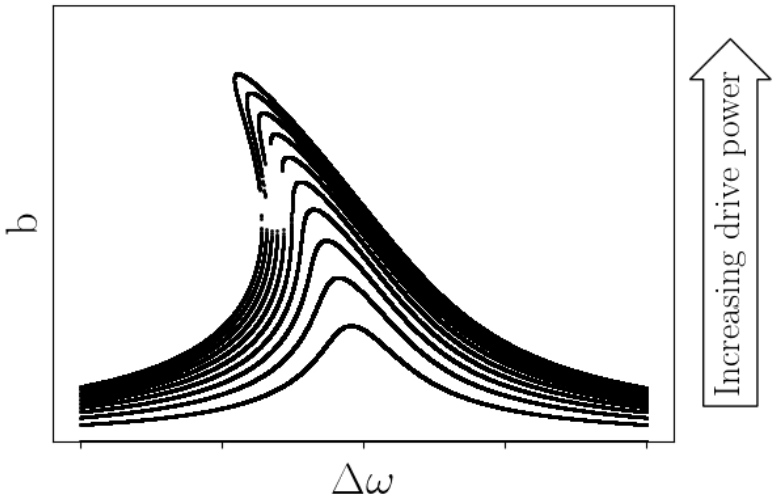

Figure 2.6: Model of the amplitude as a function of detuning from the resonant frequency of an oscillator with a cubic nonlinearity for a range of drive powers. As the drive power is increased the line-shape leans further towards low frequency. The gap in the curve in the unstable state arises due to the algorithm used to numerically solve the amplitude equation.

At frequencies close to the resonant frequency it is possible to solve for the amplitude-frequency relation using perturbation theory [56]:

$$\frac{F^2}{4M^2\omega_0^2} = b^2\left[\left(\Delta\omega - \kappa b^2\right)^2 + \Gamma^2\right], \tag{2.29}$$

where b is the amplitude, $\Delta\omega = \omega - \omega_0$ and,

$$\kappa = \frac{3\rho}{8\omega_0}. \tag{2.30}$$

Figure 2.6 shows the amplitude as a function of frequency for a Duffing oscillator. As the drive power is increased the line shape leans further towards low frequency. At sufficient drive power the line shape has leant sufficiently far that there are multiple possible amplitudes at a given frequency. Two of the states are stable and one is unstable. A change in amplitude state is an example of a bifurcation. The direction of the lean is dependent on the sign of the nonlinear coefficient.

2.6.2 The Volcano Nonlinearity

The volcano nonlinearity is a sudden drop in magnitude around the peak of the resonant mode. The effect has some hysteresis, which is attributed to latching to a non-superconducting state [57]. Since there are not two stable states of oscillation, the volcano nonlinearity is not truly a bifurcation.

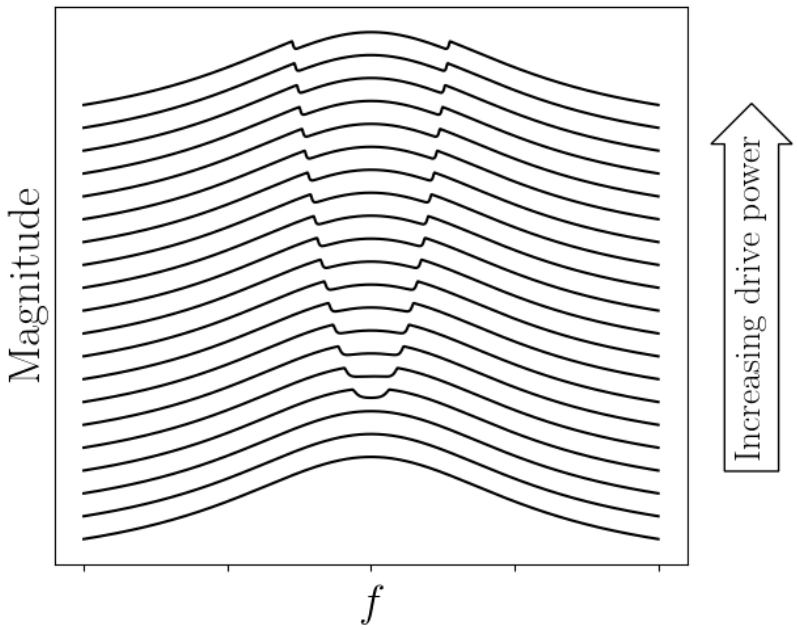

Figure 2.7: Model of the amplitude as a function of detuning of the drive from the resonant frequency. The different curves represent different drive powers. They are separated vertically for clarity. As the drive power is increased the width of the volcano widens.

The volcano nonlinearity is attributed to part of the transmission line becoming dissipative above a

certain power threshold [58]. The dissipation should then obey [58],

$$R = \begin{cases} 0 & \text{for } I < I_{\mathrm{d}}, \\ R_0 \left[1 - \mathrm{e}^{((I_{\mathrm{d}} - I)k)}\right] & \text{for } I > I_{\mathrm{d}}, \end{cases} \tag{2.31}$$

where R_0 and k are fitting parameters, I_{d} is the critical current at which the dissipation begins and I is the amplitude of the current in the resonator. The dissipation has been observed in bare resonators where it was attributed to weak links between the grain boundaries of the superconductor [58].

Figure 2.7 shows the line shape of a volcano nonlinearity. As the power is increased the crater widens, since the critical current of the weak link is exceeded at frequencies further from the resonant frequency.

2.7 Previous Work

Arrays have previously been studied extensively. They have been studied in the context of metamaterials [7], used as nonlinearities for parametric amplifiers [33] and modelled as dipole arrays [59, 60]. In this section we will give an overview of some of the previous work on arrays as well as the experiment performed at RHUL that inspired the work in this thesis.

2.7.1 Josephson Junction Arrays

DC measurements of the IV characteristics of both one [61, 62, 63, 64] and two dimensional [65, 66] have been performed previously. This work is distinct from the work presented in this thesis, since our work probes the inductance of arrays in a resonator using RF currents.

Schematics of one and two dimensional arrays are shown in figure 2.8.

Providing the Josephson inductance is sufficiently large, an array of Josephson junctions may be treated as islands and junctions. It has been shown that such a system will obey a double sine-Gordon equation [23], which has soliton solutions. A charged island will result in the excitation of a charge soliton or anti-soliton. In the superconducting state this may either be an electron or Cooper pair soliton [65].

If the capacitive behaviour dominates the Josephson behaviour of a 1d array, the system may

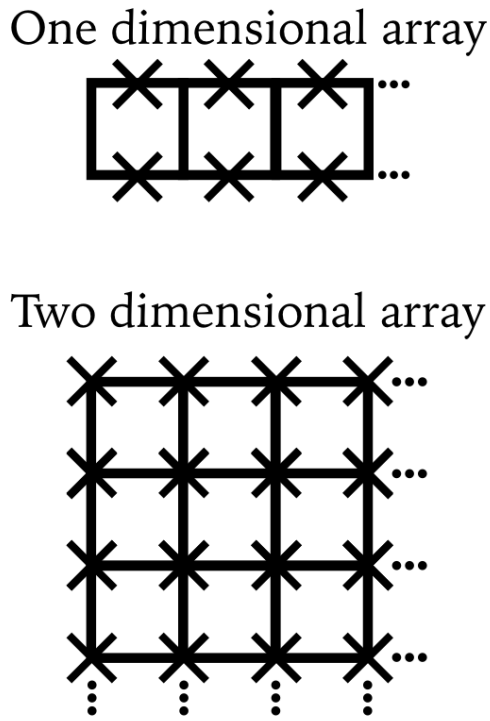

Figure 2.8: Diagram of 1d and 2d arrays of Josephson junctions.

form a Coulomb blockade state. A Coulomb blockade is characterised by a zero current state that exists below a threshold voltage in the IV curve. To avoid thermal excitation the temperature should satisfy $k_{\mathrm{B}}T \ll E_{\mathrm{C}}$, and the junction environment must be high impedance [61]. Once the threshold is passed there is back-bending of the IV curve [64]. The back-bending occurs because the flow is dominated by stochastic quasi-particle tunnelling at low currents, which has a high resistance. At higher currents Cooper pair tunnelling dominates. This effect has a lower resistance [61]. The back bending is illustrated in figure 2.9.

A Coulomb blockade state may form in long Josephson junction arrays even if the Josephson energy dominates the charging energy [64]. In such cases the Coulomb blockade forms because an excess Cooper pair becomes delocalised and acts to screen the potential [68]. The Coulomb blockade behaviour is not solely a property of arrays, it is also observable in single junctions [61, 68].

The transition of the system from a superconducting to an insulating state is interpreted as a quantum phase transition due to the measured resistance being larger for shorter arrays. Modelled according to the XY-model [68], the system undergoes a Berezinskii-Kosterlitz-Thouless transition from a disordered to an ordered state with increasing coupling [59, 61].

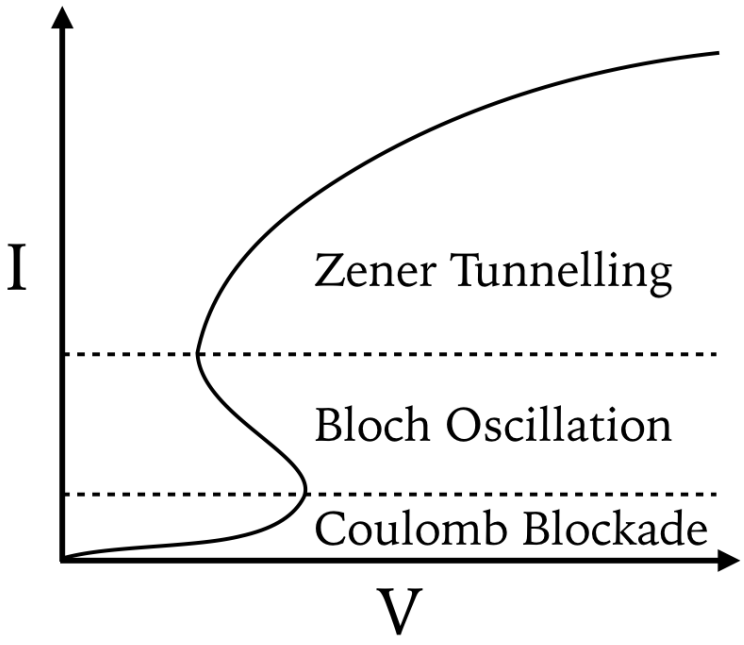

Figure 2.9: A sketch of an IV curve for an array of Josephson junctions. In the Coulomb blockade state the dominant process is quasi particle tunnelling. In the Bloch oscillation region the dominant process is Cooper pair tunnelling, resulting in charge oscillation between $\pm e$. At higher voltages the Zener tunnelling is significant. Adapted from [67].

The Coulomb blockade behaviour appears to present an attractive transistor design for quantum circuits. However, it has been shown [62] that the random charge distribution of the islands in a Josephson junction chain can inhibit the tuning of the Coulomb blockade state.

The canonically conjugate system to charge flow is that of vortex flow [66, 68], which has been studied in 2d arrays of Josephson junctions. Whether charge or flux flow dominates is determined by the ratio of the Josephson coupling energy, E_{J}, to the island charging energy E_{C} [65].

There are two forces determining the dynamics of flux flow through an array, The Magnus effect and flux pinning. If the Magnus force dominates the vortices will propagate at a drift velocity arising from an effective resistance. If flux pinning dominates the flow will be dominated by the tunnelling of vortices through a barrier, or thermal excitation allowing a vortex to jump a barrier. At low temperature tunnelling dominates. It is possible to tune an array into either the flux flow or vortex tunnelling regimes with temperature [66].

At temperatures close to or greater than the critical temperature the flow is dominated by flux

flow, and is therefore linear [66]. When the temperature is reduced the vortex binding energy is increased and the flow is dominated by thermal jumping over barriers. This follows a Boltzmann distribution. The hopping rate is dependent on the frustration of the system, defined as the number of free vortices per cell, $f = Ba_0^2/\Phi_0$ where B is the applied field and a_0^2 is the unit cell area [66]. At very low temperatures Quantum tunnelling dominates the thermal activation. The flow in this regime is temperature independent [66].

Another use of SQUID arrays is to use as leads to perform measurements of the IV characteristic of a Josephson junction [67]. Since the arrays have tuneable inductance it is possible to study the dependence of the IV characteristics of a Josephson junction on its electromagnetic environment. This is possible because it is possible to tune the inductance of the SQUID array leads using an external magnetic field whilst the behaviour of the junction itself is not sensitively dependent on the field. At frustrations of around $\frac{1}{2}$, the single Josephson junction exhibits a Coulomb blockade. Since the Josephson junction is not sensitive to the magnetic field, the Coulomb blockade has arisen due to the inductance of the junction environment.

2.7.2 A Previous RHUL Experiment

This section describes a previous experiment on SQUID arrays at RHUL. The experimental work described in this section was performed by I. Alfaleh [1]. The results of this experiment form the basis of the work in this thesis.

A schematic of the measured sample is shown in 2.10. The sample is a niobium trilayer resonator containing 2 arrays of 32 RF SQUIDs. The arrays are located at $0.55l$ and $0.75l$ along the resonator where l is the resonator length. The SQUIDs have a loop area of $25\,\mu\mathrm{m}^2$. The SQUIDs are designed to have a β_L less than 1 at $4.2\,\mathrm{K}$. The sample was made at PTB and was designed for purposes which are not the subject of this thesis.

The resonant frequency of the resonator was probed as a function of applied field using an external coil. The measurements were performed at liquid helium temperatures in a dilution refrigerator. The resonant frequency was obtained by fitting a Lorentzian function to a forward transmission (S_{21}) measurement performed with a vector network analyser (VNA). The measured curve is shown in figure 2.11. The curve would normally be expected to be smooth and continuous for $\beta_\mathrm{L} < 1$, as illustrated in figure 2.4. Such a plot is known as a modulation curve.

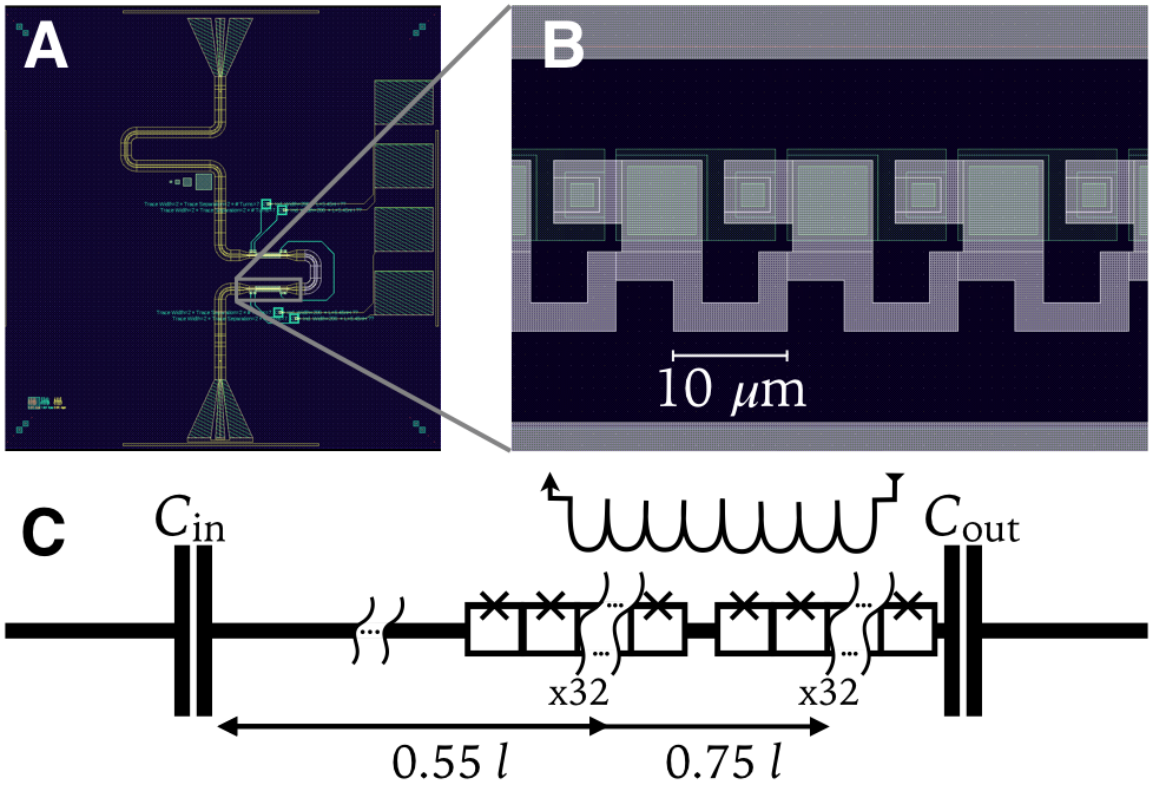

Figure 2.10: A: Layout of the Nb CPW $\lambda/2$ resonator. B: Design of a section of a SQUID array. C: Schematic diagram showing the layout of the measured sample. The ladder pattern ensures that adjacent SQUIDs have a common phase drop along the shared side.

The measured modulation curve exhibits many unexpected features. There are multiple hysteretic jumps which may occur at positions in flux well away from the half flux point. These jumps are repeatable and are robust to thermal cycling. If the jumps were the result of trapped flux vortices, we would expect them to disappear or move with repetition and thermal cycling. It may be expected to observe jumps at fields other than $\Phi_0/2$ if the SQUIDs had $\beta_{\mathrm{L}} > 1$ and if the field inhomogeneity were sufficiently large or if the SQUID loop areas were sufficiently dispersed. The field homogeneity is discussed in chapter 3. It is found to be of the order of 0.5% on the scale of the resonator. This is several orders of magnitude too small to explain the observed phase difference.

The frequency modulation curve also exhibits a modulation effect with a period of many flux quanta. The large period of this beating effect meant that a full period was not observed. The beating

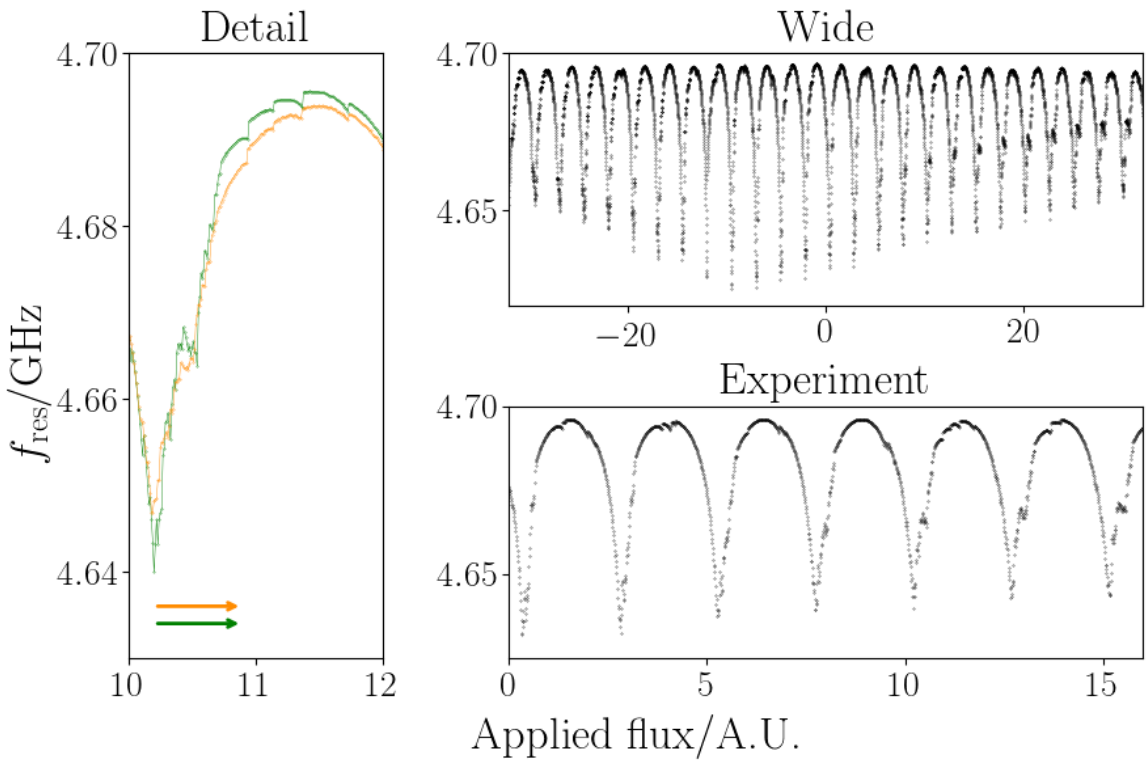

Figure 2.11: The measured frequency modulation curve of a resonator containing 2 arrays of 32 SQUIDs. The curve shows hysteretic jumps. Longer sweeps also show that the amplitude of the modulation varies with field. This is the result of a phase difference between SQUIDs. Left: A zoom showing the detail in the hysteretic features observed in the frequency modulation curve of the resonator. The hysteretic jumps may occur away from the half flux point. Repetition of the sweep (overlaid) shows that the effect is repeatable. Top: A wide view of the sweep shows that the curve also exhibits a beat like effect with a period of many flux quanta. Bottom: A shorter sweep showing the appearance of sub-fringes alongside the modulation curve.

effect is caused by a dispersion in the phases of the SQUIDs. Since the SQUIDs are fabricated in close proximity the field inhomogeneity is again not sufficient to explain these features in the modulation curve.

The effects in this curve can not, therefore, be accurately modelled by considering the SQUIDs according to the current theories. The remaining sections will explore the possible explanations for this behaviour, as well as the further ramifications of the underlying cause of this behaviour.

Chapter 3

A Study of the Homogeneity of the Applied Magnetic Field

In section 2.7.2 we discuss a beating effect observed in the frequency modulation curve of a resonator. A beating effect can be caused by a difference in the flux threading each SQUID loop, resulting in a phase difference between the SQUIDs. This can be caused by either a difference in coupling to the external field between the SQUIDs or by an inhomogeneity in the field produced by the coil. In this section we describe an experiment and model to investigate the field homogeneity further.

The external magnetic flux used to modulate the SQUID inductance in previous and current measurements is produced by a superconducting solenoid mounted on the sample box. The distance between the sample and the solenoid is around $1\,\mathrm{mm}$. Both its diameter and length are approximately $1\,\mathrm{cm}$. This is illustrated in figure 3.1

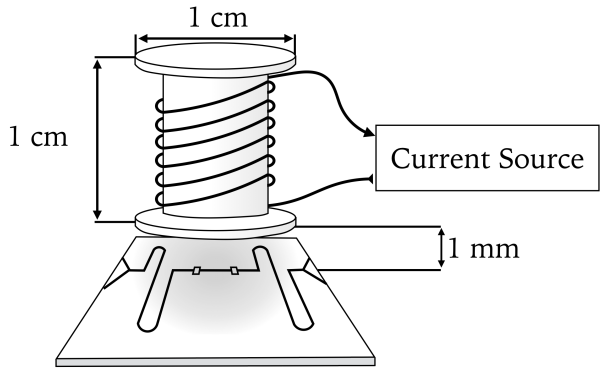

Figure 3.1: Diagram of the solenoid used to flux bias the SQUIDs.

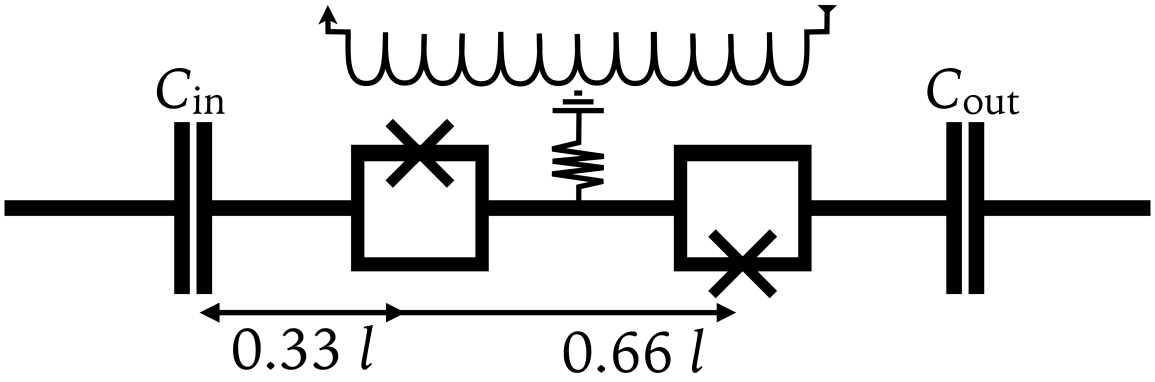

Figure 3.2: Layout of the period doubling resonator. There is a single RF SQUID located at $l/3$ and $2l/3$ where l is the resonator length. The SQUIDs are positioned to give maximum coupling between the first and second modes. The resistor at $0.5l$ is included in order to dampen odd modes. The reversal of the SQUID's orientation accounts for the change in sign of the current of the second mode between the SQUIDs.

The sample measured was a niobium $\lambda/2$ CPW resonator with $f_{\text{res}} = 4.3\,\text{GHz}$. A schematic of the sample is shown in figure 3.2. The sample was fabricated at PTB. The sample contained 2 well separated SQUIDs. The SQUIDs have a loop area of $280\,\mu\text{m}^2$ and β_{L} of 0.7 at $4.2\,\text{K}$. The layout of the sample was designed to observe period doubling behaviour [21]. The measurements were performed by K.E. Porsch [69], whilst I performed all subsequent analysis.

Measurements of the frequency modulation curve of the sample again exposed an unexpected beating effect. This is shown in the top panel of figure 3.3. The beating effect has a period of $207\Phi_0$. We are able to model this by assuming that the flux threading each SQUID is slightly different. We therefore obtain

$$\begin{cases} \phi_{\text{ext}} = \phi_{\text{int}}^{(1)} + \beta_{\text{L}}^{(1)} \sin(\phi_{\text{int}}^{(1)}) \\ \phi_{\text{ext}}(1 + \Delta\phi) = \phi_{\text{int}}^{(2)} + \beta_{\text{L}}^{(2)} \sin(\phi_{\text{int}}^{(2)}), \end{cases} \tag{3.1}$$

where $\Delta\phi$ is the difference in the flux through each SQUID.

We are then able to obtain the inductance and resonant frequency of the sample using equation 2.26. The SQUIDs have a loop area of $280\,\mu\text{m}^2$. This corresponds to $L_{\text{g}} = 26\,\text{pH}$. We then treat the resonator inductance and capacitance as fitting parameters. The lower panel of figure 3.3 shows the resultant frequency modulation curve. The values for L_{res} and C are reasonable. We find that the beating is well described by a field inhomogeneity of 0.482%.

An additional modulation is visible on the underside of the frequency modulation curve. This was

found to be the result of aliasing. Since the troughs in the frequency modulation curve are narrow, the data point density necessary to accurately describe them is high. Therefore the depth of the measured troughs is sensitive to the data point density. In this case the near harmonic relation between the distance between data points and a flux quantum has lead to the observed periodic behaviour. We show that it is possible to reproduce this effect by matching the sampling rate of the theory to that of the experiment.

There is an offset between the phases of each SQUID at zero applied flux. This is caused by trapped flux, indicating that the shielding used was inadequate. The trapped field was found to be $86\Phi_0$. This is taken to be equal to the number of flux quanta between $0\,\mathrm{V}$ and the field at which the SQUIDs are in phase. The earth's magnetic field is of order $5 \times 10^{-5}\,\mathrm{T}$. With a loop area of $280\,\mu\mathrm{m}^2$, we find that this accounts for $7\Phi_0$. Because of the expulsion of magnetic field from superconductors through the Meissner effect the field strength will be increased in the non-superconducting regions. This effect is known as flux focussing. In our sample geometry this accounts approximately for a factor 10 increase in field. Thus the trapped flux is of the order of the strength of the earth's field.

We have quantified the error in loop area of SQUIDs fabricated at RHUL in figure 6.5. For a SQUID of loop area $50\,\mu\mathrm{m}^2$ the deviation was found to be around 2%. The deviation in loop area of SQUIDs fabricated at PTB is unknown. However, assuming a similar absolute deviation to that of the RHUL SQUIDs, the fractional uncertainty will reduce by around an order of magnitude. The difference in the flux through each SQUID therefore is similar to that expected by considering loop area deviation alone.

The field inhomogeneity found by this analysis is not significant enough to explain the beating effect observed in the experiment described in section 2.7.2, nor does it account for the appearance of jumps. If the features were the result of deviation in the SQUID loop area we would expect some Gaussian distribution of loop areas centred around the designed loop area. Over a period of many flux quanta destructive interference between the frequency modulation of the individual curves would result in the measured signal becoming washed out, rather than in the jumps previously discussed. As such, this modelling proves firstly that the coil used to flux bias the SQUIDs is able to produce a sufficiently homogeneous field that loop area deviation dominates the SQUID phase dispersion, and secondly, that the features discussed in section 2.7.2 are not the result of loop area deviation or applied field inhomogeneity alone.

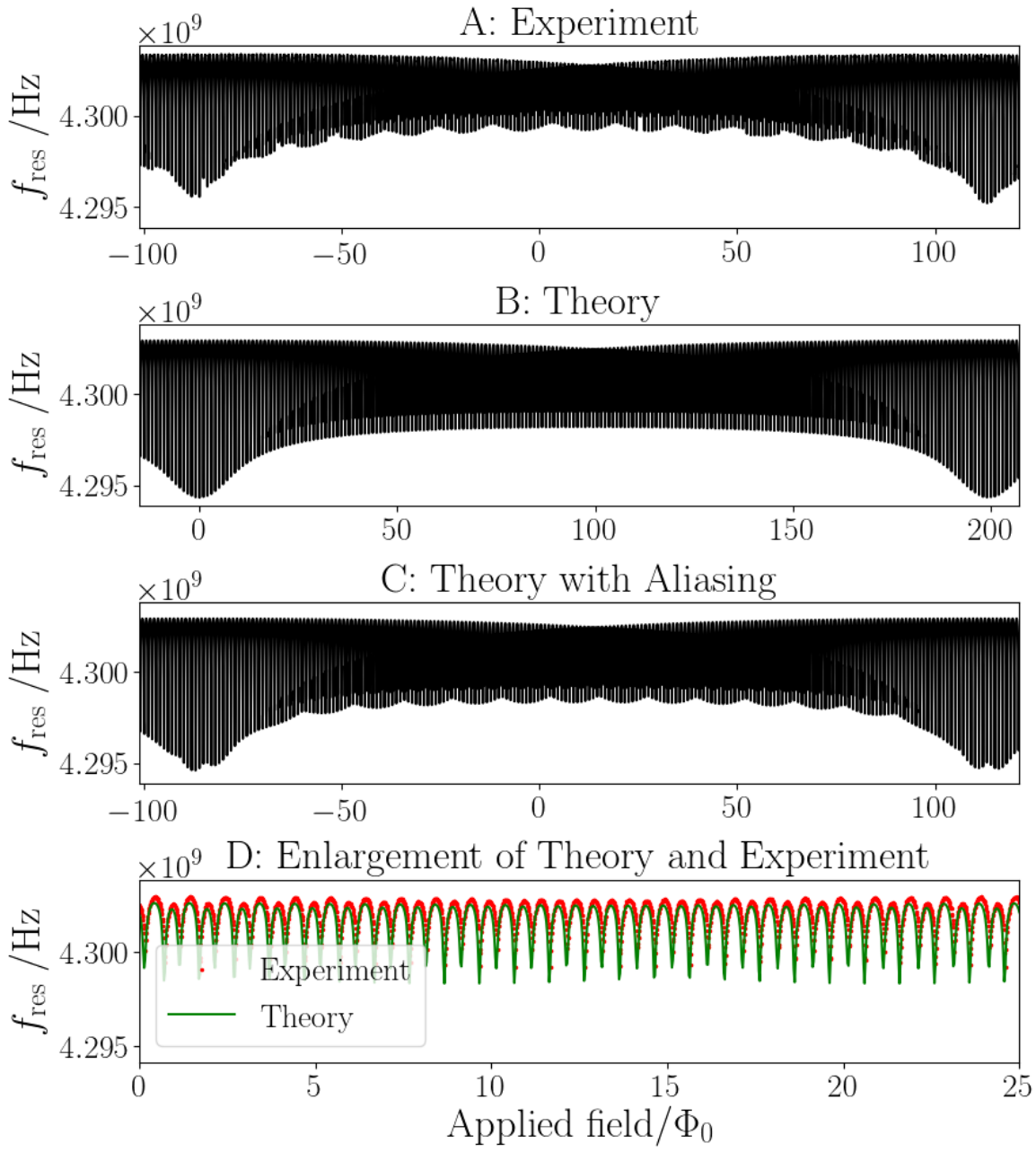

Figure 3.3: A: The experimentally observed flux modulation curve for a sample with an RF SQUID at $\frac{1}{3}l$ and $\frac{2}{3}l$ where l is the resonators length. Due to a small difference in flux threading each SQUID we observe a beating effect. The data for the top panel was taken by K.E. Porsch [69]. B: The theoretical model of the beating effect. This has been plotted for a field inhomogeneity of 0.482%, a resonator capacitance, C_{tot}, of $0.36\,\mathrm{pF}$, an inductance, L_{res}, of $0.15\,\mu\mathrm{H}$ and SQUID dimensionless inductances, $\beta_{\mathrm{L}}^{(1,2)}$, of 0.70 and 0.65. These parameters are reasonable given the resonator geometry. The SQUIDs have a calculated geometric inductance of $26\,\mathrm{pH}$. The non-zero phase of the beating effect at zero flux indicated the presence of trapped flux. This was found to equal $86\Phi_0$. C: The theoretical model of the beating effect. The aliasing effect has been reproduced by matching the sample spacing used in the model to that of the experiment. D: Overlay and enlargement of theoretical and experimental curves.

Chapter 4

Modelling the Frequency Modulation Curve of a SQUID Array

Previously, we have discussed SQUIDs only as separate entities. In this section we show that the behaviour of SQUID arrays may be better understood by considering SQUID arrays as collective bodies where the state of each individual SQUID is dependent on the state of its nearest neighbours. It is shown that this may result in a collective hysteretic behaviour even where individual SQUIDs are fabricated with loop area and critical current such that they would not be expected to exhibit hysteresis. This collective behaviour is observable as jumps in the total inductance of the SQUID array. If the array is embedded in a CPW resonator then the collective behaviour41 will manifest itself as a jump in the resonant frequency akin to that observed in section 2.7.2. We also show that a dispersion of the SQUID phases arises as a natural consequence of the collective behaviour. This collective behaviour is then compared to the hysteretic artefacts observed in the measured frequency modulation curve discussed in section 2.7.2.

4.1 Development of the Model

It is possible to couple RF SQUIDs in an array by patterning them with a shared side as shown in figure 4.1. The overlap of the circulating currents along the shared wire between adjacent SQUIDs requires that the superconducting phase drop along the wire is the same for both SQUIDs. This common phase drop means that the phase drop in adjacent SQUIDs must be considered when calculating the internal

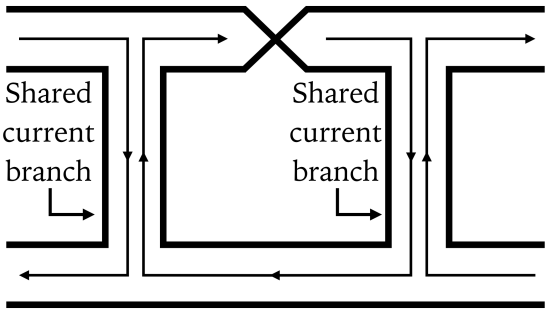

Figure 4.1: Diagram showing the shared current branch between adjacent SQUIDs.

flux in each SQUID.

The phase drop along the shared side between SQUIDs must be equal for each SQUID. The contribution to the phase in an adjacent SQUID is then given by [70]

$$\phi_{\text{int}}^{(i)} = \frac{L_{\text{c}}}{L_{\text{g}}}\phi_{\text{int}}^{(i+1)}, \tag{4.1}$$

where L_{c} is the part of the inductance shared between neighbour SQUIDs.

The transcendental equation relates the applied flux to the flux inside the SQUID loop. For an uncoupled SQUID this is given by [26],

$$\Phi_{\text{ext}} = \Phi_{\text{int}} + L_{\text{g}} I_{\text{c}} \sin\left(\phi_{\text{int}}\right). \tag{4.2}$$

Including the contribution to the current from the neighbouring SQUIDs, equation 4.2 becomes,

$$\Phi_{\text{ext}} = \Phi_{\text{int}}^{(i)} + L_{\text{g}} I_{\text{c}}^{(i)} \sin\left(\phi_{\text{int}}^{(i)}\right) - \frac{L_{\text{c}}}{L_{\text{g}}}\Phi_{\text{int}}^{(i-1)} - \frac{L_{\text{c}}}{L_{\text{g}}}\Phi_{\text{int}}^{(i+1)}. \tag{4.3}$$

for the i^{th} SQUID.

We define $\alpha = L_{\text{c}}/L_{\text{g}}$ and use the reduced flux defined in equation 2.14 to obtain the set of coupled equations [70],

$$\begin{cases} \phi_{\text{ext}} = \phi_{\text{int}}^{(1)} + \beta_{\text{L}}^{(1)} \sin\left(\phi_{\text{int}}^{(1)}\right) - \alpha\phi_{\text{int}}^{(2)}, \\ \phi_{\text{ext}} = \phi_{\text{int}}^{(i)} + \beta_{\text{L}}^{(i)} \sin\left(\phi_{\text{int}}^{(i)}\right) - \alpha\phi_{\text{int}}^{(i-1)} - \alpha\phi_{\text{int}}^{(i+1)}, \\ \phi_{\text{ext}} = \phi_{\text{int}}^{(N)} + \beta_{\text{L}}^{(N)} \sin(\phi_{\text{int}}^{(N)}) - \alpha\phi_{\text{int}}^{(N-1)}. \end{cases} \tag{4.4}$$

These equations must be solved simultaneously numerically. It is possible to use these equations to find the resonant frequency of the SQUID using equations 2.25 and 2.17.

4.2 The Conditions for Hysteretic Behaviour

A SQUID will act hysteretically if the coefficient of the non-linear part of the SQUID equation is larger than that of the linear. If the coupling term, α, is small or if the array contains only two SQUIDs then the SQUIDs will behave the same. This means that we can write equation 4.3 as

$$\phi_{\text{ext}} = \phi_{\text{int}}^{(i)} + \beta_{\text{L}}^{(i)} \sin\left(\phi_{\text{int}}^{(i)}\right) - \alpha\phi_{\text{int}}^{(i)}. \tag{4.5}$$

Rearranging gives

$$\left(\frac{1}{1-\alpha}\right)\phi_{\text{ext}} = \phi_{\text{int}}^{(i)} + \left(\frac{1}{1-\alpha}\right)\beta_{\text{L}}^{(i)} \sin\left(\phi_{\text{int}}^{(i)}\right), \tag{4.6}$$

which results in the frequency modulation curve being functionally unaltered by the coupling with rescaled period and β_{L}. The new approximate limit for the onset of hysteresis is then

$$\beta_{\text{L}} > 1 - \alpha \tag{4.7}$$

for the SQUIDs at the very edge of the array and

$$\beta_{\text{L}} > 1 - 2\alpha \tag{4.8}$$

for the inner SQUIDs. Equations 4.7 and 4.8 mean that a SQUID array may exhibit hysteretic behaviour even if $\beta_{\text{L}} < 1$.

These expressions can be generalised for cases with stronger coupling by splitting the internal flux into a linear and nonlinear component:

$$\phi_{\text{int}}(\phi_{\text{ext}}) = A^{(i)}\phi_{\text{ext}} + B^{(i)}(\phi_{\text{ext}}), \tag{4.9}$$

where $A^{(i)}$ and $B^{(i)}(\phi_{\text{ext}})$ represent an undetermined constant and function respectively. It is assumed

that $B^{(i)}(\phi_{\text{ext}})$ is oscillatory. Substitution of equation 4.9 into equation 4.3 trivially yields

$$\phi_{\text{ext}} - A^{(i\pm1)}\alpha\phi_{\text{ext}} = \phi_{\text{int}}^{(i)} + \beta_{\text{L}}^{(i)}\sin\left(\phi_{\text{int}}^{(i)}\right) - \alpha B^{(i\pm1)}(\phi_{\text{ext}}). \tag{4.10}$$

Thus the term $A^{(i)}$ reduces the field felt by the SQUID and the term $B^{(i)}(\phi_{\text{ext}})$ creates the observed hysteresis. The extension of this calculation for the inner SQUIDs where there are 2 nearest neighbours can be absorbed by the undetermined terms $A^{(i)}$ and $B^{(i)}(\phi_{\text{ext}})$.

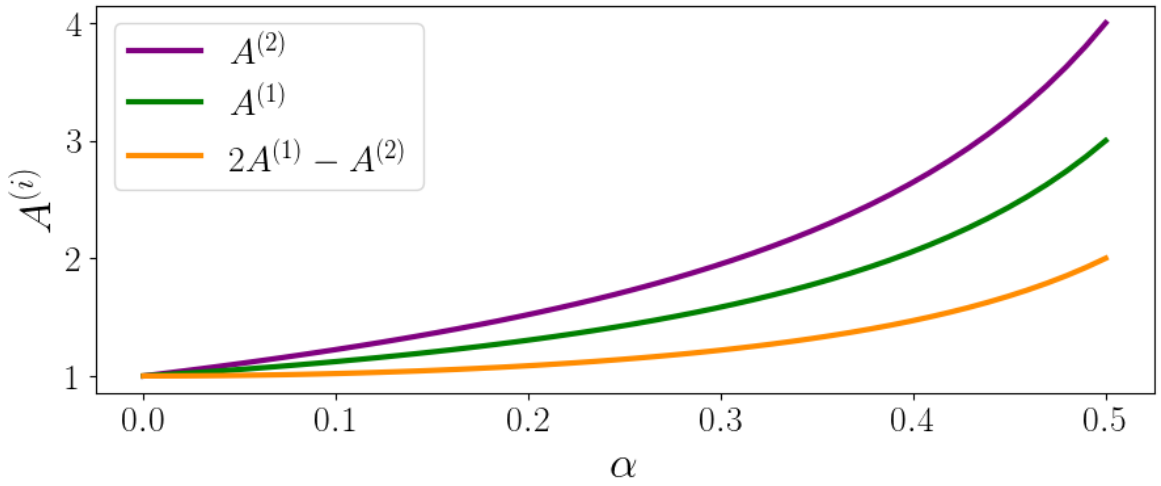

Figure 4.2: The coefficient of the linear part of the function $\phi_{\text{int}}^{(i)}(\phi_{\text{ext}})$, $A^{(i)}$, as a function of coupling strength for a 3 SQUID array for an edge ($i = 1$) and inner ($i = 2$) SQUID. There is a nonlinear increase of $A^{(i)}$ with increasing coupling strength. The difference between the SQUIDs increases with coupling strength. This defines the periodic phase difference between the SQUIDs.

In the case of an array of only 3 SQUIDs it is possible to examine the coefficient $A^{(i)}$ more closely. In order to remove the varying elements of equation 4.4 we average over many periods of flux quanta to obtain,

$$\phi_{\text{ext}} = \overline{\phi_{\text{int}}^{(i)}} - \alpha\overline{\phi_{\text{int}}^{(i-1)}} - \alpha\overline{\phi_{\text{int}}^{(i+1)}} \tag{4.11}$$

where $\overline{x}$ denotes flux-averaged variables. Providing $B^{(i)}(\phi_{\text{ext}})$ is purely oscillatory, we are now able to rewrite equation 4.11 as

$$\phi_{\text{ext}} = A^{(i)}\phi_{\text{ext}} - \alpha A^{(i-1)}\phi_{\text{ext}} - \alpha A^{(i+1)}\phi_{\text{ext}}, \tag{4.12}$$

which requires that

$$k\phi_{\text{ext}} \notin \begin{cases} \left[\sin\left(A^{(i)}\phi_{\text{ext}}\right)\right] / \left[\cos\left(B^{(i)}(\phi_{\text{ext}})\right)\right], \\ \left[\cos\left(A^{(i)}\phi_{\text{ext}}\right)\right] / \left[\sin\left(B^{(i)}(\phi_{\text{ext}})\right)\right], \end{cases} \tag{4.13}$$

where k is an undetermined constant of proportionality. This condition arises from the substitution of equation 4.9 into the sine term of equation 4.4. Comparing the form of equation 4.12 for the inner and the edge SQUID of the 3 SQUID array gives,

$$\begin{cases} \phi_{\text{ext}} = A^{(1)}\phi_{\text{ext}} - \alpha A^{(2)}\phi_{\text{ext}}, \\ \phi_{\text{ext}} = A^{(2)}\phi_{\text{ext}} - \alpha A^{(1)}\phi_{\text{ext}} - \alpha A^{(3)}\phi_{\text{ext}}, \\ \phi_{\text{ext}} = A^{(3)}\phi_{\text{ext}} - \alpha A^{(2)}\phi_{\text{ext}}. \end{cases} \tag{4.14}$$

By symmetry, $A^{(1)} = A^{(3)}$, which gives a set of two simultaneous equations with two unknowns:

$$\begin{cases} 1 = A^{(1)} - \alpha A^{(2)}, \\ 1 = A^{(2)} - 2\alpha A^{(1)}. \end{cases} \tag{4.15}$$

These have the solution

$$\begin{cases} A^{(1)} = \frac{1+\alpha}{1-2\alpha^2}, \\ A^{(2)} = \frac{1+2\alpha}{1-2\alpha^2}. \end{cases} \tag{4.16}$$

This is plotted in figure 4.2.

It is possible to generalise this method to a system of N SQUIDs using matrices. We can write the system of equations 4.14 for N SQUIDs in matrix form as

$$\begin{bmatrix} 1 \\ 1 \\ \vdots \\ \vdots \\ 1 \end{bmatrix} = \begin{bmatrix} 1 & -\alpha & 0 & \dots & 0 \\ -\alpha & 1 & -\alpha & \dots & \vdots \\ 0 & \ddots & \ddots & \ddots & 0 \\ \vdots & \dots & -\alpha & 1 & -\alpha \\ 0 & \dots & 0 & -\alpha & 1 \end{bmatrix} \begin{bmatrix} A^{(1)} \\ A^{(2)} \\ \vdots \\ \vdots \\ A^{(N)} \end{bmatrix}, \tag{4.17}$$

where we have divided through by ϕ_{ext}. This can be expressed compactly as

$$\mathbf{1} = \boldsymbol{\alpha}\mathbf{A}. \tag{4.18}$$

Then

$$\mathbf{A} = \boldsymbol{\alpha}^{-1}\mathbf{1}. \tag{4.19}$$

which can be solved to find $A^{(i)}$ for any length array. The inverse matrix, $\boldsymbol{\alpha}^{-1}$, can be found analytically. The problem can be simplified using symmetry arguments. For instance, the $N = 4$ case can be solved with,

$$\begin{bmatrix} A^{(1)} \\ A^{(2)} \\ A^{(3)} \\ A^{(4)} \end{bmatrix} = \frac{1}{\det(\boldsymbol{\alpha}_4)} \begin{bmatrix} \det(\boldsymbol{\alpha}_3) & \det(\boldsymbol{\alpha}_2)\alpha^1 & \det(\boldsymbol{\alpha}_1)\alpha^2 & \alpha^3 \\ \det(\boldsymbol{\alpha}_2)\alpha^1 & \det(\boldsymbol{\alpha}_2) & \det(\boldsymbol{\alpha}_1)\alpha^1 & \det(\boldsymbol{\alpha}_1)\alpha^2 \\ \det(\boldsymbol{\alpha}_1)\alpha^2 & \det(\boldsymbol{\alpha}_1)\alpha^1 & \det(\boldsymbol{\alpha}_2) & \det(\boldsymbol{\alpha}_2)\alpha^1 \\ \alpha^3 & \det(\boldsymbol{\alpha}_1)\alpha^2 & \det(\boldsymbol{\alpha}_2)\alpha^1 & \det(\boldsymbol{\alpha}_3) \end{bmatrix} \begin{bmatrix} 1 \\ 1 \\ 1 \\ 1 \end{bmatrix} \tag{4.20}$$

where

$$\det(\boldsymbol{\alpha}_n) = \det(\boldsymbol{\alpha}_{n-1}) - \alpha^2 \det(\boldsymbol{\alpha}_{n-2}) \tag{4.21}$$

with $\det(\boldsymbol{\alpha}_1) = 1$ and $\det(\boldsymbol{\alpha}_2) = 1 - \alpha^2$. The notation $\det(\boldsymbol{\alpha}_x)$ refers to the determinant of the x dimensional matrix $\boldsymbol{\alpha}_x$.

For large N the calculation is performed numerically.

We now examine the function describing the hysteresis in the frequency modulation curve. The resonant frequency of the resonator is given by equation 2.25 where L_{tot} is the total inductance, given by the sum of the SQUID inductances, L_i, and the inductance of the resonator, L_{res}:

$$L_{\text{tot}} = \sum_{i=1}^{N} L_i + L_{\text{res}}. \tag{4.22}$$

The inductance of the SQUIDs is found using equation 2.17.

A jump may be identified by setting the derivative of the curve to infinity. Using the chain rule, we find that,

$$\frac{\partial f_{\text{res}}}{\partial \phi_{\text{ext}}} = \frac{\partial f_{\text{res}}}{\partial L_{\text{tot}}} \frac{\partial L_{\text{tot}}}{\partial \phi_{\text{ext}}} = \sqrt{\frac{1}{4CL_{\text{tot}}^3}} \frac{\partial L_{\text{tot}}}{\partial \phi_{\text{ext}}}. \tag{4.23}$$

Equation 4.23 will go to infinity if $L_{\text{tot}} = 0$. If this is the case then f_{res} will also go to infinity. This is

unphysical. Therefore we need only set the derivative of the inductance to infinity.

Equation 4.22 can be written as

$$L_{\text{tot}} = L_{\text{res}} + \frac{L_{\text{g}}}{1+\beta_{\text{L}}^{(1)}\cos(\phi_{\text{int}}^{(1)}) - \alpha\frac{\partial\phi_{\text{int}}^{(2)}}{\partial\phi_{\text{int}}^{(1)}}} + \frac{L_{\text{g}}}{1+\beta_{\text{L}}^{(N)}\cos(\phi_{\text{int}}^{(N)}) - \alpha\frac{\partial\phi_{\text{int}}^{(N-1)}}{\partial\phi_{\text{int}}^{(N)}}} + \sum_{i=2}^{N-1}\frac{L_{\text{g}}}{1+\beta_{\text{L}}^{(i)}\cos(\phi_{\text{int}}^{(i)}) - \alpha\frac{\partial}{\partial\phi_{\text{int}}^{(i)}}(\phi_{\text{int}}^{(i-1)}+\phi_{\text{int}}^{(i+1)})}. \tag{4.24}$$

Using the expression $\partial^2 y/\partial x^2 = -\left[\partial x/\partial y\right]^{-3}\left[\partial^2 x/\partial y^2\right]$, which can be obtained using the chain and quotient rules, we find that the derivative of the inductance is given by

$$\frac{\partial L_{\text{tot}}}{\partial\phi_{\text{ext}}} = L_{\text{g}}\sum_{i=1}^{N}\frac{1}{(x_i)^3}\left(\beta_{\text{L}}^{(i)}\sin(\phi_{\text{int}}^{(i)}) + \alpha\frac{\partial^2}{\left(\partial\phi_{\text{int}}^{(i)}\right)^2}\left[(1-\delta_{i,N})\phi_{\text{int}}^{(i+1)} + (1-\delta_{i,1})\phi_{\text{int}}^{(i-1)}\right]\right), \tag{4.25}$$

where

$$x_i = 1+\beta_{\text{L}}^{(i)}\cos(\phi_{\text{int}}^{(i)}) - \alpha\frac{\partial}{\partial\phi_{\text{int}}^{(i)}}[(1-\delta_{i,N})\phi_{\text{int}}^{(i+1)} + (1-\delta_{i,1})\phi_{\text{int}}^{(i-1)}], \tag{4.26}$$

and $\delta_{i,j}$ is the Kronecker delta.

Equation 4.25 will be infinite if $x_i = 0$. We will examine equation 4.26 around integer flux, where jumps have been observed. Using the small angle approximation we obtain

$$\frac{\phi_{\text{int}}^{(i)}}{\phi_{\text{int}}^{(i\pm1)}} \approx \frac{2\alpha}{\left(1+\beta_{\text{L}}^{(i)}\right)} \approx 1, \tag{4.27}$$

for inner SQUIDs, and

$$\frac{\phi_{\text{int}}^{(1,N)}}{\phi_{\text{int}}^{(2,N-1)}} \approx \frac{\alpha}{\left(1+\beta_{\text{L}}^{(1,N)}\right)} \tag{4.28}$$

for the edge SQUIDs. This solution requires that $\alpha > 0.5$ which is unphysical since it requires that a rectangular SQUID has a side inductance greater than half of its total inductance.

The jumps must therefore arise from the term $\partial^2\phi_{\text{int}}^{(i\pm1)}/\partial{\phi_{\text{int}}^{(i)}}^2$. This term goes to infinity when the circulating current through a SQUID changes hysteretically, with a phase difference between neighbouring SQUIDs. The phase difference arises due to the edge effects in the array. This term can be thought of as a measure of the disorder of the flux configuration of the SQUIDs in the array. The system disorder is discussed further in chapter 5.

4.3 Numerical Modelling of the Coupled SQUID Array

It is possible to solve the equations 4.4 numerically in order to find the internal flux as a function of applied field. This then allows us to plot the modelled frequency modulation curve. In this section we present the results of numerical analysis of the model.

The equations 4.4 have been solved using python using combinations of secant-like and Newton-Raphson-like methods. Both of these methods suffer in the presence of high hysteresis, the secant method because the function now may have multiple roots in each window and Newton-Raphson because of the kinks in the gradient. Therefore once each solution is calculated it is passed back to the equations to check it is a valid root. If it does not fall within a defined window of error, both the x and y coordinates are removed from the solution and replaced with null placeholders. This leads to gaps in the curve if the system is highly hysteretic but ensures that all of the presented solutions are accurate.

The hysteresis is accounted for by iterating along the array first in terms of increasing ϕ_{ext} then decreasing, with the solution to the previous field used as the zeroth iteration for the subsequent solution. A flaw with this method is that it assumes that there are two solutions or less for each value of applied field. In most practical samples this should be the case. It is not however the case if, for example, $\beta_{\text{L}} > 2$, further complicating the modelling of highly hysteretic curves. It is important to account for the directionality in the up and down sweeps to show any kind of jump. Without accounting for the direction we produce two separate, smooth overlapping curves. The jumps appear as the system switches between those curves.

Figure 4.3 shows the calculated internal flux as a function of the external flux for a SQUID at the edge and for a SQUID in the middle of a 5 SQUID array. It is apparent that for an uncoupled array with $\beta_{\text{L}} < 1$ the function is smooth and continuous. The lines for each SQUID fall directly on top of each other. With non-zero α the curve becomes discontinuous and multivalued at some points in applied flux. It is of interest that these points have moved from the normal half flux point and that the periodicity of the curve is altered. The altered periodicity is due to the linear component of the coupling, $A^{(i)}$ (see section 4.2). Because the edge SQUIDs are only coupled to a single SQUID there is a phase difference between adjacent SQUIDs. This phase difference propagates some way into the array creating a spread of phases and leading to a complicated beating effect.

Figure 4.4 shows the modelled frequency modulation curves for 2 arrays of 32 SQUIDs for a range

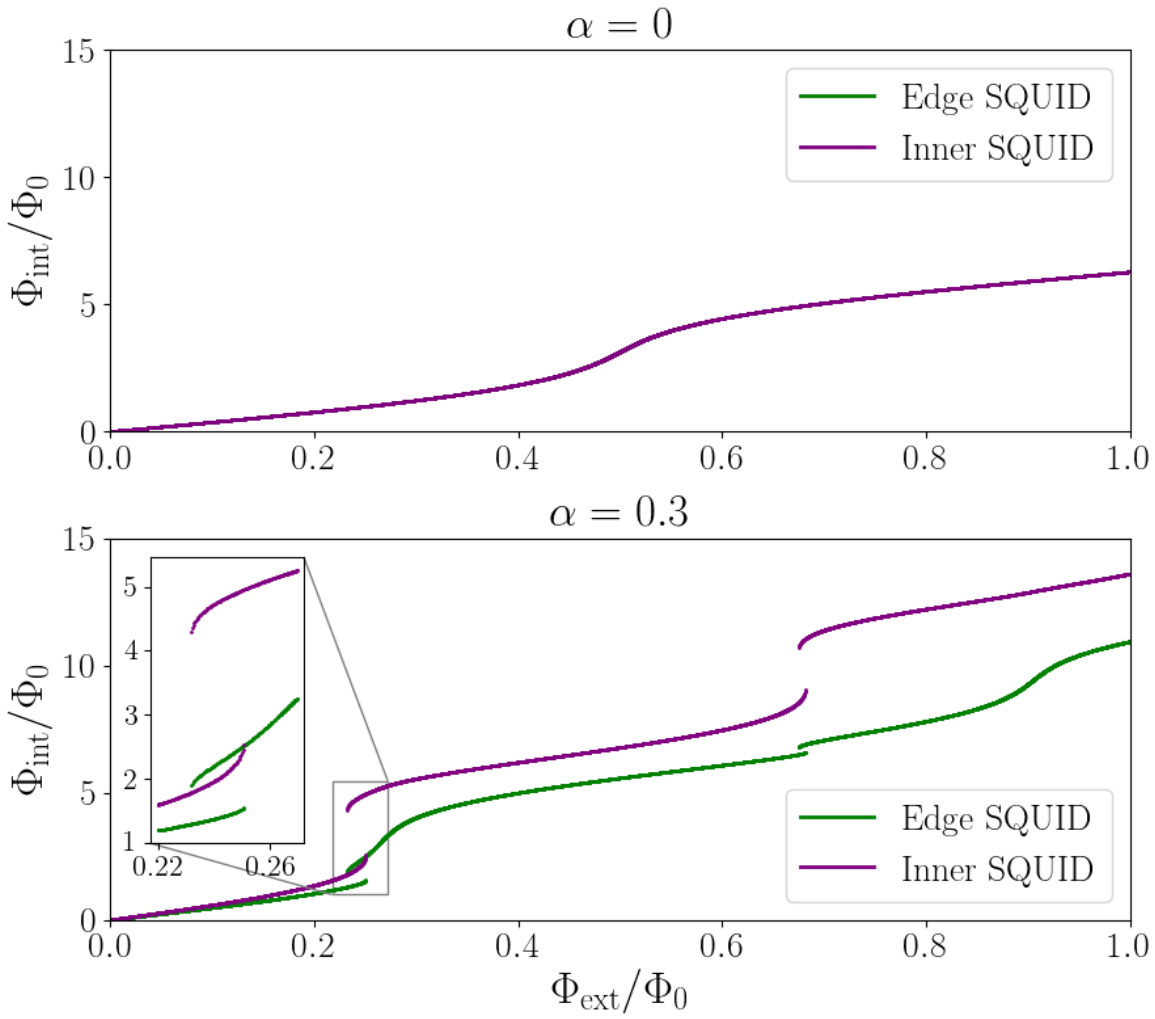

Figure 4.3: Introducing coupling between SQUIDs in an array can introduce hysteretic behaviour. The top plot shows the internal flux for an array of uncoupled SQUIDs against applied magnetic field. Both upper and lower panels are calculated for an array of 5 SQUIDs with $\beta_L = 0.7$. The curve remains single valued for all fields. The lower plot has a coupling factor of $\alpha = 0.3$ and may now occupy different states at certain fluxes.

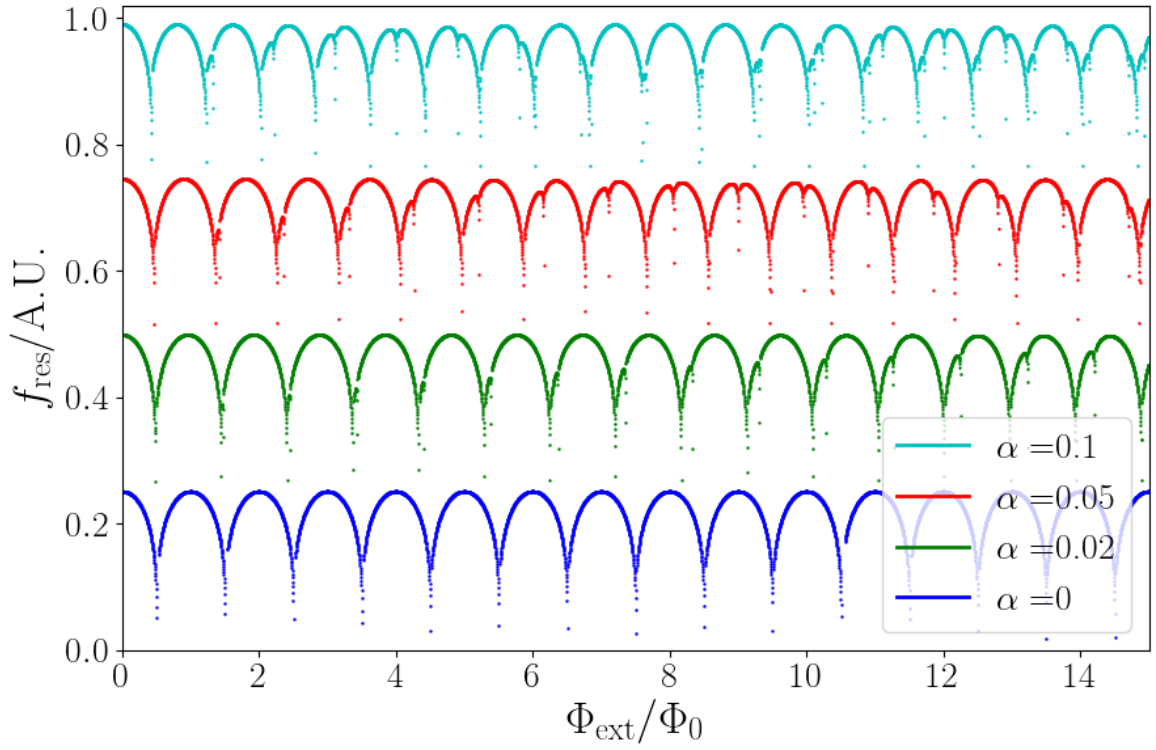

Figure 4.4: Frequency modulation curves for arrays with different coupling strengths α. Note that the coupling produces hysteretic jumps in the curve. The separation between curves is added artificially for clarity. These curves have been calculated for 2 arrays of 32 SQUIDs with $\beta_L = 1.15$. The parameters are chosen for illustrative reasons.

of coupling strengths. The curves are separated vertically for clarity. The array lengths have been chosen to correspond with the experiment described in section 2.7.2. The frequency modulation curve has been calculated with,

$$f_{res} = f_0 \sqrt{\frac{L_{res}}{L_{tot}}} \tag{4.29}$$

where $f_0 = 1/\sqrt{L_{res}C}$ has been set to 1 [$T^{-1}H^{0.5}$] and L_{tot} is the summation of the SQUID inductances and the resonator inductance.

It is apparent that the introduction of coupling into the array creates jumps. As the coupling is increased the jumps become more prevalent. This is because the jumps rely on the phase difference created by the edge SQUID coupling to only one neighbour. As the coupling is increased the effect of this phase difference penetrates further into the array. It should be noted that although the chosen value of $\beta_L = 1.15$ is greater than 1, without coupling we would only expect to see jumps at half flux. It is not necessary to have $\beta_L > 1$ to observe jumps, however in this case the coupling strength is small,

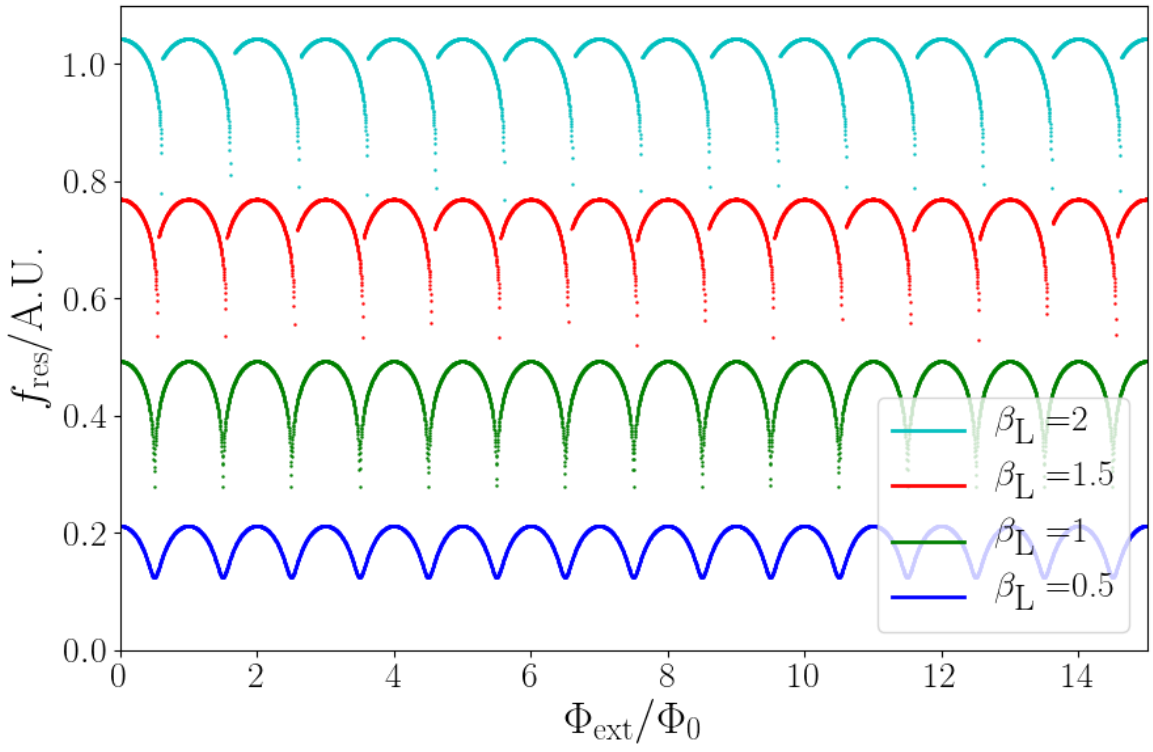

Figure 4.5: Frequency modulation curves for arrays with different dimensionless inductances β_{L}. Note that although there are jumps in the modulation curve for $\beta_{\mathrm{L}} > 1$, the jumps only occur at half-integer values of applied flux. These calculations have been performed for a resonator containing two arrays of 32 SQUIDs. The separation between curves is added for clarity.

resulting in a only small correction to the normal condition for hysteretic SQUID operation.

For contrast, figure 4.5 shows a series of frequency modulation curves for a sample containing 2 arrays of 32 SQUIDs. In this plot β_{L} has been varied. Note that although jumps are present in the curves for $\beta_{\mathrm{L}} > 1$, the jumps are only at half-integer values of applied flux and do not resemble those observed in the experiment described in section 2.7.2.

It is of interest to attempt to model the results of the experiment described in section 2.7.2. In the experiment measurements of the resonant frequency of a CPW resonator showed a beating effect as well as repeatable hysteretic jumps in the resonant frequency. Precise modelling is a difficult task because the total inductance of the array is reliant on the flux state of every SQUID in the array. This is strongly dependent on the value of α, which determines the spread of phases. There are also deviations in SQUID parameters to account for. Such deviations can create further regions of disorder in the array. For these reasons it is not possible to produce an accurate fit of the data. Figure 4.6 shows

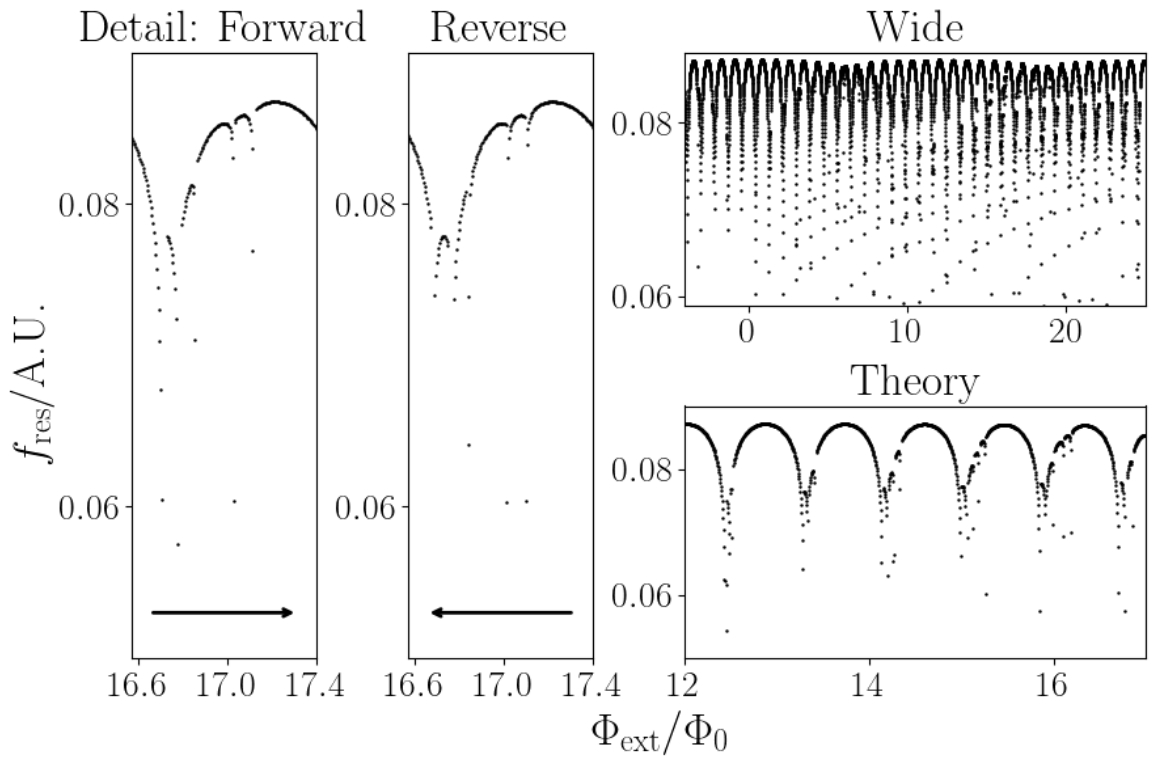

Figure 4.6: The modelled frequency modulation curve of a resonator containing 2 arrays of 32 SQUIDs, assuming a coupling of $\alpha = 0.07$ between adjacent SQUIDs, and a dimensionless inductance of $\beta_{\mathrm{L}} = 1.145$. The curve shows hysteretic jumps. Left: A detail of the jumps. Top: A wide view of the sweep shows that the curve also exhibits a beat like effect with a period of many flux quanta. Bottom: A shorter sweep. It is of note that the period of the curve is less than Φ_0.

the calculated frequency modulation curve with reasonable parameters input into the model. For this model, $\alpha = 0.07$ and $\beta_{\mathrm{L}} = 1.145$. Parameter deviation of the SQUIDs has been neglected. We are able to reproduce the jumps as well as the broad beating effect. The jumps in the model are softer than those in the experiment. There are several reasons for this. One is that in the model the frequency modulation curve is calculated by the differentiation of a discretely sampled array of fluxes. Secondly, and most significantly, in situations where the hysteresis is high the algorithms used to solve the simultaneous equation are less robust. This has limited the ranges of coupling strengths used. The tails in the jumps in the model are narrow. Experimentally this makes the system prone to thermal excitation into the higher hysteretic branch, resulting in a sharper jump.

The chosen value for α comes from a rough estimation of the ratio $L_{\mathrm{c}}/L_{\mathrm{g}}$ based on figure 2.10. Note that in both the model and the experiment a small sub-fringe appears between some fringes. This is the result of the flux dependent phase difference between neighbour SQUIDs. In this calculation β_{L}

has been treated as a fitting parameter.

By assuming a coupling between SQUIDs created by the shared side we are able to reproduce the main features of the experiment. These include the beating effect and the jumps, as well as subtler features such as the appearance of sub-fringes. The parameters input to the model are physically reasonable with respect to the experiment. The precise behaviour of the array depends on correctly accounting for the behaviour of each individual SQUID. In the disordered edge regions this is strongly dependent on the chosen parameters as well as any deviation in SQUID parameters.

Chapter 5

Modelling the Flux Configuration of the Array

A SQUID may be thought of as a circular current loop. This structure will have a magnetic moment, μ, proportional to the current circulating around the loop, $I_{\mathrm{s}} = I_{\mathrm{c}} \sin\left(\phi_{\mathrm{int}}^{(i)}\right)$. This is illustrated in figure 5.1. These magnetic elements have been shown to be coupled by a shared current along a shared side in chapter 4. The coupling will have an effect on how the magnetic moments of the SQUIDs behave as a function of applied field. We may expect, for instance, that in a strong coupling regime adjacent SQUIDs would favourably align in an an anti-parallel state. In contrast, in the case of zero coupling we would expect the SQUIDs to behave identically. Therefore the magnetic moments would be aligned in parallel.

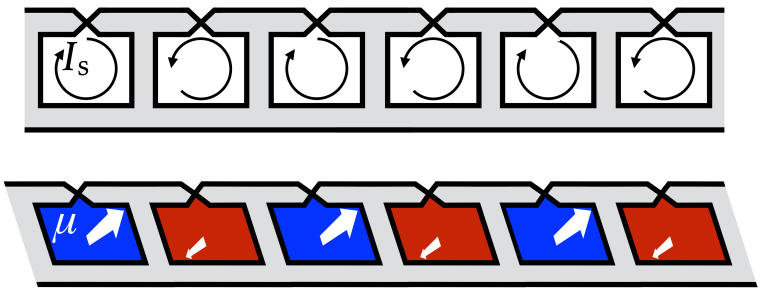

Figure 5.1: Top: A diagram showing an array of SQUIDs acting as current loops. The moments are shown in an antiparallel configuration. Lower: Diagram of the magnetic moments of the array.

This chapter will extend the modelling work described in chapter 4 to examine the expected

behaviour of the magnetic moments of the SQUIDs in different coupling regimes. We will look at how far into the array the edge effect propagates and explore how this affects the behaviour of the system in different length arrays.

5.1 Hysteretic Effects in the Flux Configuration of the Array

The SQUID array can be considered as a string of magnetic moments. Depending on the strength of the coupling we may expect the array to behave in qualitatively different manners. Figure 5.2 shows the magnetic moments of an array of 20 SQUIDs with a coupling of $\alpha = 0.1$ (top) and $\alpha = 0.4$ (bottom). In the weakly coupled array the SQUIDs in the centre of the array behave identically. Towards the edges of the array there are some SQUIDs which are out of phase with each other. This edge region extends around 3 SQUIDs into the array. We have chosen $\beta_{\mathrm{L}} = 0.3$ since this ensures that the system is non-hysteretic. When the coupling is increased the disordered edge region is much larger. This corresponds to the increased energy cost of the moments being aligned in parallel when they are strongly interacting. The period of the behaviour is significantly shorter in the strongly coupled plot due to the linear component of the coupling. This effect is discussed in detail in chapter 4.

In chapter 4 we found that the observed jumps in the frequency modulation curve were the result of disorder in the array; we required a SQUID to undergo a hysteretic alteration in its alignment with its neighbour. Figure 5.2 shows that the disordered region of the array is at the edge of the array. It is in these regions therefore that we expect to find the origin of the hysteretic resonant frequency jumps. The magnetic moments of the SQUIDs in the array are compared to the frequency modulation curve in figure 5.3. The frequency modulation curve is shown in the left hand panel. The centre and right panels show the magnetic moment configuration. We note that as expected the jumps occur at positions in applied flux at which there is a hysteretic change in alignment between the neighbour SQUIDs. In this case, due to the relatively low coupling coefficient of 0.2, the jumps are due to the flip of only the edge-most SQUID. The disordered edge region penetrates 3 SQUIDs into the array, with the third SQUID only negligibly different from the inner SQUIDs. The right hand panel shows a zoom of the edge few SQUIDs, where the hysteretic anti-alignment occurs. In this case the array is symmetric. In real systems the symmetry may be broken by either inhomogeneous fields or deviations in the loop area. In the simplest case of asymmetry in the array, either where the magnetic field inhomogeneity

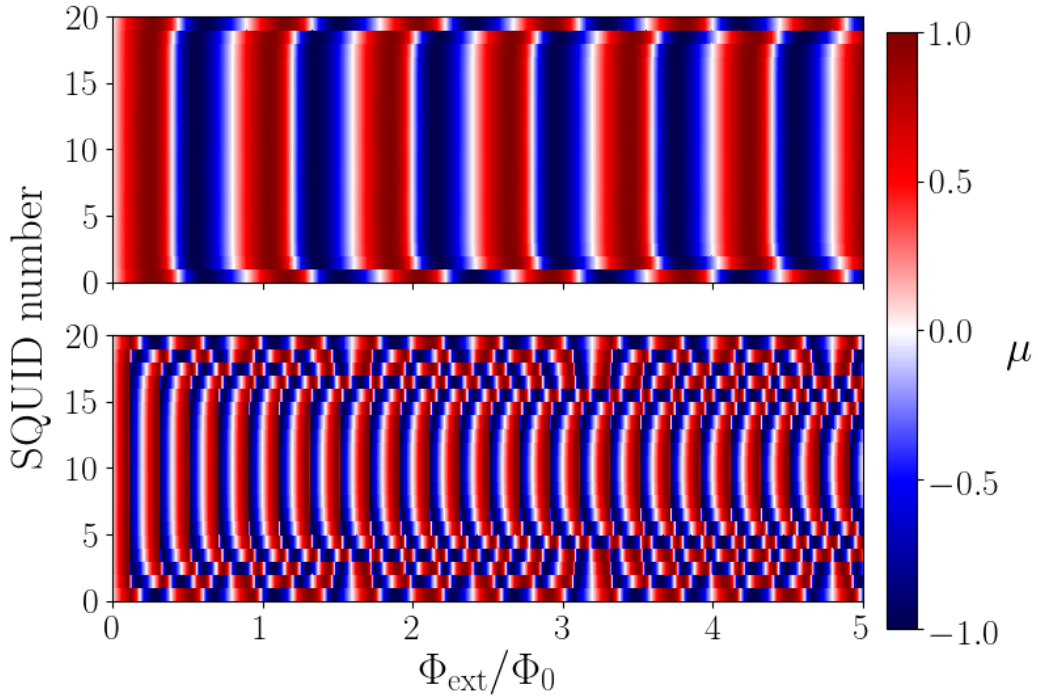

Figure 5.2: The flux configuration of an array of 20 SQUIDs. This has been calculated for an array with $\beta_{\text{L}} = 0.3$. In this regime the system is non-hysteretic. The colour represents the magnetic moment of the SQUID as a function of position in the array and applied field. The top panel is calculated for a coupling of $\alpha = 0.1$. We can see that the SQUIDs at the edges of the array have a different periodicity to those in the middle. In this weak coupling regime the edge region extends around 3 SQUIDs into the array. The lower panel is calculated for a coupling of $\alpha = 0.4$. In this regime the system is much more disordered.

produces a constant offset between each SQUID or where the field is uniform and only the edge most SQUID has a loop area deviation, we would expect the jumps arising from each edge to be offset from each other. This would cause the number of apparent jumps to double. In general these clean deviations causing constant offset are unlikely. The more general case of random deviation would result in the edge behaviour being functionally different at each end of the array. The underlying frequency modulation similar to that of an uncoupled system is the result of the coherent behaviour of the inner SQUIDs.

Because the edge region results in disorder and the inner region results in coherent behaviour we may expect to observe different behaviours depending on the inductively dominant region. In short arrays we would expect disorder to dominate whereas longer arrays will be dominated by the ordered region. This means that there is a finite window of array lengths in which we would expect to

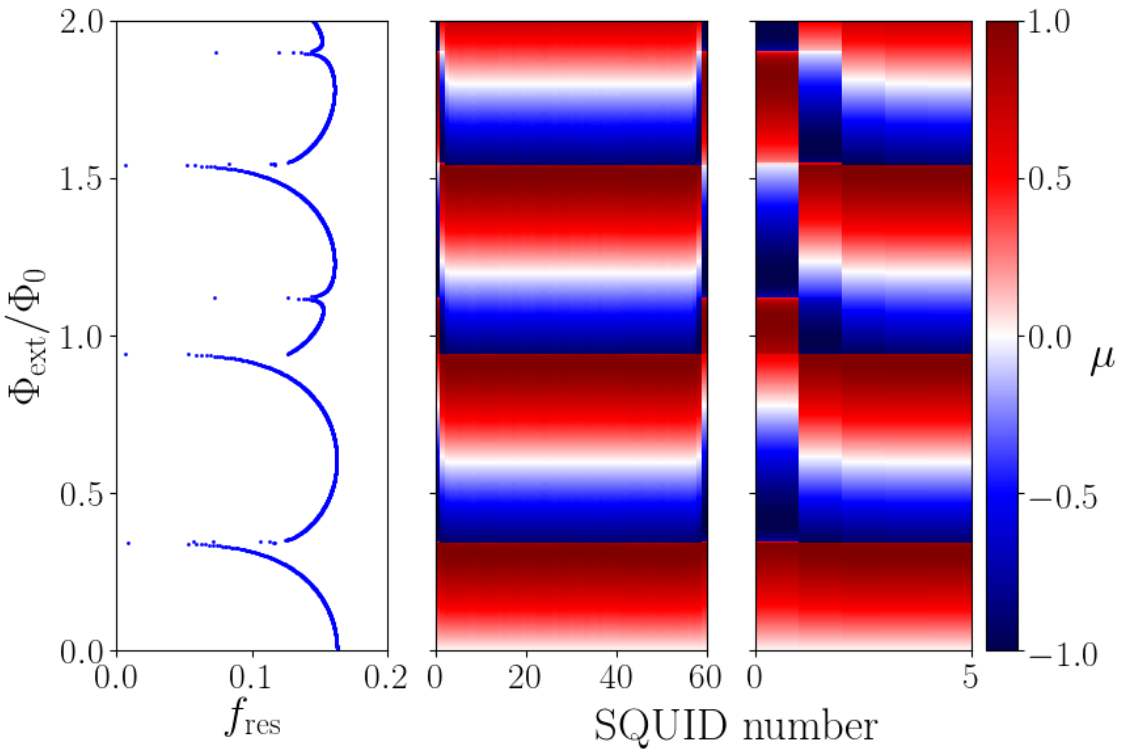

Figure 5.3: Left: Modelled resonant frequency as a function of applied flux of an array of 60 RF SQUIDs with $\alpha = 0.2$ and $\beta_{\mathrm{L}} = 1.01$. The resonator is described by $C_{\mathrm{res}} = 1\,\mathrm{F}$ and $L_{\mathrm{res}} = 1\,\mathrm{H}$. Note that the hysteretic jumps in the frequency occur at applied fluxes at which the magnetic moments of edge SQUIDs flip. Centre panel: The magnetic moment configuration of the array. The moments at the edge of the array are out of phase, whereas inner SQUIDs are in phase. Right: A zoom on the disordered edge region of the array.

observe jumps; the array needs to be long enough that the disorder acts merely as a perturbation to the ordered region, but short enough that the inductance jump is still significant compared to the total array inductance. The latter of these conditions is dependent on the resolution with which it is possible to measure the SQUID inductance. High resolution can be achieved by measuring the resonant frequency of a high Q resonator.

The flux configuration and frequency modulation curve for a range of different array lengths is plotted in figure 5.4. In the case of an array of 2 SQUIDs, the SQUIDs are identical and the coupling therefore does not impact the functional form of the modulation. Because the SQUIDs are in phase at all positions of flux this is the case with the greatest modulation depth. With 4 SQUIDs there are 2 edge SQUIDs and 2 inner SQUIDs. Assuming symmetry this results in a beating effect composed of only 2 frequencies with equal amplitudes. These correspond to the inner and the edge SQUID. As the

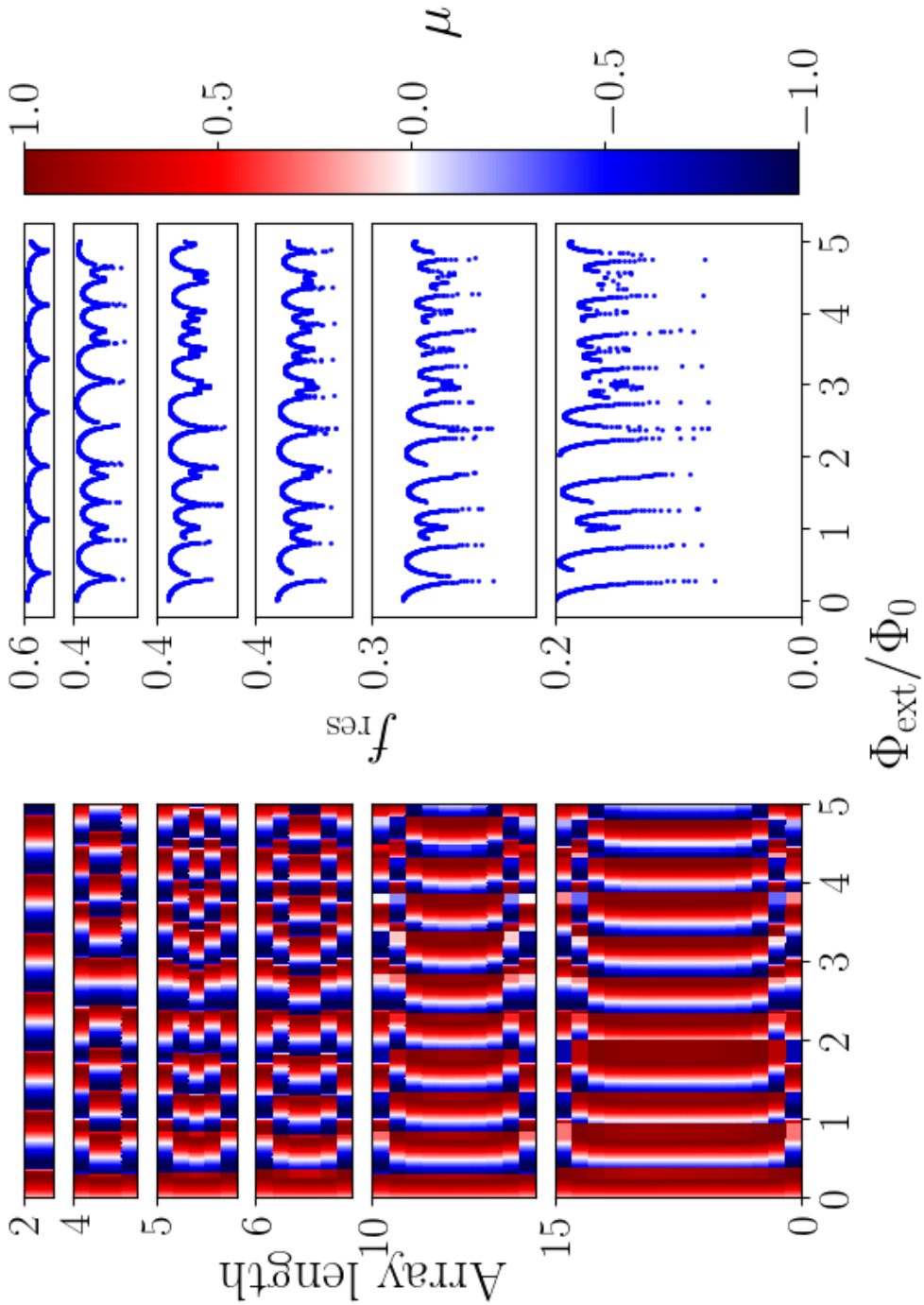

Figure 5.4: Left: Modelling of flux configuration for different length arrays. Right: The modelled flux modulation curve for the array. The observed behaviour is dependent on the length of the array. In short arrays disordered behaviour dominates and the normal frequency modulation curve becomes obscured resulting in a beating effect. In an array of 2 SQUIDs the SQUIDs behave identically, this means there is no beating effect. This has been calculated for $\alpha = 0.25$ and $\beta_{\mathrm{L}} = 0.7$.

array length is increased the number of possible flux configurations increases resulting in increasingly complicated beating effects. At a length of 15 SQUIDs the array is sufficiently long for the formation of an ordered inner region isolated from the penetration of the edge effect. The length array needed to form this region is dependent on the coupling strength. In this case the coupling has been chosen to be 0.25.

In order to determine whether the system's behaviour is dominated by the ordered region or the disordered region we investigate the length of the propagation of the edge region of the array as a function of coupling strength. Whether the system is predominantly ordered or disordered will dictate whether the system will behave in a normal manner, with perturbation to a smooth frequency modulation or in an irregular fashion, where the jumps obscure any regular frequency modulation.

The disorder is caused by the different effective fields felt by the inner and edge SQUIDs. This means that the level of disorder depends only on the linear part of the coupling, $A^{(i)}$. This is explained more fully in chapter 4. To determine the dominance of the edge effect we need only investigate the variation of $A^{(i)}$ through the array at different coupling strengths. This functionality can be found using equation 4.18. The solution to this for a 100 SQUID array is plotted in figure 5.5. The effective fields felt by each SQUID are modified by the term $A^{(i)}$ which arises from the coupling. The modification is dependent on the position of the SQUID within the array. The variation of $A^{(i)}$ is shown in the top panel of figure 5.5. We see that the modification is largest in the centre of the array, however, this is where it is also most uniform. The difference in the field modification through the array is the origin of the phase difference. This is maximal at the edges and non-zero for all but the centre 2 SQUIDs if N is even. The penetration of the disordered edge region into the array is a function of the applied field. As the field is increased the phase difference between neighbouring SQUIDs will increase. This means that at sufficiently low fields the edge region will always be negligible. At high fields the disordered region will always dominate. This is demonstrated in the lower panel of figure 5.2. In order to determine how far the edge region will penetrate into the array it is therefore necessary to define the applied fields over which the array will be measured. The lower panel of figure 5.5 shows the penetration of the edge region into the array as a function of flux for an array having a maximum difference of half a percent at 50 flux quanta. At coupling strengths of $\alpha = 0.5$ the edge region saturates to 50 SQUIDs. This is because the array consists of only 100 SQUIDs. This means that the inner, ordered region has been entirely removed. For all geometrically achievable coupling strengths α is less than 0.5.

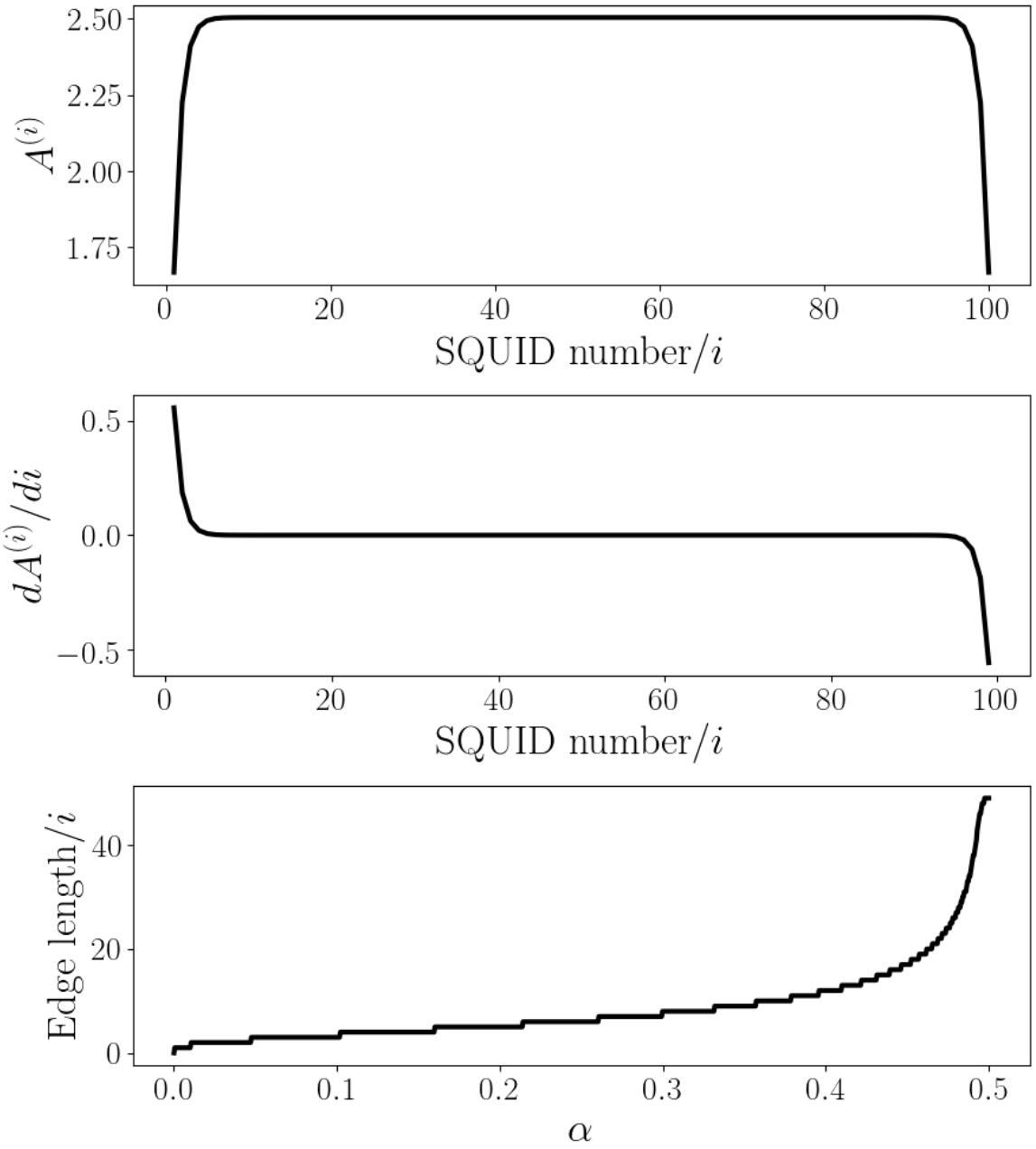

Figure 5.5: The penetration of the edge effect into the array. Top: The modification to the field caused by the coupling against the position of the SQUID in the array. There is a significant difference in the modification for the SQUIDs in the edge and the inner regions. This has been calculated for a coupling strength of $\alpha = 0.3$. At higher coupling strengths the edge region is larger. Middle: The derivative of the effective field of the SQUIDs with respect to their array position. The gradient is maximum at the edges but is non-zero throughout the array. This has also been calculated for $\alpha = 0.3$. Lower: The distance into the array that the edge effect penetrates before the SQUIDs effective field are approximately equal as a function of coupling strength. Since there is a finite effective field difference throughout the array at sufficiently high fields the edge region will always dominate the behaviour. In this case we have defined equality as having a phase difference of less than half a percent over 50 flux quanta.

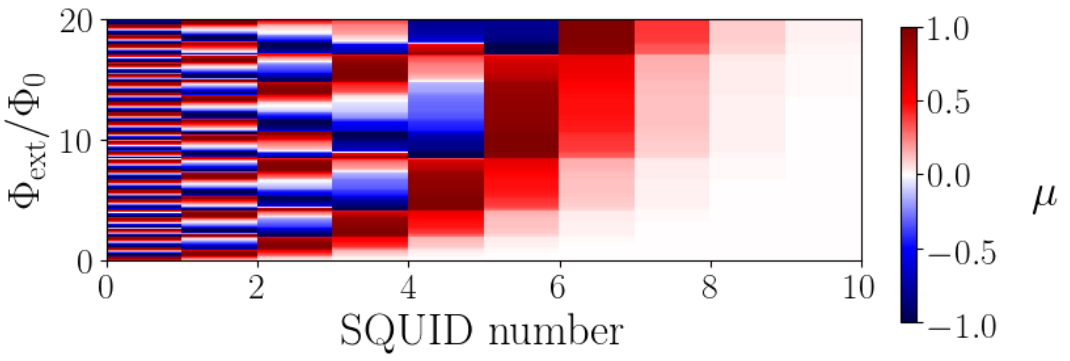

Figure 5.6: The coupling means that flux is able to be shared between SQUIDs. This results in an effective field different from the applied field. In this plot flux enters only the edge SQUID. The coupling then allows flux to spread along the array. The coupling in this plot is $\alpha = 0.4$.

In order to understand the modification to the applied field caused by the coupling, figure 5.6 shows the effect of applying a magnetic field only to the edge SQUID of a strongly coupled array. This is intended only as an illustration, although it may be possible to achieve a similar effect using on chip flux bias lines. We can see that the flux vortices are able to travel some distance along the array. This is the origin of the modification to the applied field.

There are 2 sources of hysteresis in the frequency modulation curve. The first is the conventional hysteresis associated with $\beta_{\mathrm{L}} > 1$. In this case the condition for hysteretic behaviour is modified by the coupling so that hysteresis may manifest itself in the case of $\beta_{\mathrm{L}} < 1$ providing the coupling is sufficiently strong. The second source of hysteresis is the result of the hysteresis in the flux configuration. This is reliant on the condition $\beta_{\mathrm{L}} \gtrsim 1 - \alpha$. The hysteresis in the flux configuration is the result of disorder in the edge region of the array. The jump occurs when the magnetic moment of a SQUID changes between parallel alignment and anti-parallel alignment or vice versa with its neighbour SQUID. The realignment results in a change of the total inductance of the system. Unlike the jumps occurring from the conventional hysteresis associated with order and a large β_{L}, due to disorder, the moment flip may occur at any position of phase.

5.2 The Effect of Dispersion of SQUID Parameters

In a coupled array the state of each SQUID is dependent on the state of those around it. We may, therefore, expect the system to be significantly disrupted by any kind of parameter dispersion. For

example, if a SQUID with a loop area differing slightly from that of the other SQUIDs is inserted into an array it will couple to the applied field differently. This will result in a phase difference between it and the other SQUIDs in the array. The inductance of the SQUID is dependent on the applied field. In the uncoupled case the total inductance of the array will therefore deviate from the expected inductance by the difference in the inductance of the deviating SQUID. In the coupled case the phase difference will impact the neighbouring SQUIDs, creating a disordered region centred on the differing SQUID. The total inductance will then differ from the expected total inductance by the summation of several disordered SQUIDs. The coupling has therefore acted to magnify the effect of the parameter deviation on the system.

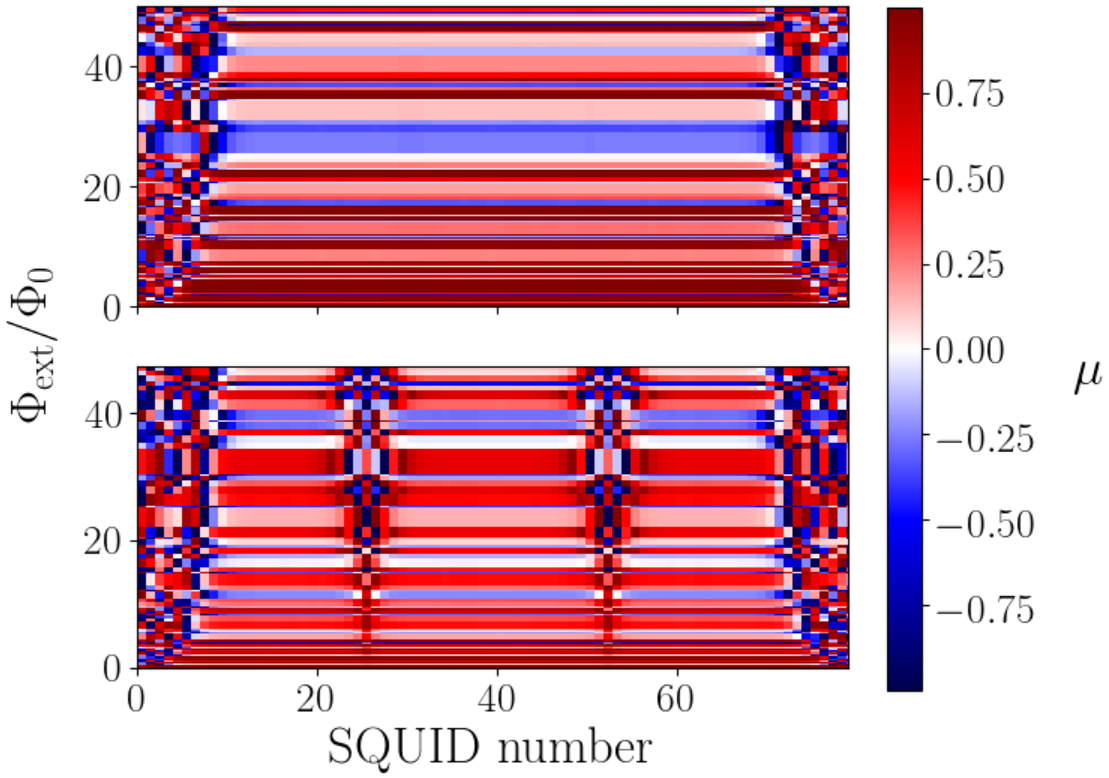

Figure 5.7: Top: The configuration of the magnetic moments in an array of 80 SQUIDs as a function of applied field for an array with strong coupling. This is calculated for $\alpha = 0.4$ and $\beta_L = 0.7$. There is a distinct region at the edge of the array where the magnetic moments are disordered. Bottom: The loop area of the SQUIDs at positions 26 and 52 have been enlarged by 2%. This shows that a small deviation in SQUID area may result in a large region with poorly controlled phases. The choice of a deviation of 2% is physically reasonable for SQUIDs of a loop area of a few tens of micrometers.

This principle has been explored in figure 5.7. The top panel shows the flux configuration of an array with identical SQUIDs. In the lower panel the loop area of the SQUIDs at positions 26 and 52 have been enlarged by 2%. The enlargement has resulted in the formation of a disordered region surrounding each deviation. In this case the coupling is strong, with a coefficient of $\alpha = 0.4$. This accentuates the effect, as can be verified by a comparison of the disordered edge widths of the strongly and weakly coupled arrays shown in figure 5.2. The array length of 80 SQUIDs is chosen to ensure that there is sufficient room for the development of the ordered state either side each disordered region. The chosen deviation of 2% is physically reasonable for SQUIDs with a loop area of around $50\,\mu\mathrm{m}^2$. In real arrays the deviation would result from uncertainty in the fabrication process. This means that we would expect the loop areas to differ in an uncontrolled manner throughout the array. In this situation the coherence of a strongly coupled array would be entirely lost. Clearly this is a significant issue in the development of devices containing an array of SQUIDs fabricated with a common current branch.

To some extent this problem may be alleviated by fabricating arrays in which the shared inductance is low. This would result in a weak coupling meaning that the disordered region would not propagate as far into the array. The problem may also be reduced by utilising a larger geometry, where the percentage uncertainty in the fabrication of the loop is somewhat lower.

The next parameter which may have some deviation through the length of the array is the critical current of the junctions. We would expect this to impact less significantly on the behaviour of the total SQUID array since the coupling is between the adjacent phases and there is no direct junction-junction coupling. However, it may result in altered hysteresis of the SQUID, causing the magnetic moment to flip to a state that would not otherwise have been accessible.

The question of how robust the behaviour of an array of SQUIDs is to some dispersion of junction parameters through the array may be explored by modelling how the inclusion of a single SQUID in the array that has differing critical current from its neighbour affects the observable behaviour of the array. We might expect the coupling to affect the number of SQUIDs affected by the impurity. The dependence of the behaviour on the position of the parameter deviation will also be of interest, since the edge regions behave differently to the inner SQUIDs. We therefore systematically vary the position of the deviating SQUID in the array.

Figure 5.8 shows how the position of a SQUID with I_c different from the rest of the array affects the total inductance of the array in the strong coupling ($\alpha = 0.4$) regime. The distribution of the different

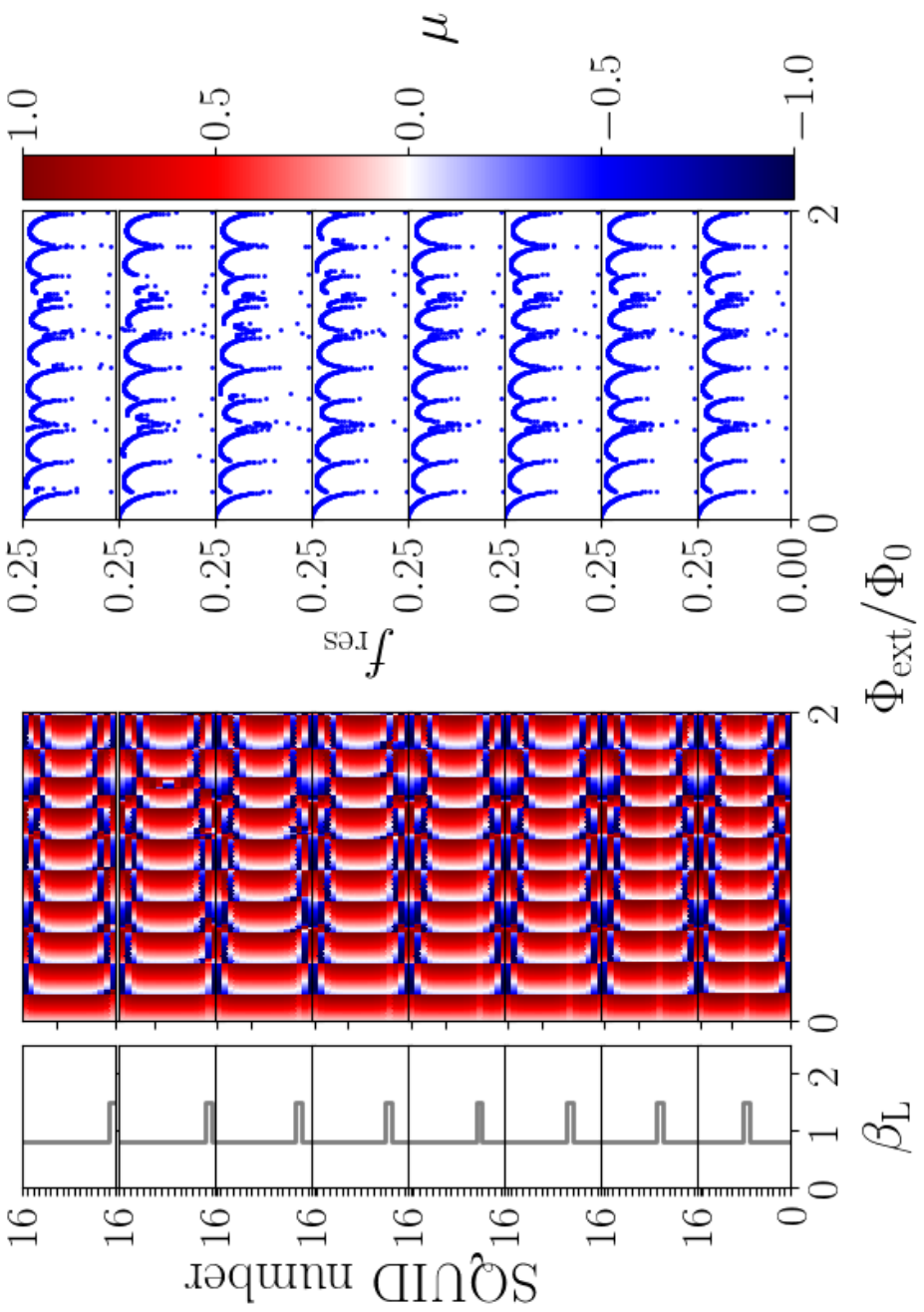

Figure 5.8: This shows the effect of dispersion in the critical current of a strongly coupled array. The coupling coefficient is $\alpha = 0.4$. The SQUIDs have a β_L of 0.8. There is a SQUID inserted into the array with a β_L of 1.5. The position of the SQUID with the higher critical current has been moved to different positions in the array. The β_L of the SQUIDs through the array is shown in the left hand panel. The middle panel shows the distribution of the magnetic moments. The right hand panel shows the resultant frequency modulation curve. The position of the differing junction makes little difference to the total inductance of the system.

critical currents is shown in the left most plots. The position of the differing junction is incremented between the vertically separated plots. The centre plots show the flux configuration. The right most plots show the resonant frequency of a resonator containing the array of SQUIDs with $C_{\text{res}} = 1\,\text{F}$ and $L_{\text{res}} = 1\,\text{H}$. There is little difference between the plots. This means that even in this strong coupling regime where we would expect to be most sensitive the system is robust with respect to deviations in the critical current of the individual junctions in the array.

We may expect the deviation of critical currents to have a more significant impact where the total array length is shorter. In shorter arrays the contribution from each SQUID is proportionally more significant. Figure 5.9 shows the frequency modulation curve and flux configuration of an array of 3 SQUIDs. There is some small change in the frequency modulation curve, but the system is still reasonably robust to the change in the configuration of critical currents. This means that although having a finite dispersion of junction characteristics will affect the behaviour of the system, the behaviour is not greatly modified by the introduction of nearest neighbour coupling between the SQUIDs.

5.3 Removing the Edge Effects

In order to improve the control experimental control of the system it is favourable to remove the disordered regions from the array. It may be possible to achieve this by reducing the geometric inductance of the edge SQUIDs, or equivalently, by increasing the geometric inductance of the inner SQUIDs. Since the coupling coefficient is $\alpha = L_{\text{c}}/L_{\text{g}}$, setting $L_{\text{g}}^{(\text{edge})} = \frac{1}{2}L_{\text{g}}^{(\text{inner})}$ creates an asymmetric coupling such that $\alpha_{01} = 2\alpha_{10}$ and the edge SQUID is effectively coupled to 2 SQUIDs. A diagram showing the layout of such a system is shown in figure 5.10. It should be noted that in order to ensure that β_{L} is uniform throughout the array, the critical current of the junctions in the edge SQUIDs will need to be double that of the inner SQUIDs.

The asymmetric coupling will cause a reflection of the flux transferred from the inner to the outer SQUID.

In real systems the added inductor, L, will not always be perfectly matched to the loop inductance L_{g}. It is of interest therefore to examine how the accurate the inductance matching needs to be in order to remove the edge effect.

Figure 5.11 shows the difference in phase between the edge SQUID and its neighbour as a function

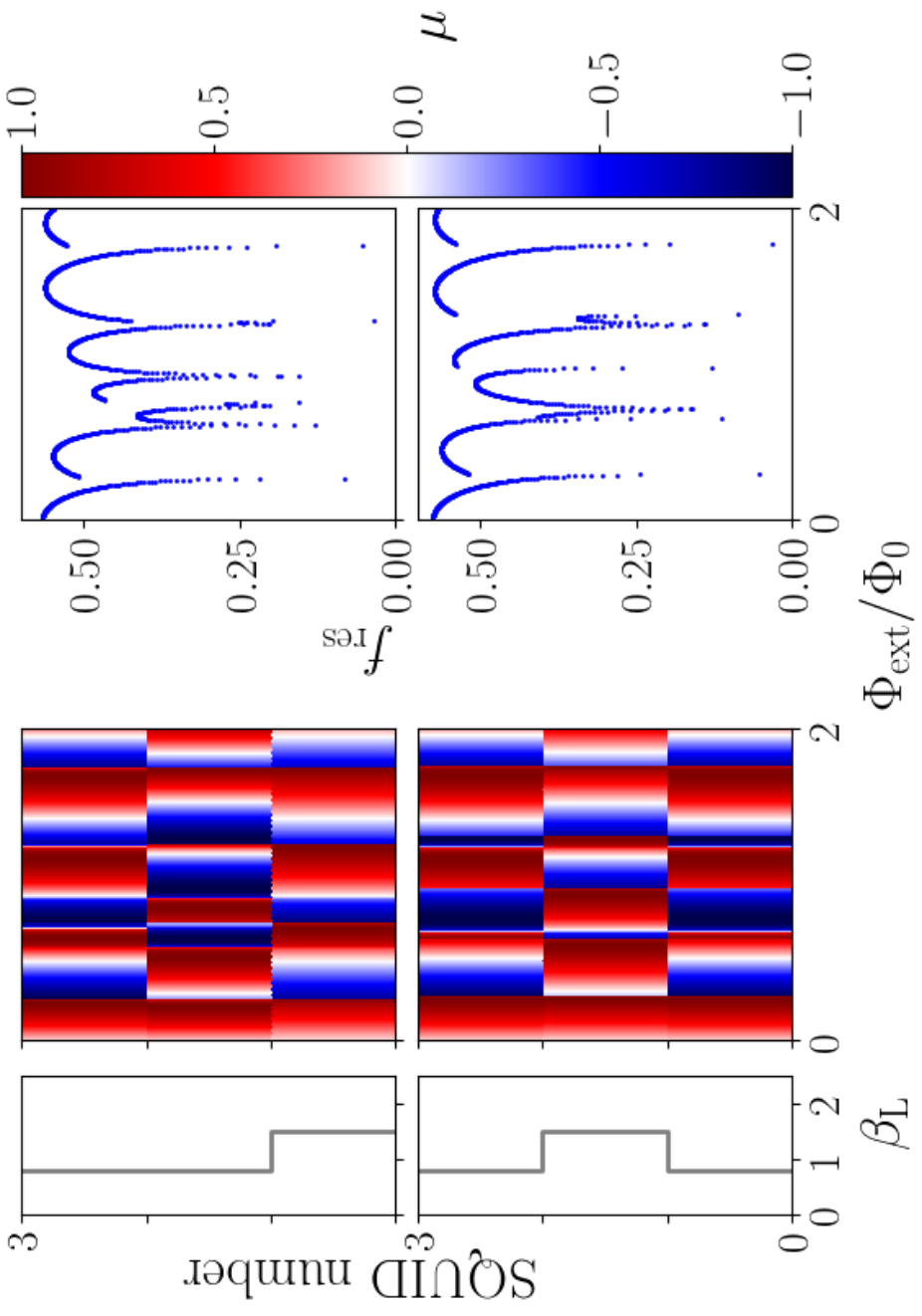

Figure 5.9: This shows the effect of dispersion in the critical current of a strongly coupled short array. The coupling coefficient is $\alpha = 0.4$. The SQUIDs have a β_L of 0.8. There is a SQUID inserted into the array with a β_L of 1.5, the position of the which has been varied. The β_L of the SQUIDs is shown in the left hand panel. The middle panel shows the distribution of the magnetic moments. The right hand panel shows the resultant frequency modulation curve. There is some variation in the frequency modulation curve depending on the position of the SQUID with poorly controlled junction characteristics, however the effect is not significant.

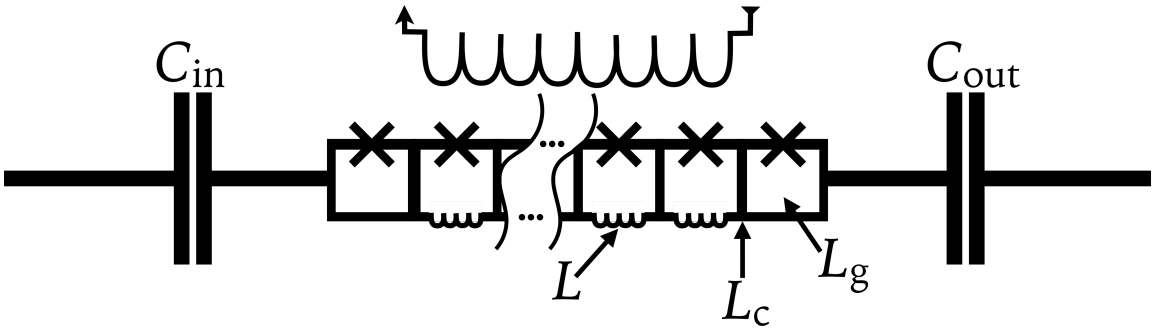

Figure 5.10: It may be possible to create asymmetric coupling and hence remove the edge effects by adding an inductor to the loop of the inner SQUIDs in the array. This creates an asymmetric coupling between the edge and the inner SQUIDs, removing the cause of the edge effect.

of applied field and the ratio of the geometric inductance of the edge and inner SQUIDs. If the difference in phase is zero then the edge effect has been removed. We can see that this is the case providing $1.95 \lesssim L_{\text{edge}}/L_{\text{inner}} \lesssim 2.05$ over the range of applied fields shown. For operation at high field it is expected that this condition will become more stringent.

Figure 5.12 shows the frequency modulation curves for different $L_{\text{edge}}/L_{\text{inner}}$. When $L_{\text{edge}}/L_{\text{inner}} \approx 2$ the behaviour is indistinguishable from the an uncoupled array. This means that the edge effect has been removed.

5.4 Summary

Over the last two chapters we have shown that it is possible to explain the beating pattern and hysteretic jumps discussed in section 2.7.2 by assuming a coupling between nearest neighbours. The coupling has a linear and an oscillatory part. The linear part leads to a difference in coupling to the external field, whilst the oscillatory part leads to a rescaling of the SQUID parameters.

The SQUID at the edge of the array is coupled to only one other SQUID. This introduces disorder into the array. The distance that the disorder propagates into the array is dependent on the coupling strength. The ratio of disorder to order dictates the collective behaviour of the array. Greater disorder leads to jumps in the frequency modulation curve. If the disorder significantly dominates the ordered region then the frequency modulation curve becomes washed out through destructive interference of the contributions of the inductance of the individual SQUIDs.

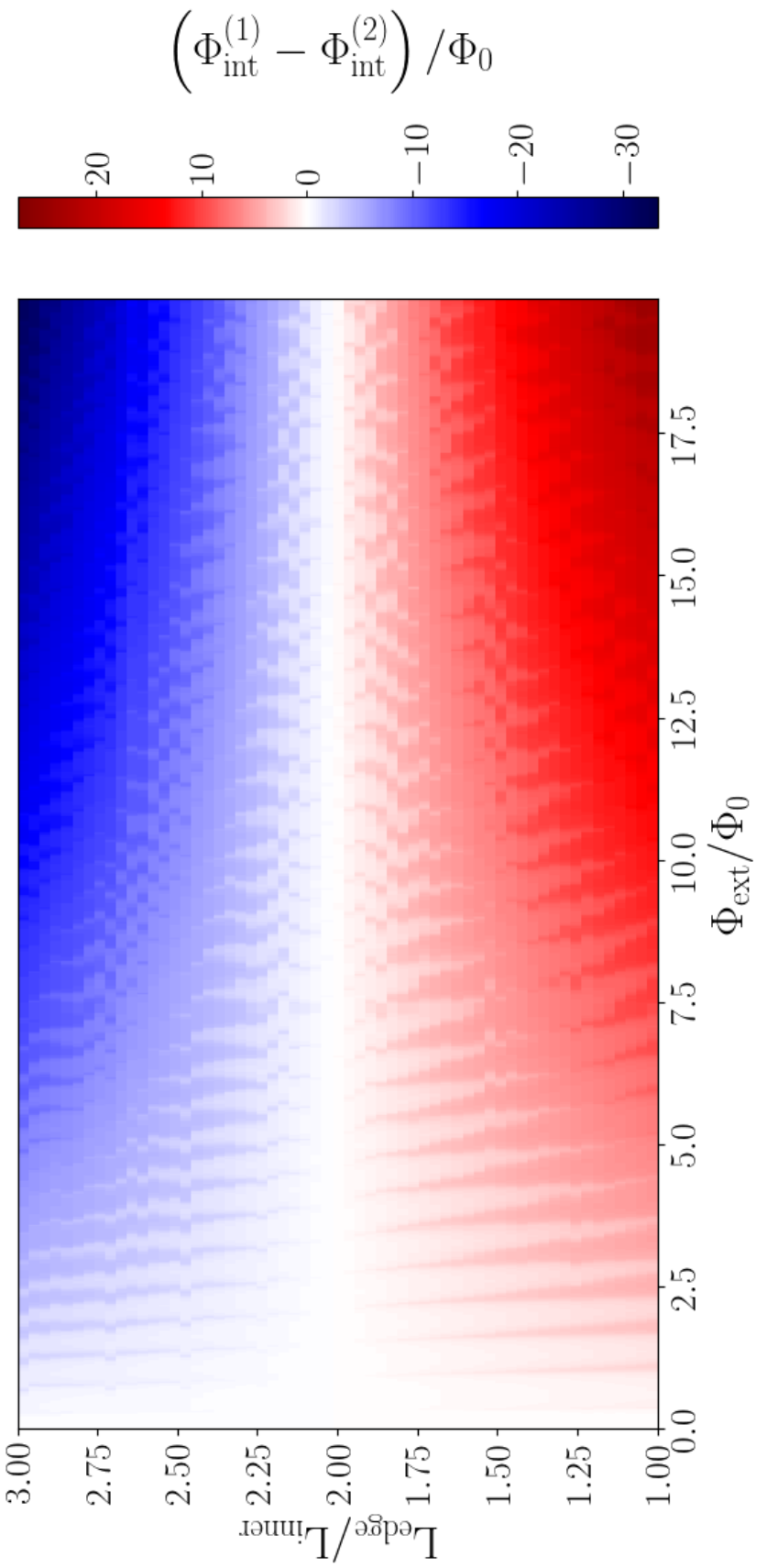

Figure 5.11: The edge effects for an array of 3 SQUIDs with $\beta_{\text{L}} = 0.6$, and $\alpha = 0.2$. The colour represents the difference between the edge and the neighbour SQUID. The applied field is increased along the x axis. The deviation in inductance matching is shown on the y axis. The case of perfect inductance matching is $L_{\text{edge}}/L_{\text{inner}} = 2$. When the inductances are well matched there is no difference between the edge and the inner SQUIDs. This means that the flux configuration of the array will be ordered throughout. This is true for inductances matched to within 5%. This is dependent the maximum applied field over which the system is required to remain ordered.

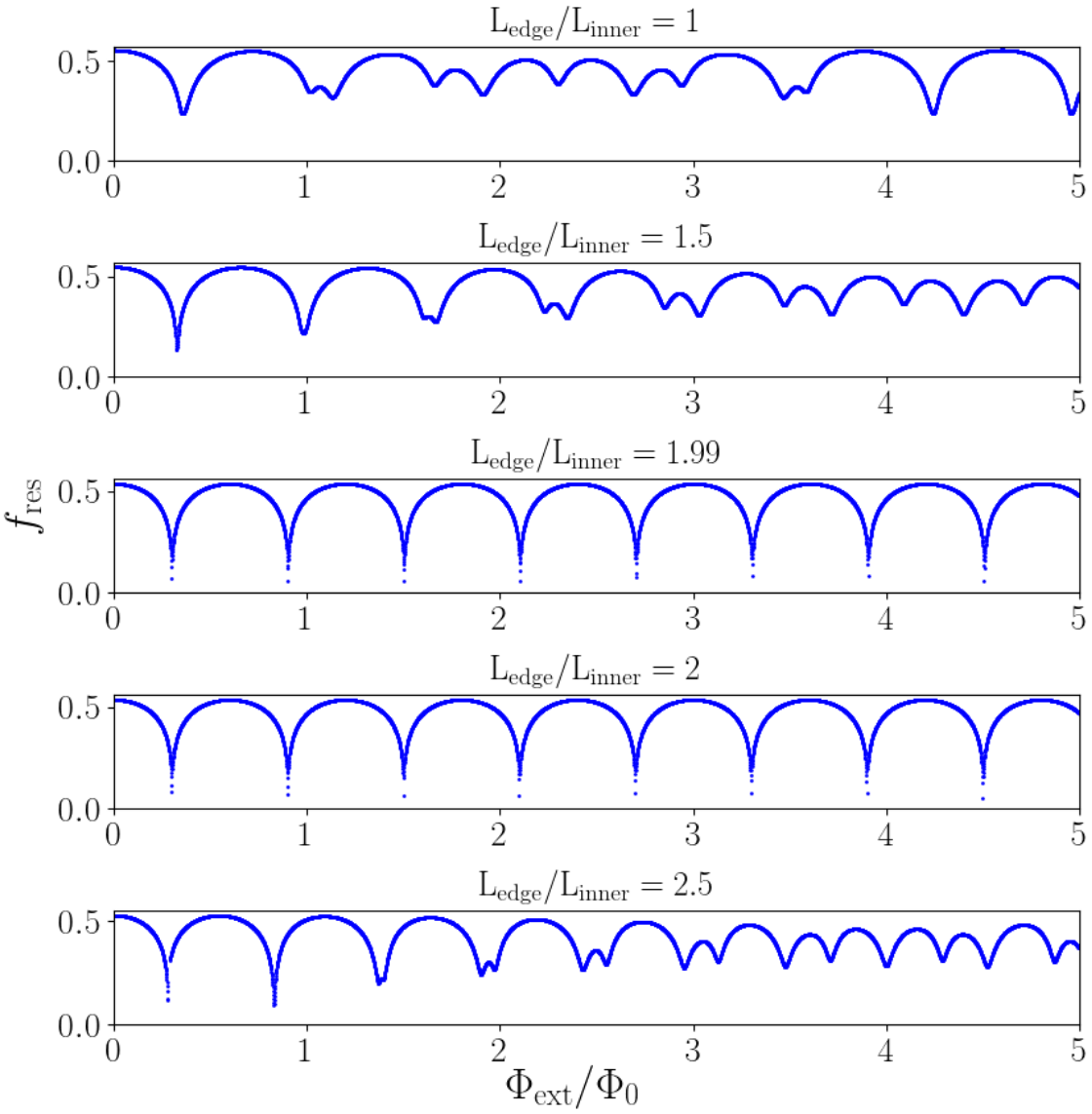

Figure 5.12: Modelled frequency modulation curves of arrays with different L_{edge}/L_{inner}. This is calculated for $\alpha = 0.2$ and $\beta_L = 0.6$ for a 3 SQUID array. The ratio L_{edge}/L_{inner} determines how completely the edge effect will be removed. When $L_{edge}/L_{inner} \approx 2$ the flux configuration is ordered and a normal frequency modulation curve is observed.

If the edge SQUID has a loop area equal to the inner SQUIDs, but with an additional inductance added through, for example, meandering of the superconducting wire, it is possible to introduce an asymmetric coupling. It is possible to design this so that the edge effect is removed. This means that although the SQUID parameters are still altered by the coupling, the SQUIDs would remain in phase at all fields, thus removing both the beating effect and the jumps.

Although the model reproduces both the observed jumps and the observed beating effect (discussed in section 2.7.2), the complexity of the sample meant it did not prove possible to fit the model to the data. The remainder of this thesis describes measurements performed on a shorter array of SQUIDs in order to reduce the parameter space.

Chapter 6

Experimental Setup

This chapter will give an overview of the experimental setup used to perform the measurements outlined in chapter 7.

6.1 Dilution Refrigerator

The experiment was performed in a Cryoconcept dilution refrigerator. After installation of experimental wiring the base temperature is approximately $20\,\mathrm{mK}$. The refrigerator is wet and requires a transfer of liquid helium on a 5 day cycle. During the transfer there is some temperature instability.

6.2 Thermometry

The temperature is monitored by 4 point measurements of 4 resistive thermometers at various temperature stages. The resistances of the thermometers are measured by two Stanford Research Systems AC resistance bridges. The thermometer best describing experimental conditions is a RuO_2 thermometer on the mixing chamber (MC). This will be called the MC thermometer. By comparison to SQUID noise thermometry it has been found that the MC thermometer is unreliable below a temperature of $50\,\mathrm{mK}$. This is attributed to the thermometer becoming thermally decoupled from the mixing chamber at low temperature.

At low temperature it is preferable to use noise thermometry, where a DC SQUID is used to measure the Johnson-Nyquist of a resistor. The noise thermometer was mounted on the mixing

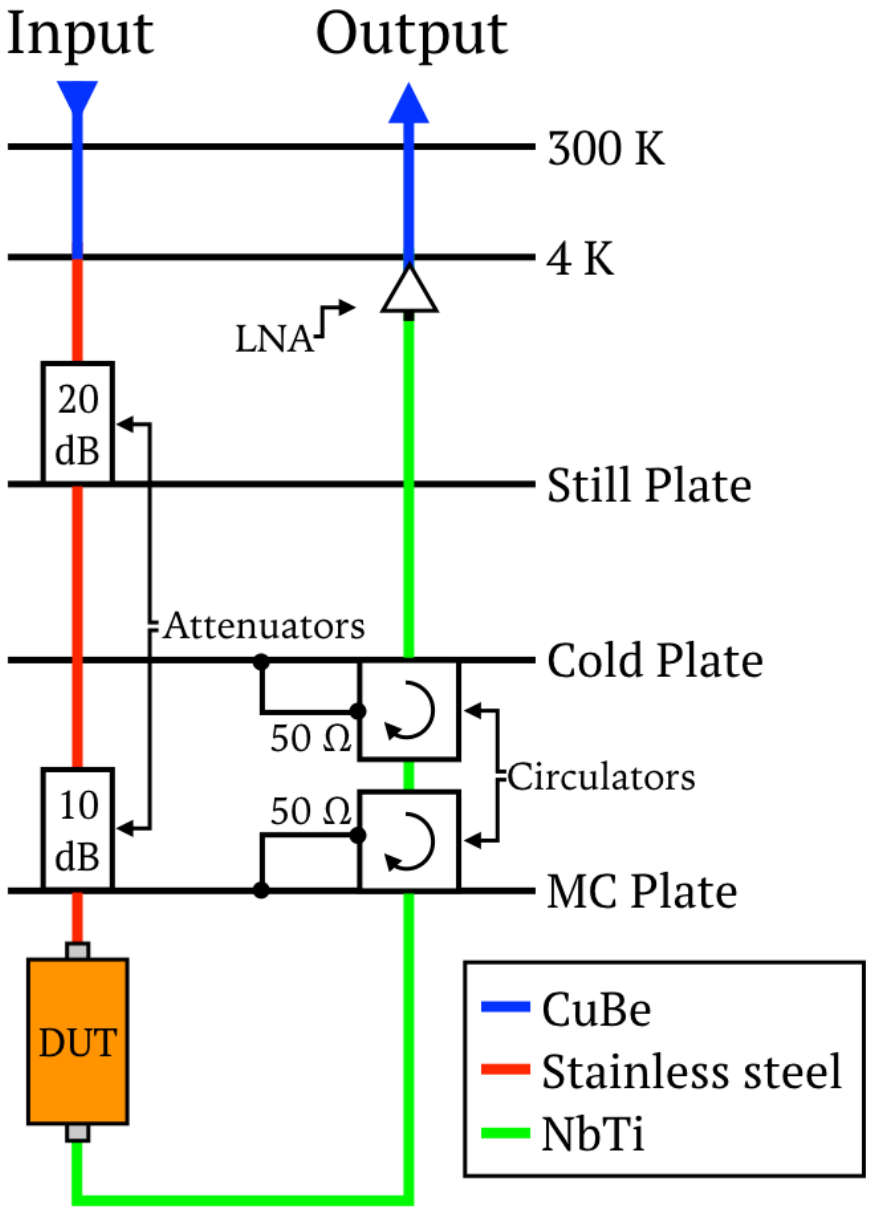

Figure 6.1: Diagram of the fridge circuitry. The colours represent the material of the coaxial line. The materials are chosen in order to minimise thermal conductivity whilst maintaining good electrical conductivity. The signal goes through 30 dB of attenuation split between the still and mixing chamber before reaching the device under test (DUT). It then passes through 2 circulators coupled to the mixing chamber and the cold plate respectively by a 50 Ω impedance before being amplified by the LNA. The lines themselves add additional frequency dependent attenuation. This is equal to 10 dB of attenuation on the stainless steel coaxial cable and 20 dB of attenuation on the CuBe coaxial cable at 6 GHz. This adds to 30 dB of line attenuation on the input circuit and 20 dB on the output circuit. The bandwidth is limited by the circulators to 3.5 GHz-7.5 GHz. The amplifier bandwidth is 4 GHz-8 GHz.

chamber, allowing the comparison with the MC thermometer. However it was not possible to use the noise thermometer during the experiment due to a heating fault. Since very little of the experiment was performed at milliKelvin temperatures, for the reasons discussed in section 2.3, the loss of the noise thermometry made little impact.

6.3 Experiment Circuit

The measurement circuitry is shown in figure 6.1. The input signal is attenuated at different stages. The output signal then passes through circulators before being amplified by the low noise amplifier (LNA). The output line is superconducting in order to minimise signal loss. The signal was sufficiently high that no further amplification was necessary at room temperature.

There is additional attenuation on the input circuit. The attenuators are Midwest microwave attenuators. They are mounted and thermally connected to the still and the MC and have respective attenuations of $20\,\mathrm{dB}$ and $10\,\mathrm{dB}$. The purpose of the attenuators is to thermalise incident radiation with the cooler stages of the refrigerator. Attenuators also allow for the thermalisation of the inner of the coax cable. Thermalisation of the attenuators with warmer stages allows heat to dissipate without loading the MC stage.

The circulators on the output line have a similar purpose to the attenuators; they prevent thermal radiation propagating towards the sample. Attenuators can not be used for this purpose on the output line as they would also attenuate the signal from the sample. Since circulators allow flow of current in only one direction they act as a suitable alternative. The circulators also prevent any reflected electrical signal from reentering the sample. The circulators are mounted to the MC and the cold plate. They are connected to the stage by a $50\,\Omega$ impedance. The measurement bandwidth is constrained by the circulators. These have a quoted operational range of $3.5\,\mathrm{GHz}$-$7.5\,\mathrm{GHz}$.

The amplifier is a Low Noise Factory cryogenic LNA (model LNF-LNC4.8C). It has a bandwidth of $4\,\mathrm{GHz}$-$8\,\mathrm{GHz}$ and a gain of $39\,\mathrm{dB}$ in this range. The maximum input RF power to the amplifier is $0\,\mathrm{dBm}$.

There are two additional room temperature amplifiers. Each of these have a gain of $45\,\mathrm{dB}$ and a bandwidth of $4\,\mathrm{GHz}$-$8\,\mathrm{GHz}$. After the initial characterisation of the sample the signal was sufficiently high that these were no longer needed.

6.4 Sample Mounting

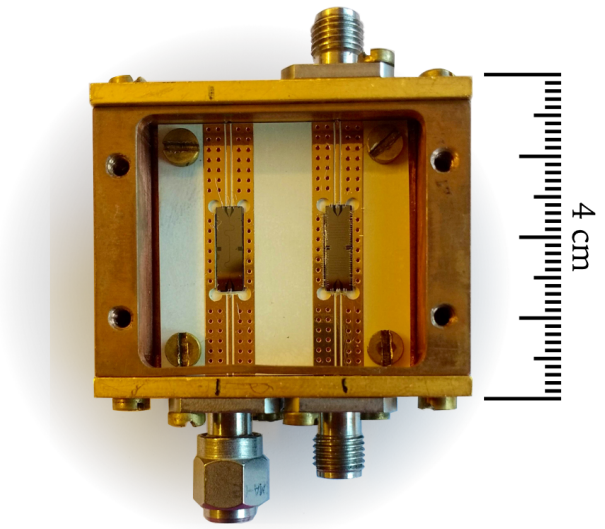

Figure 6.2: A photo of the sample box and sample. The sample is wire bonded to a PCB. The PCB is then connected to an SMA connector using Anritsu k-connectors. These are sprung contacts which slide over the centre pin of the SMA. The k-connectors allow good contact between the centre line of the SMA and the CPW. There is space for a second sample to be mounted in the box. This has been blanked off with a $50\,\Omega$ terminator.

The sample is wire bonded to a printed circuit board (PCB) and mounted in a copper sample box. The PCB is connected to the coaxial input and output lines by k-connectors. The k-connectors provide a sprung surface contact to the centre line of the PCB. They are rated to $40\,\mathrm{GHz}$, which exceeds the rating of the SMA connectors ($18\,\mathrm{GHz}$). Figure 6.2 shows a photo of the sample box. The sample box is designed to be of a size such that any resonances associated with the box are outside of the measurement bandwidth.

6.5 Sample

The sample is a resonator with an embedded nanoSQUID array. This section will discuss the resonator design and the fabrication of the nanoSQUIDs.

6.5.1 Design

The sample is a $\lambda/2$ niobium CPW resonator containing an array of 3 RF SQUIDs. This is shown schematically in figure 6.3. The SQUIDs are fabricated with a shared side, as in the experiment described in section 2.7.2. This is to constrain the phase drop of neighbouring SQUIDs in order to create a nearest neighbour coupling. The choice of a 3 SQUID array limits the hysteresis discussed in section 4. There are two nominally identical edge SQUIDs coupled to a single inner SQUID. In principle this results in only two system states at a given flux bias. The simpler design should avoid the irregular behaviour observed in the 32 SQUID arrays described in section 2.7.2.

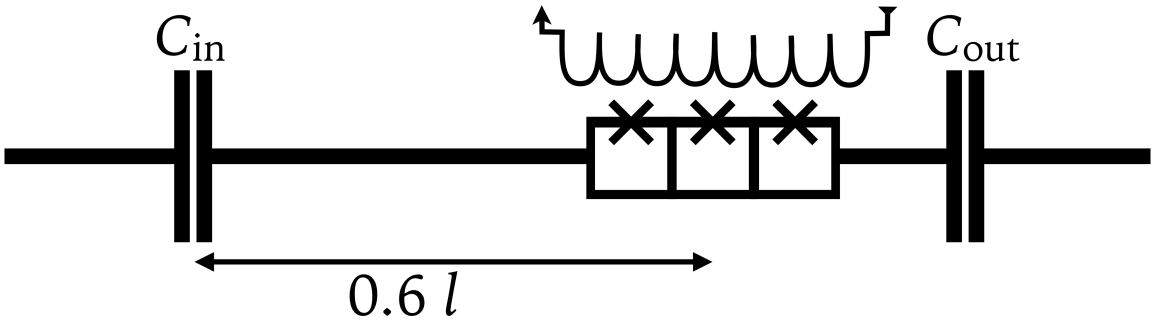

Figure 6.3: A schematic of a resonator containing an array of 3 RF SQUIDs. The SQUIDs are not in the centre of the resonator, allowing coupling to the second mode.

The CPW is designed to have an impedance of $50\,\Omega$. This is achieved with a centre line width of $w = 20\,\mu\text{m}$ and a centre line-ground plane separation of $s = 0.52w$. It is made of a $200\,\text{nm}$ thick layer of niobium sputtered on to a Si/SiO_2 wafer. This has an effective permittivity of $\varepsilon_{\text{eff}} = 6.4$.

The transmission line is interrupted at 2 points by interdigital capacitors to form a resonator. The capacitors are asymmetric in order to preferentially scatter radiation in the forward direction. The input capacitor has a capacitance of $1\,\text{fF}$. The output capacitor has 5 fingers and a capacitance of $30\,\text{fF}$. The resonator layout and the input and output capacitors are shown in figure 6.4.

The capacitance and inductance per unit length can be found using equations 2.23 and 2.22. They are found to be $L' = 2.43 \times 10^{-7}\,\text{Hm}^{-1}$ and $C' = 1.75 \times 10^{-10}\,\text{Fm}^{-1}$. The length of the resonator is $1.3\,\text{cm}$. This corresponds to a resonant frequency of $f_{\text{res}} = 5.96\,\text{GHz}$.

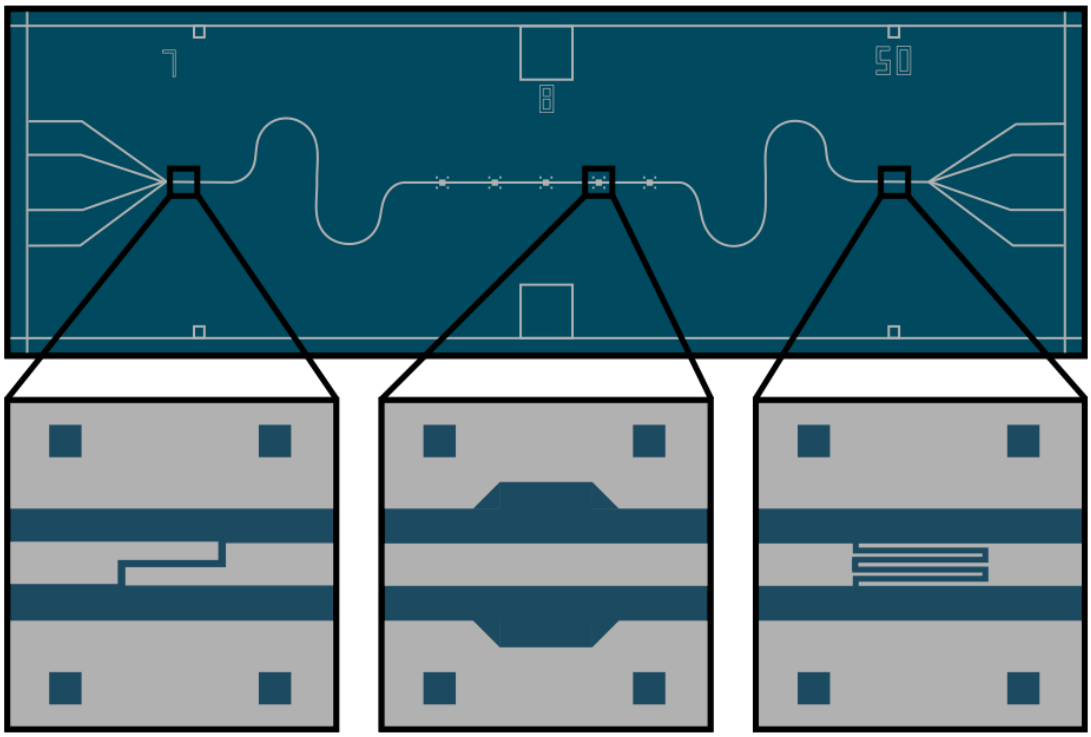

Figure 6.4: Top: The layout of the CPW resonator showing. Left: The input capacitor with a capacitance of $1\,\mathrm{fF}$. Centre: Guide marks for EBL. Right: The interdigitated 5 finger output capacitor with a capacitance of $30\,\mathrm{fF}$. The resonator length is $1.3\,\mathrm{cm}$. The centre line width of $w = 20\,\mu\mathrm{m}$ separated from the ground plane by a spacing $s = 0.52w$ give an approximate $50\,\Omega$ impedance.

6.5.2 Fabrication

The SQUIDs are formed using electron beam lithography (EBL) to produce a high resolution mask on top of the Nb CPW sample. The mask is exposed to define SQUID loops in the central conductor of the resonator. The material unprotected by the mask is then removed by a reactive ion etch. Rather than junctions, the nonlinearities in the SQUIDs are Dayem bridge [34] style nanobridges. These are also formed using EBL to define a constriction in one of the arms of the loop. It was decided to use nanobridges as opposed to Josephson junctions because this allowed us to fabricate the sample entirely from niobium. Fabricating the sample entirely from niobium allows us to perform measurements of the SQUIDs in liquid helium as well as removing any artefacts introduced by surface effects caused by

aluminium integration.

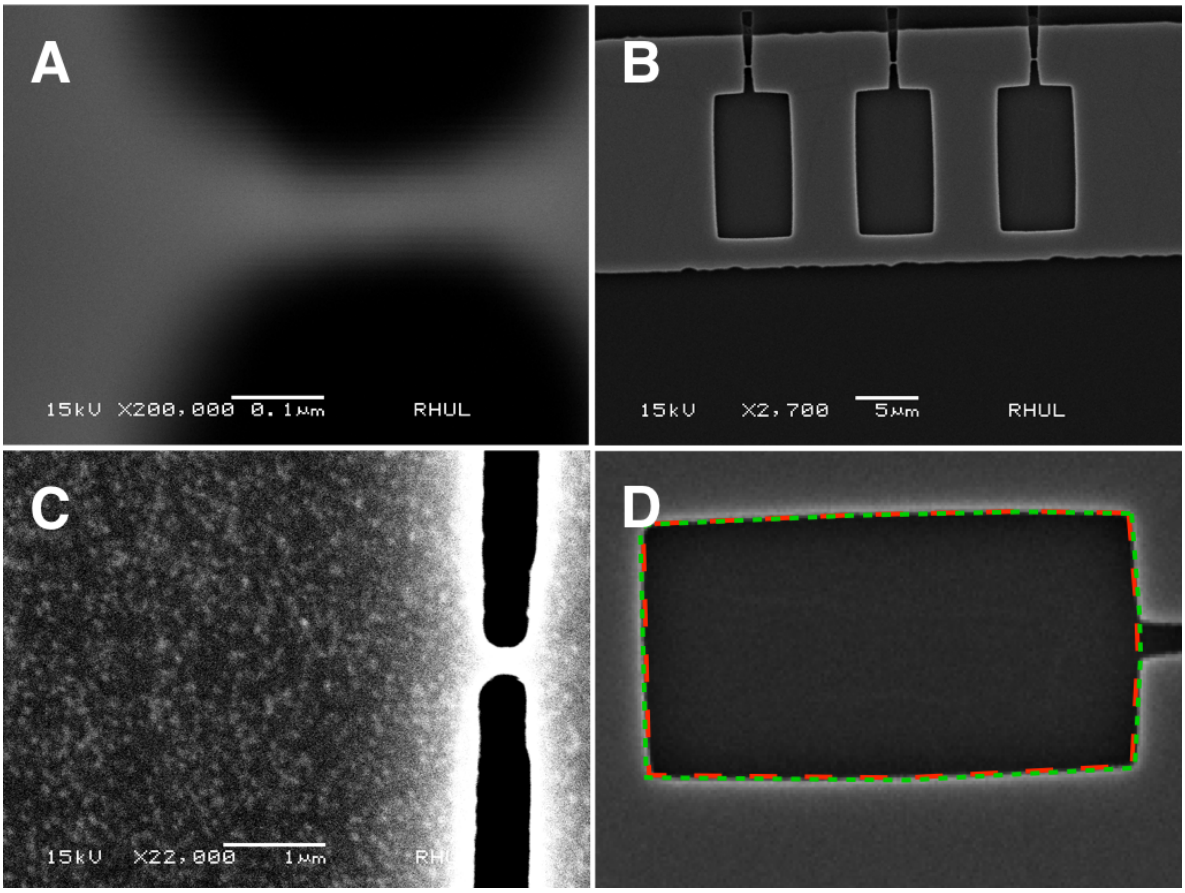

Figure 6.5: SEM pictures of the measured sample. A: One of the bridges in the array. The bridge was found to be of width $50\,\mathrm{nm}$. The physical length of the bridge is of order $300\,\mathrm{nm}$. B: The array. 3 RF nanoSQUIDs were etched into the centre line of the resonator. The SQUID loops have dimensions of $5\,\mu\mathrm{m}$ by $10\,\mu\mathrm{m}$, giving a loop area of $50\,\mu\mathrm{m}^2$. This corresponds to a geometric inductance of $L_\mathrm{g} = 1.11 \times 10^{-11}\,\mathrm{H}$. C: One of the trial iterations of the bridges. D: A single loop in the array. In order to quantify the deviation in area the outline of the smallest loop is traced in red (long dash) whilst the best fit outline of the largest loop is traced in green (short dash). The difference in these areas is found to be around 2%.

The behaviour of nanobridges is not as well understood as that of Josephson junctions. This is because historically their small size has made them relatively difficult to fabricate. Improvements in resolutions of EBLs and the introduction of techniques such as focussed ion beam lithography have somewhat improved this. The choice of nanobridges then also allows us to develop our understanding of nanobridge devices.

State of the art EBLs are able to pattern features at nanometre precision. The resolution of the EBL used was somewhat lower than this, meaning that direct writing was not possible. We therefore

used a feature of resist bilayer regression in order to define the bridges. The method is described fully in [71]. It was found that exposing and developing a copolymer PMMA bilayer stack consistently left a thin barrier of material behind. The thickness of the bridge was found to be of order $50\,\mathrm{nm}$ which is comparable to the coherence length at $T = 0\,\mathrm{K}$ in niobium which is $38\,\mathrm{nm}$.

In order to fabricate the junction we used a copolymer PMMA bilayer stack. The PMMA acts as a high resolution mask. This was exposed on the RHUL Jeol 6460 EBL system, with an accelerating voltage of 30 keV. The copolymer and PMMA receive the same dose. The dose is dependent on the size of the feature being exposed. The sample is then developed to saturation with water.

Once the mask has been developed we etch isotropically with SF_6/Ar to remove the exposed niobium using the Oxford Instruments Plasmalab 80 Plus. The sample is then cleaned with acetone and isopropanol.

Figure 6.5 shows the nanoSQUID array as well as details of the bridges. The bridges, shown in panel A, are of a consistent width of $50\,\mathrm{nm}$. The length is approximately $300\,\mathrm{nm}$. To fully quantify the length of the bridge it is necessary to study the spatial distribution of the phase drop [37]. From the discussion in section 2.3 we would expect these bridges to be best described in the long bridge limit.

The SQUID dimensions are $5\,\mu\mathrm{m}$ by $10\,\mu\mathrm{m}$. This results in a geometric inductance of $L_\mathrm{g} = 1.11 \times 10^{-11}\,\mathrm{H}$. Shelly et al [2] reported critical currents of $71\,\mu\mathrm{A}$ for nanobridges of similar dimensions. The geometry of our SQUID loops combined with the expected value of I_c are chosen to give $\beta_\mathrm{L} \approx 1$. It should be noted that the critical current is highly sensitive to the precise geometry of a nanobridge. For a resonator of total inductance $L_\mathrm{res} = 2L'l/n^2\pi^2 = 6.41 \times 10^{-10}\,\mathrm{H}$ this gives a participation ratio of $a = 0.017$ for each SQUID. For reference, the frequency modulation curve for a SQUID containing a single Josephson junction with similar parameters is shown in figure 2.4.

The deviation in the loop area can be quantified by fitting the circumference of the loop of the smallest and largest SQUID. This is shown in panel D of figure 6.5. The deviation was found to be of order 2%. The deviation is important since it impacts the coupling of the SQUID to an external magnetic field. If the deviation is large it can result in a difference in periodicity of the frequency modulation curves for each SQUID in the array. This results in a beating effect (see chapter 3). It will be necessary to distinguish the beating arising due to the deviation in loop area from that arising as a result of the coupling.

Chapter 7

Experimental Results

In order to verify the model proposed in chapter 4 we performed an experiment on a sample designed to avoid the chaotic hysteresis observed in longer SQUID arrays, but still exhibiting coupling. The aim was to simplify the behaviour of the sample by including only 3 SQUIDs in a single array, thus limiting the spread of phases produced by the coupling. The model described in chapter 4 may be generalised to describe nanobridge SQUIDs by replacing the current phase relationship of the Josephson junction by that of the nanobridge.

7.1 Characterisation in Liquid Helium Dewar

The sample was cooled to $4.2\,\mathrm{K}$ using a liquid helium Dewar to perform an initial characterisation before installation on the dilution refrigerator. The sample, in the sample box shown in figure 6.2, was mounted to a dipping probe and submerged in liquid helium.

7.1.1 Transmission Spectra

We performed transmission, S_{21}, measurements using an Anritsu 37397C Vector Network Analyser (VNA) of the sample and probe both at room temperature and when submerged in liquid helium. The room temperature spectra can be taken as the background describing the behaviour of the circuit and the sample box. Once the system is in the superconducting state the resonance appears as a peak above this background spectrum. The spectra are shown in figure 7.1. The port 1 power of the VNA was set to $0\,\mathrm{dBm}$ for both the room temperature (red) and liquid helium temperature (blue) sweeps. There was

no attenuation besides that of the circuit itself, which is equal to $14\,\mathrm{dB}$. The fundamental mode of the resonator was found at $f_{\mathrm{res}} = 5.89\,\mathrm{GHz}$.

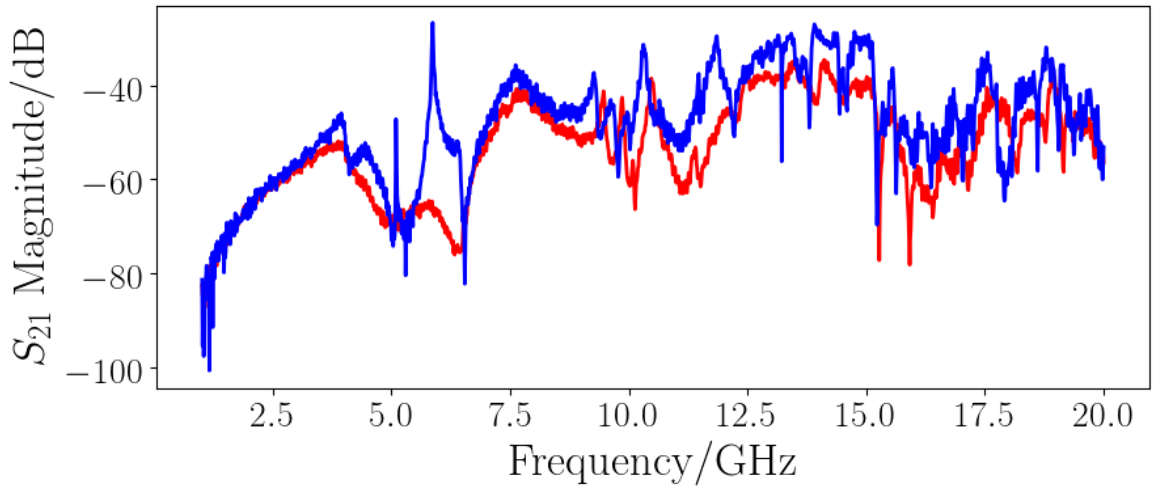

Figure 7.1: The S_{21} transmission spectra of the CPW resonator containing an array of 3 RF nanobridge SQUIDs at room temperature (red) and at $4.2\,\mathrm{K}$ (blue) in a helium transport Dewar. The measurement was performed using a VNA with a port 1 power of $0\,\mathrm{dBm}$. The circuit was the same for both measurements. When the sample is superconducting the fundamental resonance at $5.89\,\mathrm{GHz}$ is easily distinguishable from the background of the circuit. The first harmonic, near $12\,\mathrm{GHz}$ is also present, although the lower quality factor makes this feature less apparent.

The features at frequencies higher than $13\,\mathrm{GHz}$ are attributed to resonances supported by the sample box. These frequencies are outside of the measurement bandwidth of the fridge circuit. Since it does not respond to power or field, the sharp peak at $5\,\mathrm{GHz}$ is not believed to be attributable to the resonator.

7.1.2 Power Sweep

We are able to probe the nanobridge SQUID array by measuring the response of the fundamental resonance to increasing drive power. The cubic term of the nonlinear current phase relation of the nanobridges can be used to realise a Duffing oscillator. As the drive power is increased the resonance becomes asymmetric, with the resonance shifting to higher or lower frequencies depending on the sign of the cubic coefficient of the restoring force. This is described in section 2.6.1.

Figure 7.2 shows a power sweep of the resonator when submerged in liquid helium in a transport Dewar. The sweeps are offset vertically for clarity. At a power of $-36.3\,\mathrm{dBm}$ the resonator undergoes a volcano bifurcation. The increment between power sweeps is $0.4\,\mathrm{dBm}$. At a power of $-35.9\,\mathrm{dBm}$ the resonator exhibits a Duffing bifurcation. As the power is increased further the system exhibits

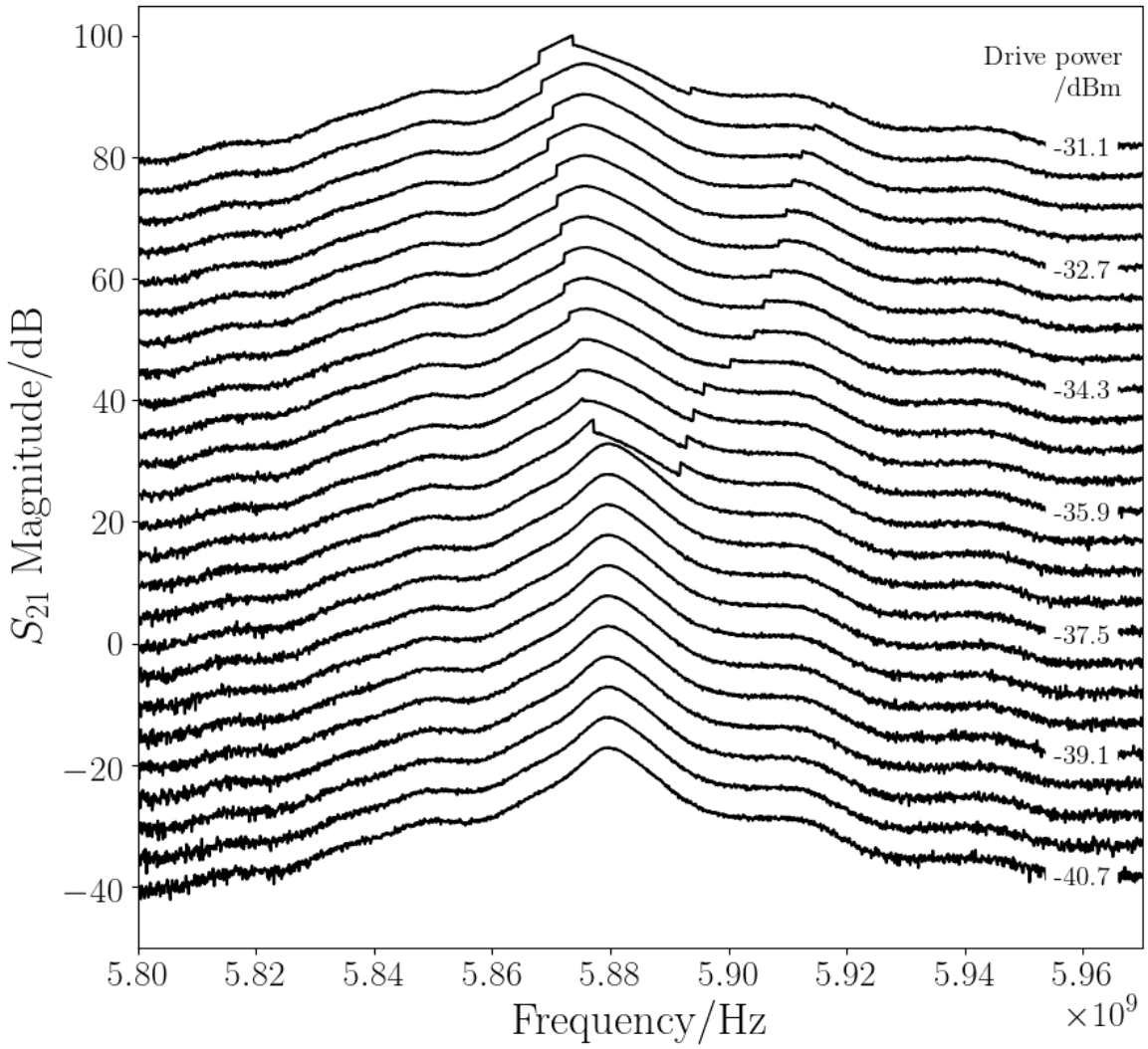

Figure 7.2: A power sweep of a 3 nanobridge SQUID array in a resonator. This sweep was performed in a helium transport Dewar. The spectra are offset vertically for clarity. The drive power at the sample for different sweeps is annotated on the plot. As the power is increased the sample undergoes a volcano bifurcation then a Duffing bifurcation. At very high powers the sample exhibits different bifurcations at different frequencies. The first bifurcation occurs at a power at the sample of $-36.3\,\mathrm{dBm}$.

multiple bifurcations. The crater of the volcano widens at high power, as a larger frequency window of the resonant peak is above the threshold power.

The second mode did not bifurcate at any power level. This is because the array is located near the centre of the resonator so that the coupling of the nonlinearity to the even modes is weak. The lack of bifurcation in the modes weakly coupled to the nanobridge SQUID array means that the bifurcation is unlikely to be the result of the nonlinear kinetic inductance of the bare resonator.

7.2 Characterisation in Dilution Refrigerator

After initial characterisation of the sample in a liquid helium Dewar it was installed onto the dilution refrigerator circuit discussed in section 6.1. The spectra was then reinvestigated.

7.2.1 Transmission Spectra

The spectra of the fridge circuit and sample when cooled to $4.2\,\mathrm{K}$ (blue) and at room temperature (red) are shown in figure 7.3. The room temperature measurement has additional room temperature amplification after the LNA in order to compensate for the output circuit becoming normal. The signal is attenuated by the circulators and amplifiers outside of the measurement bandwidth. Figure 7.4 shows

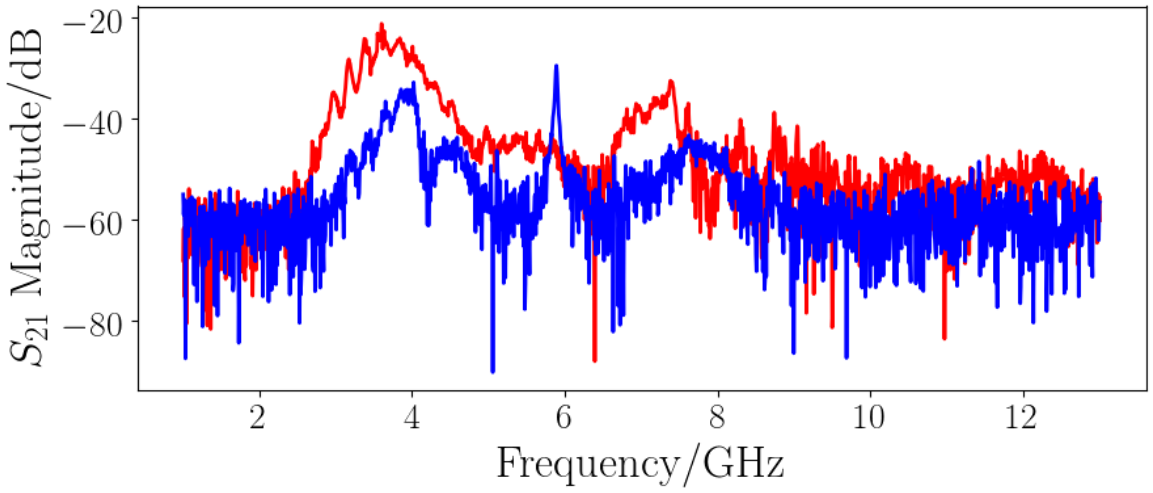

Figure 7.3: The S_{21} transmission spectra of the CPW resonator containing an array of 3 RF nanobridge SQUIDs once installed on the fridge circuit at $4.2\,\mathrm{K}$ (blue) and at room temperature (red). Additional amplification is added for the room temperature sweep. At low temperature the superconducting resonance is clearly visible. Outside of the range $3.5\,\mathrm{GHz}$ to $7.5\,\mathrm{GHz}$ the signal is attenuated by the circulators.

an S_{21} transmission measurement of the fundamental mode. At the sample the power was $-77\,\mathrm{dBm}$. Overlaid on the experimental data is a Fano resonance fit. Fitting the function allows us to find the quality factor and resonant frequency of the sample. The quality factor, Q, was found to be 400. A Fano resonance describes a resonator with discrete modes coupled to a continuum of states [55]. This results in an asymmetry. In this case the Fano parameter was $q = 2 \times 10^6$. In the limit $|q| \gg 1$ the Fano function resembles a Lorentzian function. This is indicative of a uniform ground plane potential. The conversion of the power scale from decibel-milliWatts to Watts allows for the removal of noise

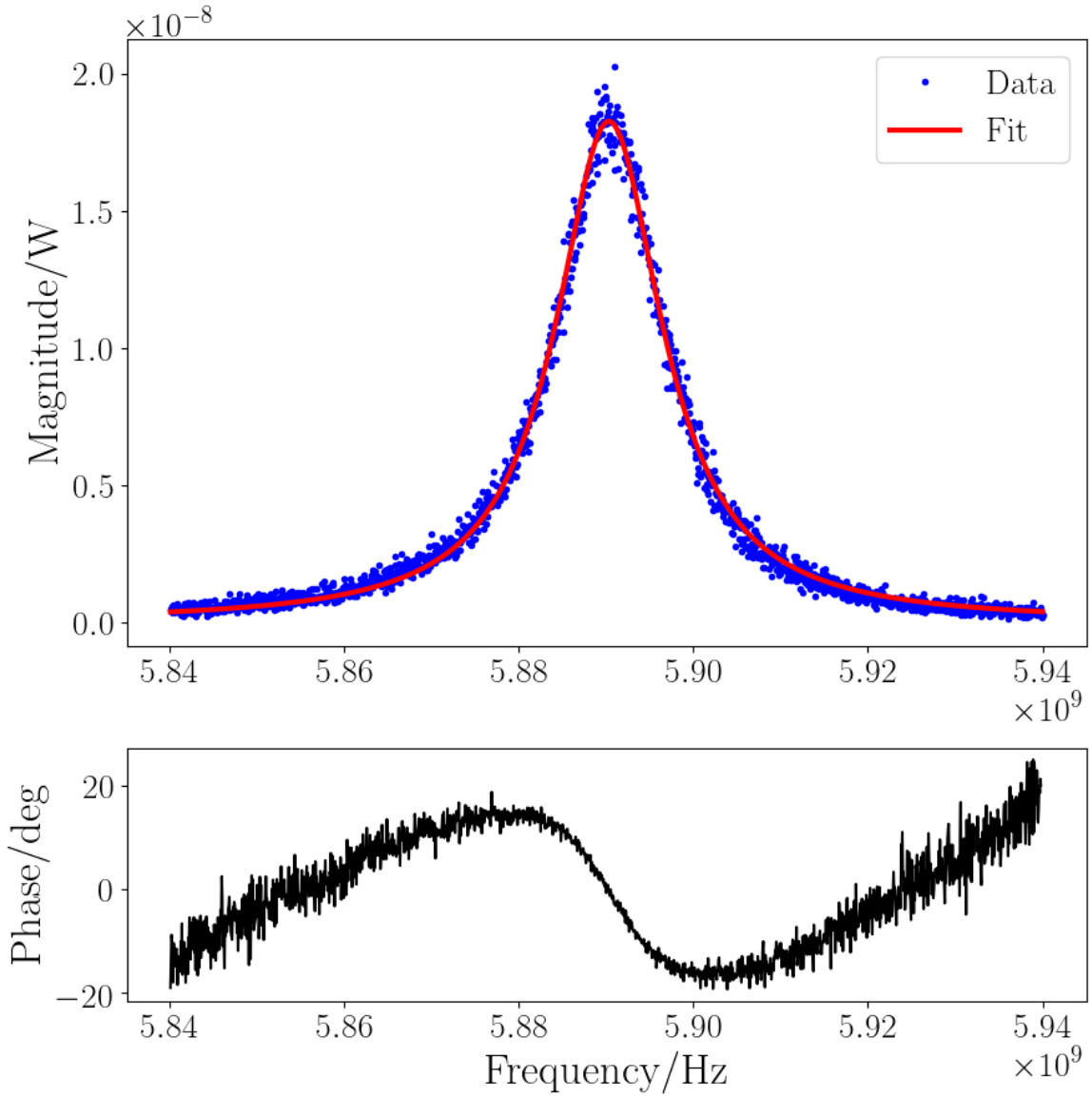

Figure 7.4: Upper panel: An S_{21} measurement of the fundamental mode at $4.4\,\mathrm{K}$ with a power of $-77\,\mathrm{dBm}$ (blue dots). The curve has been fitted with a Fano resonance (red line). The data is well fitted with a quality factor of 400 and a resonant frequency of $5.89\,\mathrm{GHz}$. The asymmetry parameter is 2×10^6, which is reflected in the near Lorentzian line-shape. Lower panel: The phase shift of the signal on resonance.

fitting parameters from the fitting equation, reducing covariance. The lower panel shows the phase data.

7.3 Frequency Modulation

The inductance of a SQUID is dependent on the bias field. Since the resonant frequency of the sample is a function of the inductance, we are able to accurately probe the inductance of the SQUID by measuring the resonant frequency of the resonator. We expect to see a periodic modulation in the resonant frequency of the sample as bias field is swept. The coupling between SQUIDs is expected to add an additional beating effect to this modulation. The additional beating effect is caused by the inner and edge SQUIDs of the array being subjected to a different effective field.

Frequency modulation was achieved using an external coil. The coil was mounted on the sample box. Current was supplied to the coil with a Yokogawa 7651 voltage source. The current was limited by a current limiting resistor at room temperature. The resistance was varied depending on the requirements of the measurement. Smaller resistors allow a greater range of magnetic fields to be applied to the sample, whilst larger resistors increase the current stability.

Hysteresis in the frequency modulation curve will arise if, according to the uncoupled theory, $\beta_{\mathrm{L}} > 1$. The coupling may alter this condition. Hysteresis can be observed by comparing the frequency modulation curve when swept in the forward and reverse directions.

In this section we will discuss the results from two methods of measuring the frequency modulation curve, one relying on S_{21} measurements performed with the VNA, and another performed with a constant wave source and a spectrum analyser.

7.3.1 VNA Measurements

The frequency modulation curve may be measured by measuring the S_{21} transmission at differing coil current values. The line shape is then fitted with a Fano function and the resonant frequency extracted. The coil current will be swept in the forward and reverse directions.

We will explore the dependence of the behaviour of the nanobridges on temperature.

Figure 7.5 shows the measured frequency modulation curve in the positive and negative directions at $4.5\,\mathrm{K}$. The current limiting resistor used here was small ($500\,\Omega$), allowing the broader features of the curve to be investigated. We notice that there is some variation in resonant frequency as a function of applied field. The periodicity of the behaviour is around an order of magnitude too large to be associated with periodic modulation of the SQUID inductance. Therefore the behaviour is attributed

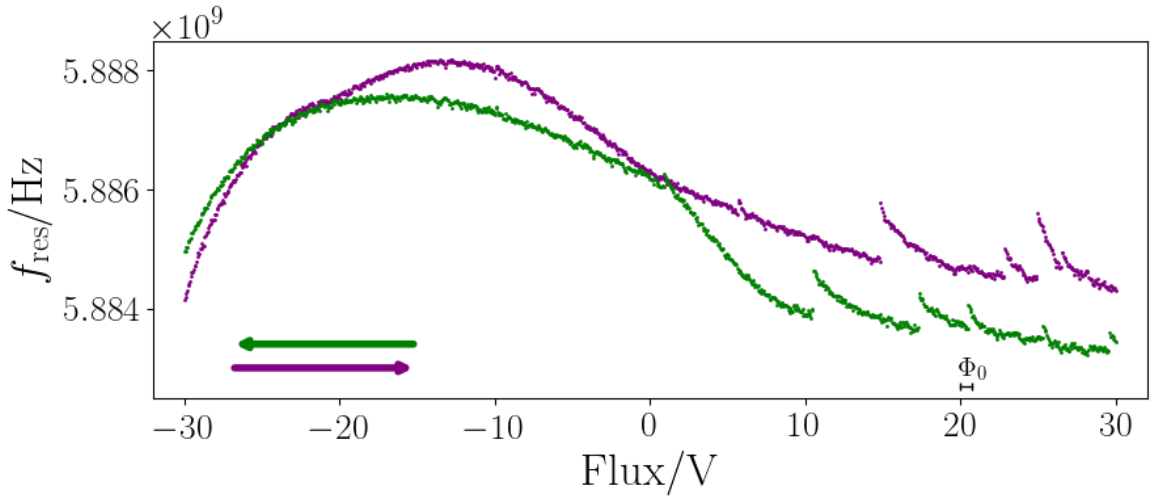

Figure 7.5: Frequency modulation of the sample at $4.5\,\mathrm{K}$. For this sweep a current limiting resistor of $500\,\Omega$ was used. The choice of resistor allows us to view the wider background behaviour of the sample. We note that there is a wide, non-periodic modulation of the resonant frequency. This is possibly due to flux vortices in the ground plane. We also note the discontinuous jumps in the resonant frequency above a coil voltage of $10\,\mathrm{V}$. The cause of the jumps is not obvious, the period is much larger than the period of the SQUID behaviour. A flux quanta is marked on the figure for comparison. The behaviour is hysteretic.

to background behaviour of the resonator. The variation in temperature during the sweep was small, around $0.05\,\mathrm{K}$, or 1%. Since we are not near T_c this is not sufficient to explain the background. It is believed that this background behaviour is instead attributable to the penetration of flux vortices into the ground planes of the sample. The background behaviour results in a variation of frequency of order $3\,\mathrm{MHz}$. With a greater participation ratio (see, for example, the SQUID modulation described in section 3) this behaviour would be dominated by the SQUID modulation. The modulation of the SQUIDs in this sample is reduced due to the relatively low nonlinearity of the current phase relation. The background behaviour is hysteretic.

In order to ensure that the observed behaviour is not the result of noise, a background measurement was performed with the same set up. This is shown in figure 7.6. Instead of being sent an array of voltage values, the voltage source was sent only zero values. The sweep was taken over the same time period. We can see that it is flat, with a width of about $0.1\,\mathrm{MHz}$. This is about half of the depth of the frequency modulation.

Figure 7.7 shows two measured frequency modulation curves taken with nominally identical conditions. Both curves are taken in the positive direction. The curves are not identical. The difference

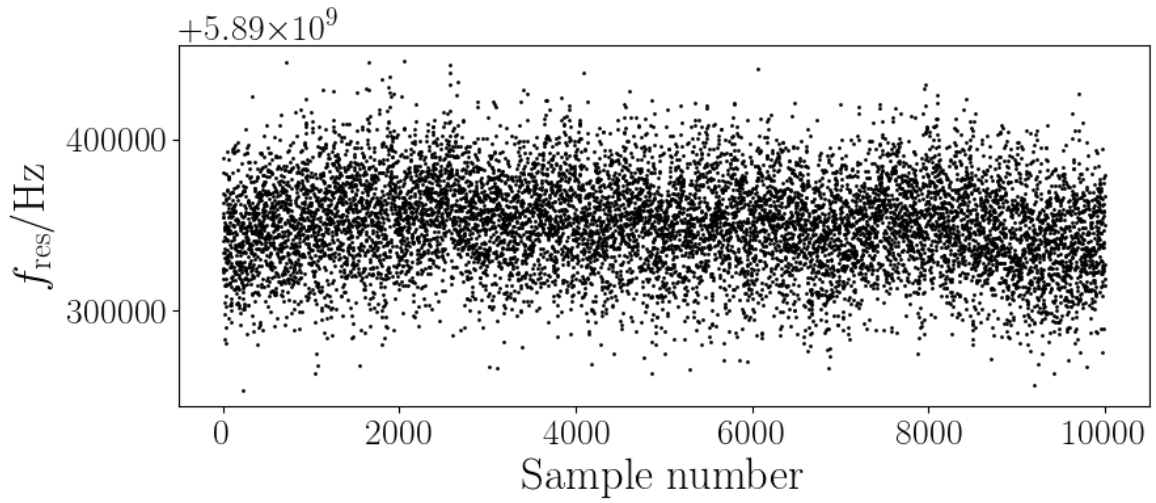

Figure 7.6: In order to distinguish the background behaviour from noise a sweep was performed where the experimental setup was identical, but the coil voltage source was held at $0\,\mathrm{V}$. The time over which the sweep was taken was the same as for the other sweeps. The sweep duration was 4 days. The sweep was performed at $4.4\,\mathrm{K}$.

is likely the result of a high degree of hysteresis. If there are many allowed states in a small energy band, a small amount of noise may push the system into a different state, which would alter the subsequent system evolution. The lower panel shows the effect of removing the slow flux dependence which is not the result of SQUID behaviour. The behaviour is removed by averaging a over a range of many flux quanta and subtracting the averaged curve from the raw data. We then apply a further average over a period much less than a flux quanta to reduce system noise. The background subtraction average is performed over 200 data points and the noise subtraction average is performed over 10 points. Once this has been performed the SQUID behaviour is isolated. It is clear that this behaviour is hysteretic. There also appears to be a broader modulation. This may be attributable to deviation in the SQUID loop area or dispersion caused by nearest neighbour coupling. The deviation in loop areas is quantified in figure 6.5. It is estimated to be 2%. This results in a beat period of 50 flux quanta. On the scale of figure 7.7, this corresponds to a period of approximately $115\,\mathrm{V}$. A zoom of the frequency modulation curve is shown in figure 7.8.

The coupling is estimated to be $\alpha = 1/3$ from geometric arguments. The resultant beat period is $3\Phi_0/\left(2A^{(1)} - A^{(2)}\right)$ where $A^{(i)}$ is defined by equation 4.16. As shown in figure 4.2, at $\alpha = 0.3$, $\left(2A^{(1)} - A^{(2)}\right) \approx 1.3$. The beat period is therefore $3\Phi_0/1.3 \approx 2.3\Phi_0$. The period of the modulation of each individual SQUID has also been altered. This means we may observe multiple fringes in a

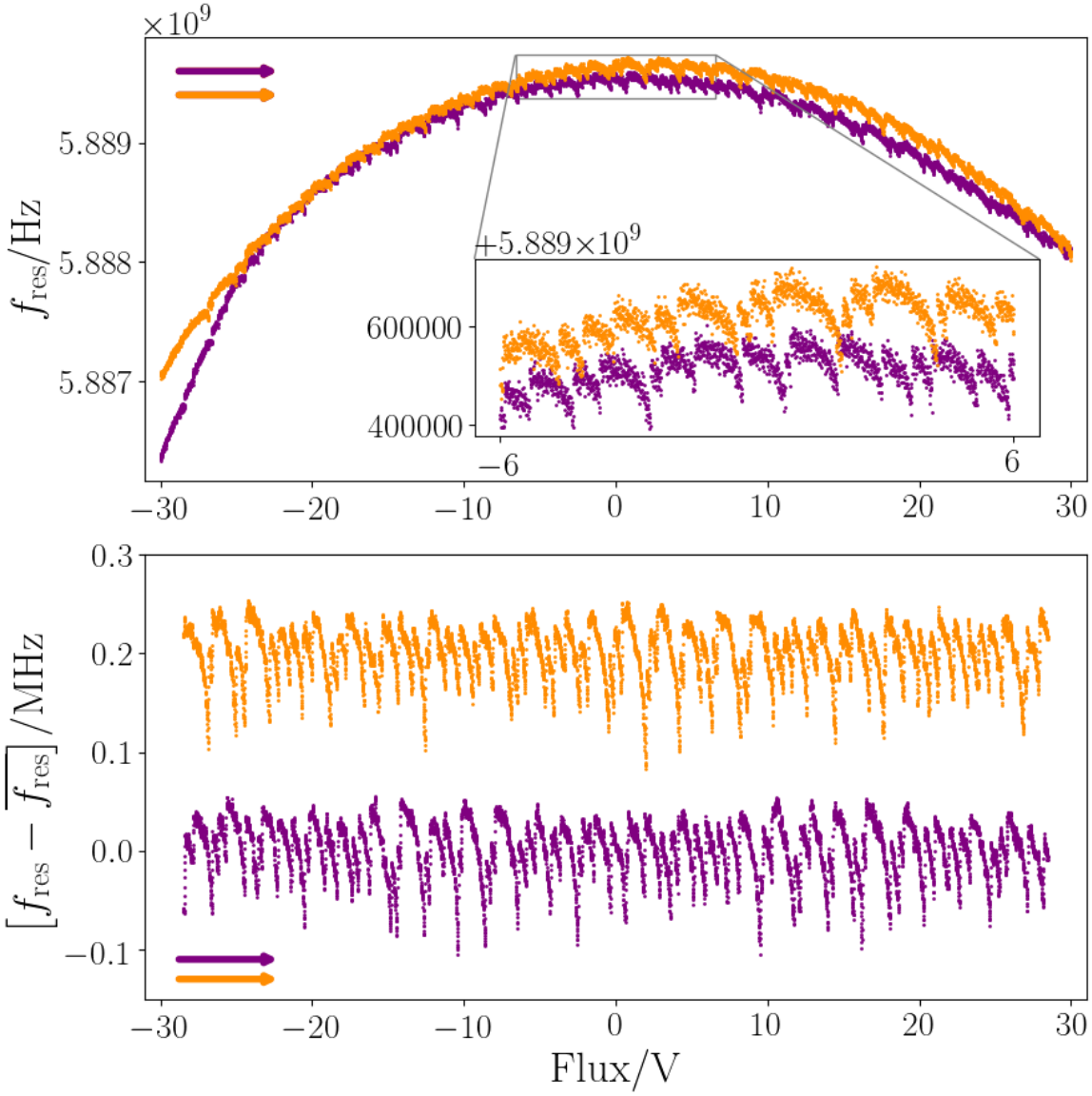

Figure 7.7: Frequency modulation of the sample at 4.6 K. For this sweep a current limiting resistor of 1.501 kΩ was used. This plot illustrates the repeatability of the effect. Both the orange and purple sweeps were taken in the positive direction and are designed to be identical. The differences between the curves are attributed to the high degree of hysteresis inherent in the system. The upper panel shows the raw data. In the lower panel the background behaviour has been removed by averaging adjacent points and subtracting the averaged curve from the data set. The number of averaged points is 500. This is much larger than a flux quanta. To reduce noise we also apply a 10 point floating average. The curves are offset vertically for clarity. They start to resemble the more recognisable flux dependence of an RF SQUID.

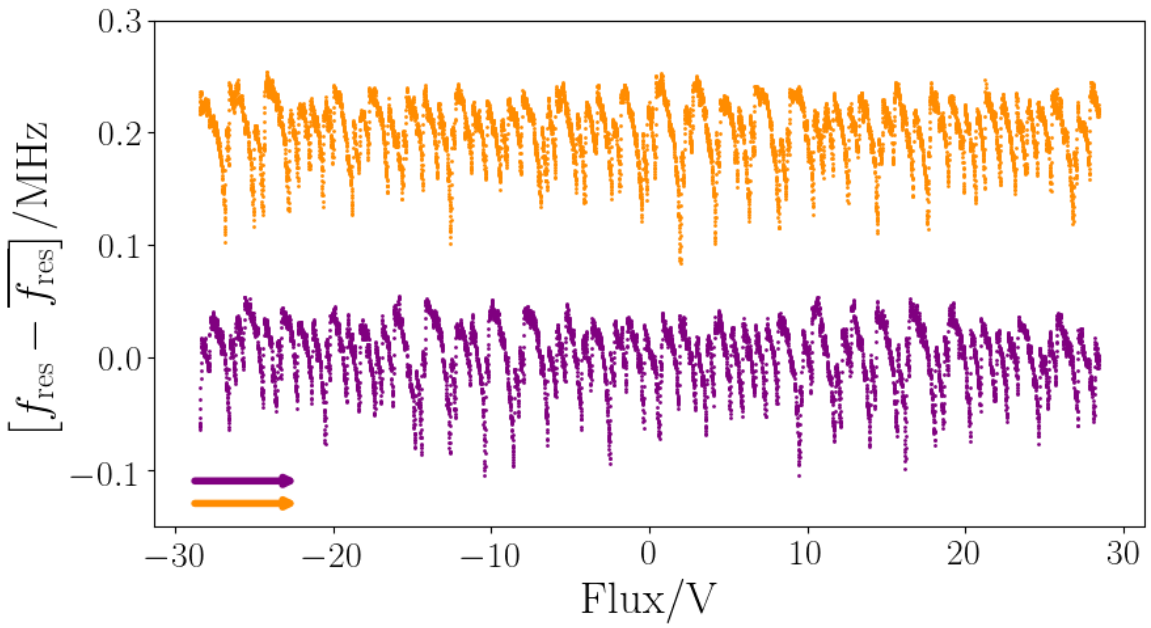

Figure 7.8: An enlargement of the frequency modulation of the sample at $4.6\,\mathrm{K}$ after the background has been subtracted by averaging over many flux quanta.

single flux quanta. The period is given by,

$$\begin{cases} P_1 = \Phi_0/\left(1+\alpha A^{(2)}\right), \\ P_2 = \Phi_0/\left(1+2\alpha A^{(1)}\right), \end{cases} \tag{7.1}$$

where P_1 and P_2 are the periods of the outer and inner SQUID respectively. With a coupling of $\alpha = 1/3$, $A^{(1)} = 12/7$ and $A^{(2)} = 15/7$. This gives $P_1 = 7\Phi_0/12$ and $P_2 = 7\Phi_0/15$. The number of observed fringes is dependent on the smaller period, P_2. This means that in a beat period of $2.3\Phi_0$ we expect to see around 5 fringes.

The beat pattern appears to be more complex than that arising from interference of only 2 waves. This may be because the measured frequency modulation curve is further complicated by the hysteresis.

In order to examine this further, we take the FFT of the background subtracted dataset shown in the lower panel of figure 7.7. The FFT is shown in figure 7.9. According to the theory of coupled SQUIDs, the ratio of the flux frequency of the inner and outer SQUIDs should be $\left(1+2\alpha A^{(1)}\right)/\left(1+\alpha A^{(2)}\right) = 1.25$. The first 2 peaks of the FFT are at $(0.41 \pm 0.02)\,\mathrm{V}^{-1}$ and $(0.32 \pm 0.02)\,\mathrm{V}^{-1}$. The ratio of these is 1.3 ± 0.1. Taking the ratio removes the need to normalise against a flux quanta. These results are in

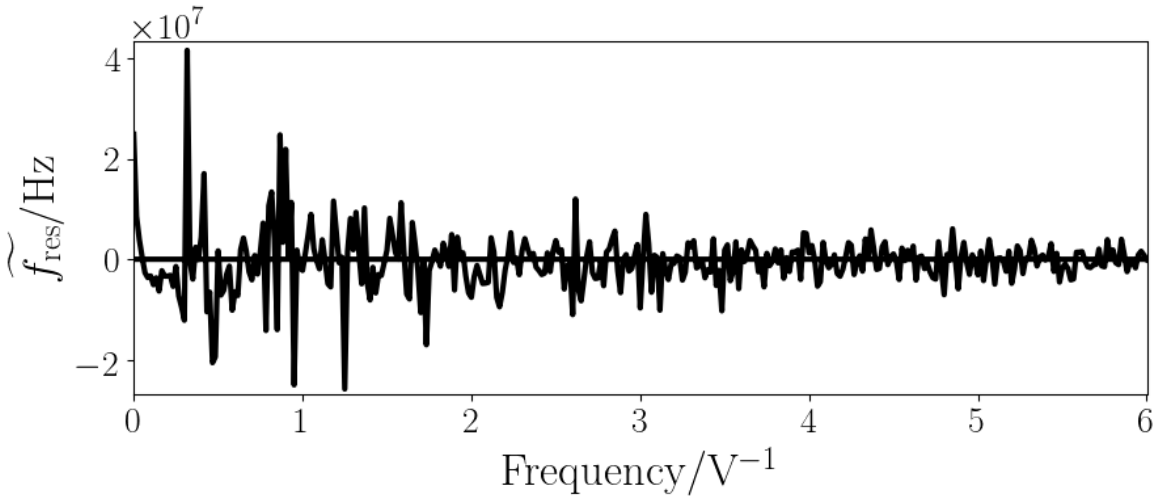

Figure 7.9: An FFT of the background subtracted frequency modulation curve. This allows us to identify the peaks corresponding to the beating effect. There is reasonable agreement between the position of the peaks in the FFT and the expected beat period based on the coupled SQUIDs theory.

reasonable agreement. For contrast, attributing the beat to deviation in SQUID loop area alone leads to an expected frequency ratio of 1.02.

Due to the edge effects the frequency of the edge SQUID will be lower than that of the inner SQUID. This means that the first peak in the FFT corresponds to the edge SQUIDs and the second peak corresponds to the inner SQUID. Since there are 2 edge SQUIDs we expect the amplitude of the first peak to be twice that of the second. This is indeed the case in the FFT of the data however the height of each peak is highly sensitive to the resolution of the x axis.

In order to attempt to reduce the flux noise we increase the current limiting resistor to $11.85\,\mathrm{k}\Omega$. The resultant measured frequency modulation curve in the forward (purple) and reverse (green) directions is shown in figure 7.10. We are able to see the form of the modulation in more detail. We note that it is highly hysteretic, beginning to resemble a sawtooth rather than a smooth curve. This is due to the geometry of the fabricated nanobridges, which are likely to have a weakly nonlinear, hysteretic current phase relation [72]. The current phase relationship may be altered by operating the sample in different temperature ranges.

We are also able to take the FFT of this data set and compare the ratio of the frequencies of the first two peaks. However, since there are a reduced number of periods present the flux-frequency step size is increased, leading to larger uncertainties. This gives 2 ± 1. By changing the resistor we have

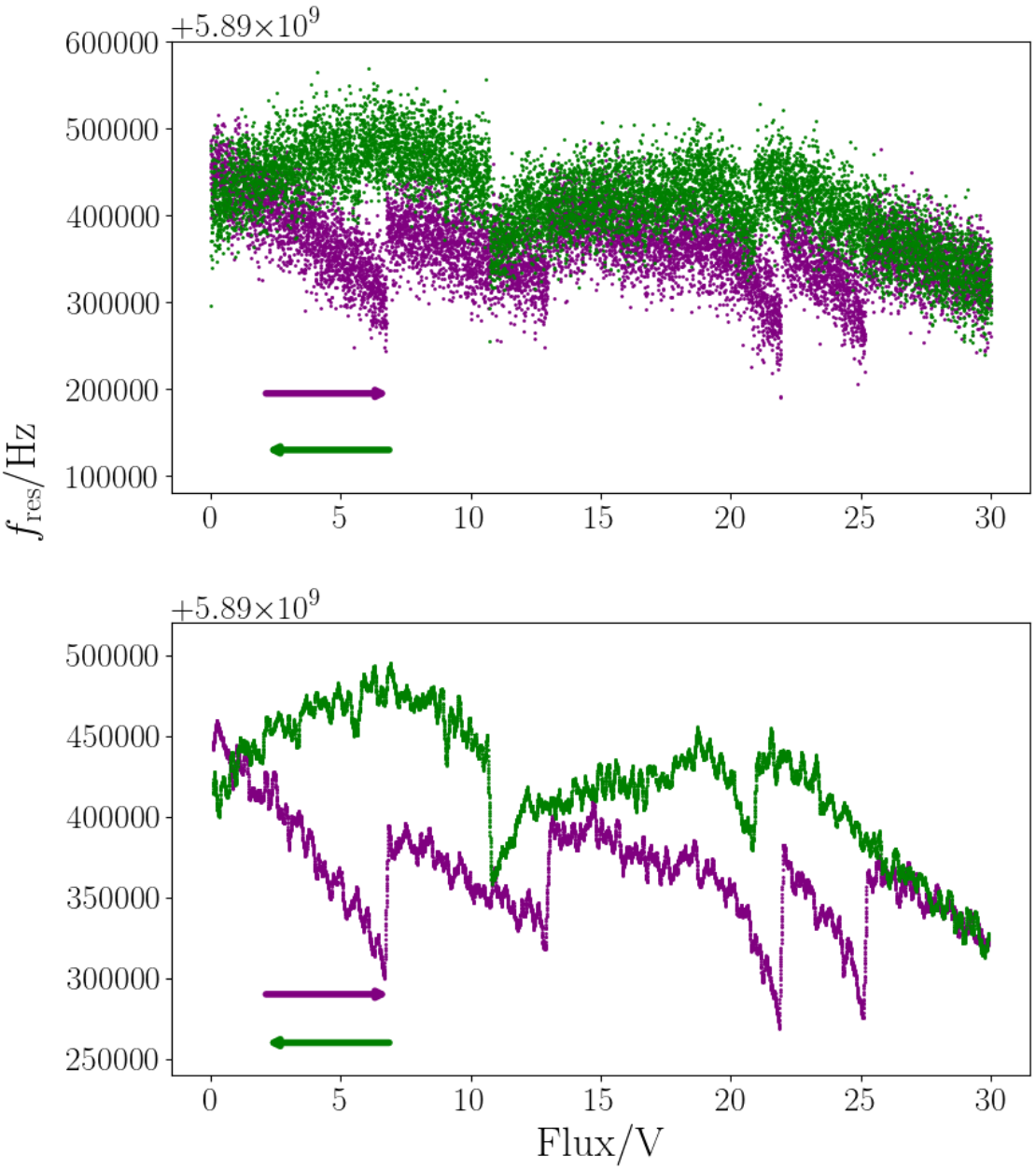

Figure 7.10: The measured frequency modulation curve with reduced flux noise, achieved by using a current bias resistor of $11.86\,\mathrm{k}\Omega$. The bias field has been swept in the forward (purple) and reverse (green) directions. In the lower panel averaging has again been used in order to reduce the noise.

therefore gained stability at the expense of resolution.

Figure 7.11 shows a temperature sweep of frequency modulation curves. The temperature was controlled by a heater on the MC plate. The temperature was monitored in python using the MC thermometer to allow the current to be automatically varied to compensate for any drift in temperature.

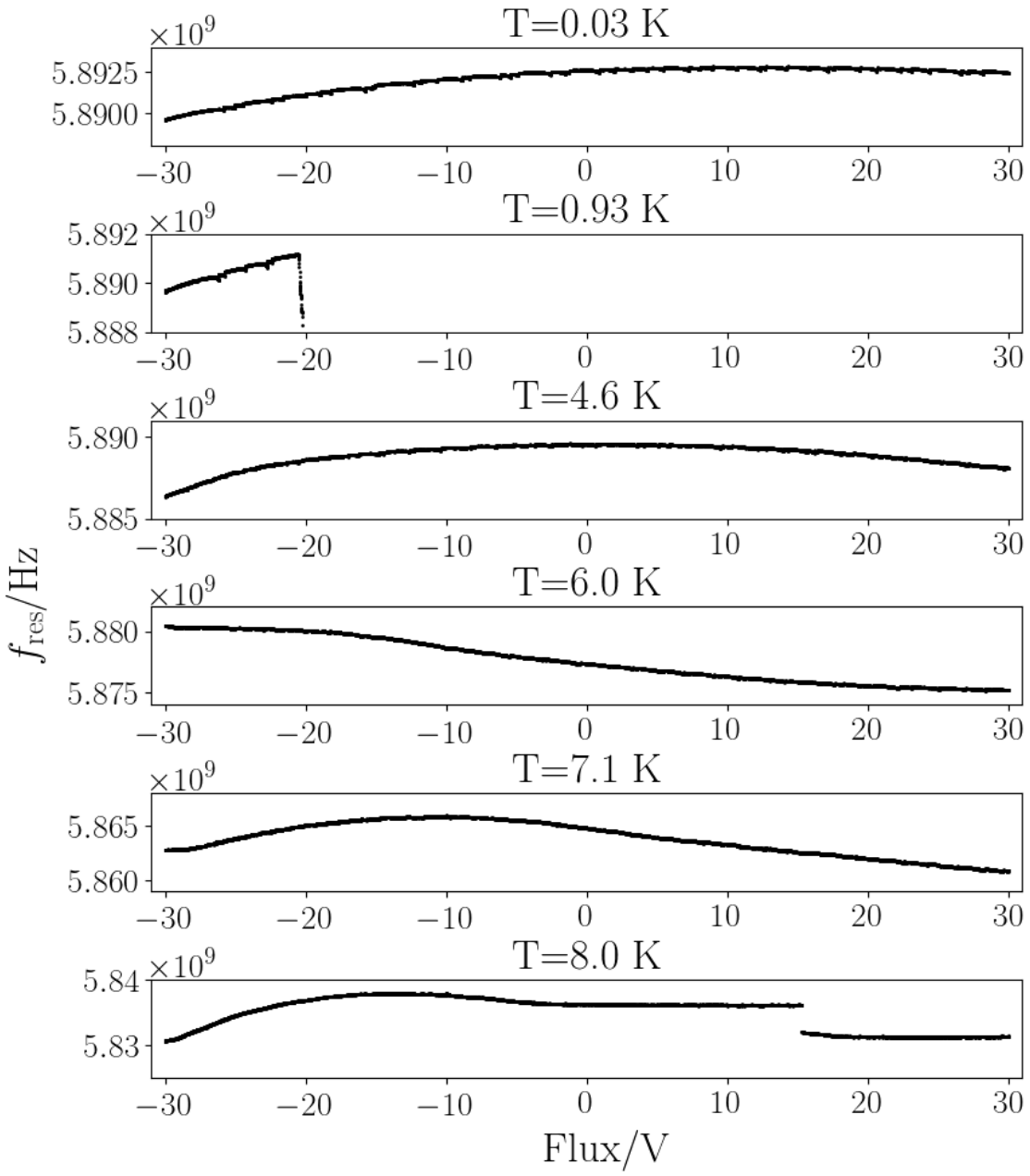

Figure 7.11: Frequency modulation curves of the sample at temperatures of $30\,\mathrm{mK}$, $840\,\mathrm{mK}$, $4.64\,\mathrm{K}$, $6.03\,\mathrm{K}$, $7.07\,\mathrm{K}$ and $8.06\,\mathrm{K}$. The sweeps were taken in the forward direction. The current limiting resistor was $1.501\,\mathrm{k\Omega}$. The right hand panel shows the temperature of each sweep. The broad features observable in this plot are due to temperature instability. The jump in frequency in the $8\,\mathrm{K}$ curve was caused by a temperature shift of $0.08\,\mathrm{K}$. The shortened range of the second panel is due to fridge warming.

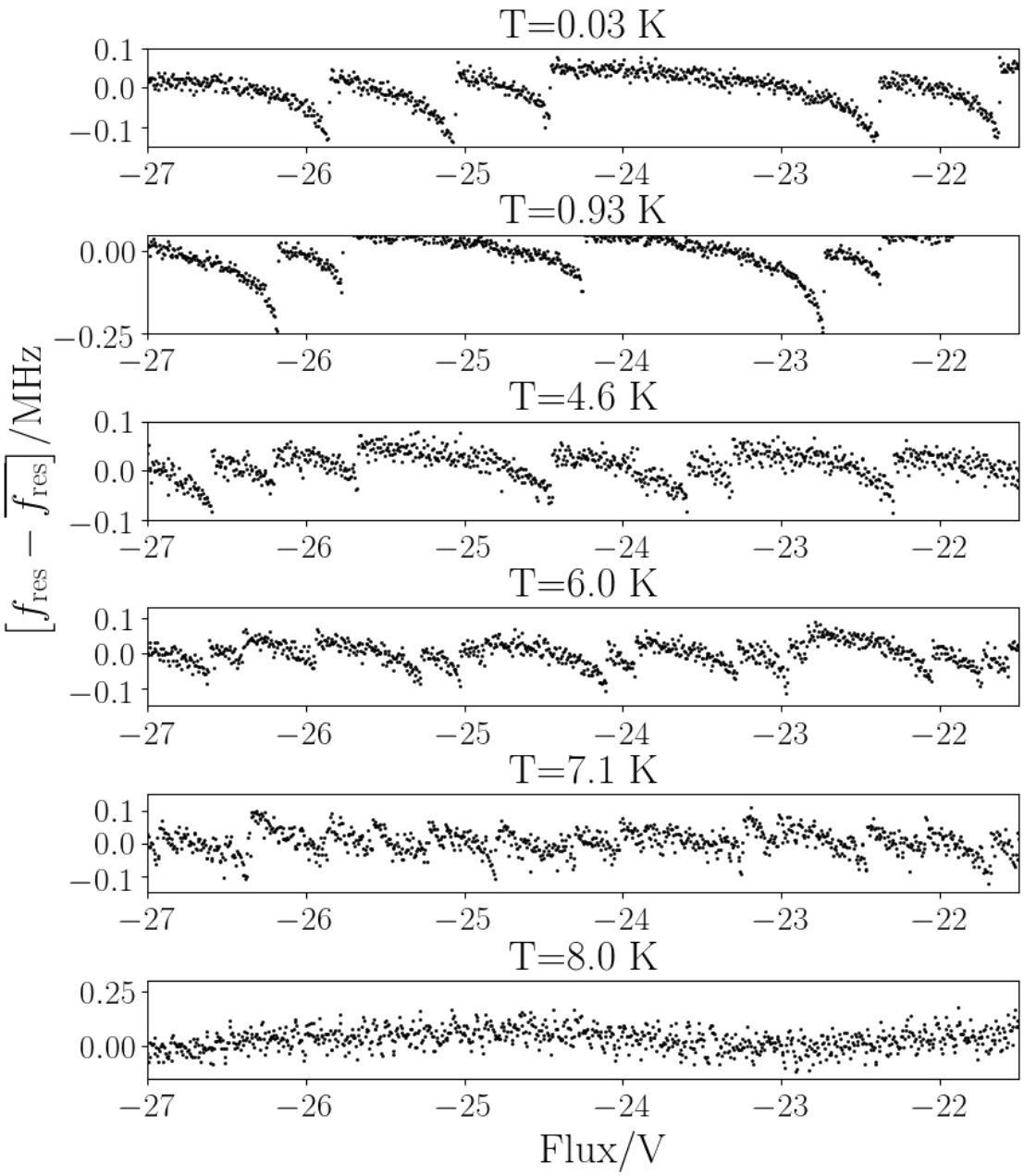

Figure 7.12: An enlargement of the frequency modulation curves of the sample shown at different temperatures between $30\,\mathrm{mK}$ and $8\,\mathrm{K}$. The background behaviour has been removed by subtracting a wide average of 500 adjacent points from the curve. The sweeps were taken in the forward direction with a current limiting resistor of $1.501\,\mathrm{k\Omega}$. The temperature is shown in the right hand panel. The increased noise in the warmer plots is due to both the lowering of Q and the increased thermal noise.

Despite this, at temperatures greater than $6\,\mathrm{K}$ there is a drift of around $0.08\,\mathrm{K}$ in temperature over time scales of a few days. At temperatures close to T_{c} this causes a significant shift in resonant frequency. This shift in resonator behaviour can be removed by performing a background subtraction. However,

the background subtraction will not account for any change in the SQUID parameters. We therefore chose to look at a small region of the curves over which the temperature was held sufficiently constant. The frequency modulation curves after the background subtraction are shown in such a small region in figure 7.12. The background subtraction is performed by the subtraction of the average of each 500 adjacent data points. The temperature was swept between $30\,\mathrm{mK}$ and $8\,\mathrm{K}$. We note that the hysteresis increases with temperature. This is evidenced by the shortening of the period of flux over which the system remains in a given state or, equivalently, the number of jumps in the window. We expect I_c to decrease with increasing temperature. This means that we expect the level of electrical hysteresis to reduce. The level of thermal hysteresis should be alleviated by the RF SQUID geometry, however increased temperature would also reduce thermal hysteresis as the re-trapping current approaches the critical current [2]. The most likely explanation for the apparent increase in hysteresis therefore is that the system energy levels are sufficiently close that thermal noise is significant enough to push the system into a different state.

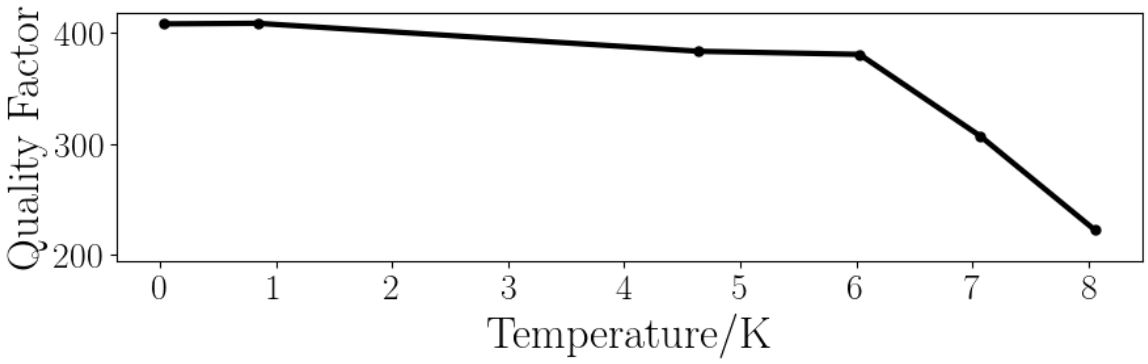

Figure 7.13: The quality factor of the resonance against the temperature. The quality factor drops significantly from $6\,\mathrm{K}$.

The increase in the system noise is in part due to the lowering of the quality factor with temperature. This is plotted in figure 7.13. The quality factor drops sharply between $6\,\mathrm{K}$ and $8\,\mathrm{K}$. At temperatures below $6\,\mathrm{K}$ the drop in Q is not significant. This means that the increased noise between the $800\,\mathrm{mK}$ sweep and the $4\,\mathrm{K}$ sweeps is mostly attributable to thermal noise. The sample is therefore optimally operated at milliKelvin temperatures.

The hysteresis at low temperature is best examined by sweeping the coil voltage in the forward and reverse directions. This is plotted in figure 7.14. The upper panel shows the frequency modulation curve

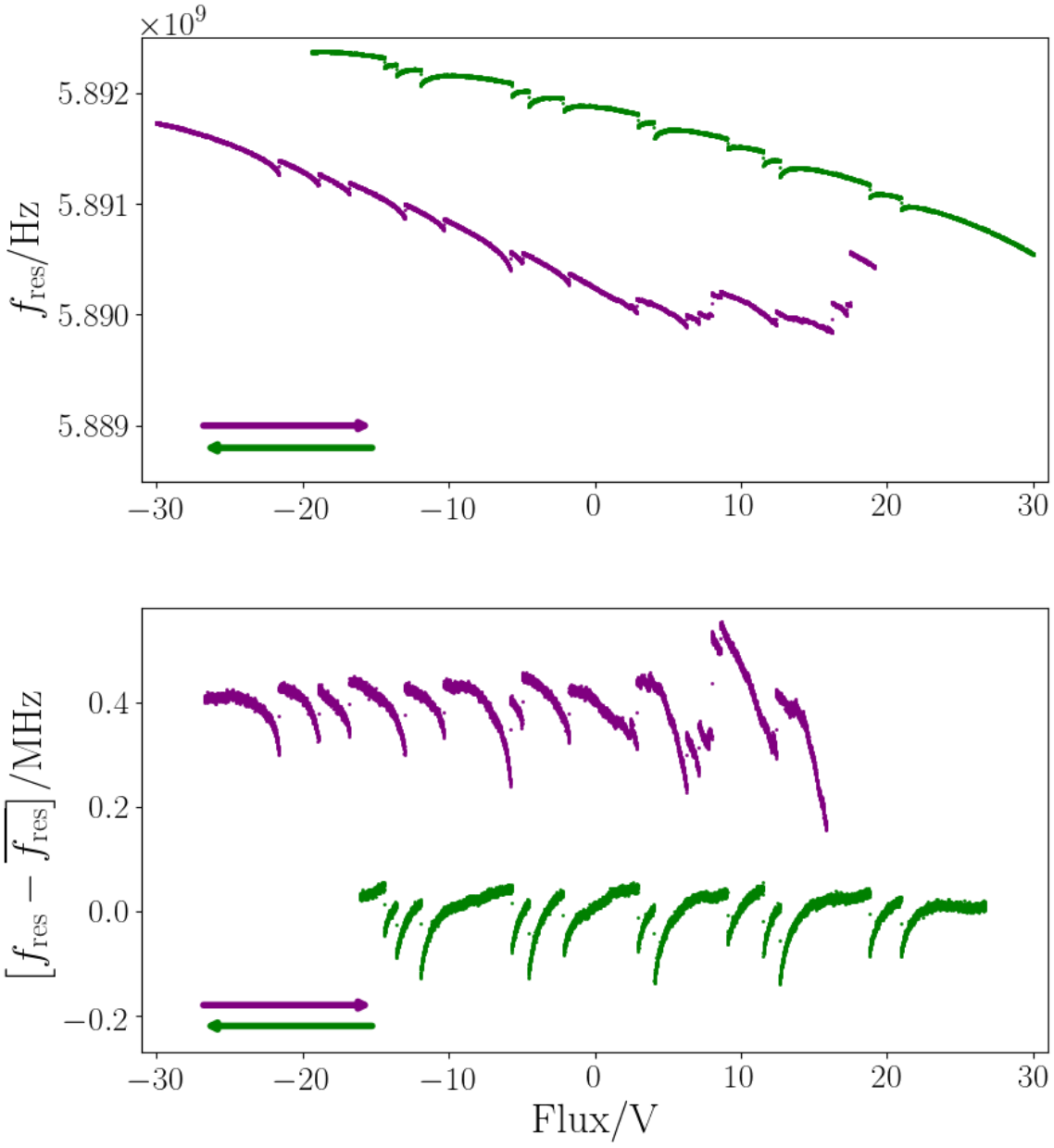

Figure 7.14: Frequency modulation curve performed at 30 mK. The voltage has been swept in the forward (purple), and reverse (green) direction. For this sweep a resistor of 3.89 kΩ has been used to limit the coil current. There is a high degree of hysteresis, the forward curve in particular jumps by a significant amount at around 20 V. The background behaviour not attributed to the SQUIDs is removed by subtracting an averaged curve in the lower panel. The curves in the lower panel are separated vertically for clarity.

in the positive (purple) and negative (green) directions. There is a significant slope, which is attributed to background behaviour. We perform a background subtraction to isolate the SQUID behaviour. This

is shown in the lower panel. We observe that the curves are highly hysteretic, making the system hard to control.

We have demonstrated the use of niobium nanobridges at a range of temperatures. The nanobridges exhibit nonlinear, highly hysteretic behaviour at all temperatures. The high degree of hysteresis is attributed to the geometry of the bridges and may be improved by using variable thickness bridges [35]. The hysteresis is likely mostly due to a hysteretic current-phase relation, since the superconducting short of an RF SQUID helps alleviate thermal hysteresis.

We have shown some evidence of coupling between SQUIDs in the form of a beating behaviour in the frequency modulation of the SQUIDs. The period of this beating is better explained by coupling than by deviation in SQUID loop area. However this could be better demonstrated in a more controllable system. The coupling will also increase the hysteresis of the system, although this is harder to quantify without fitting to the data.

Another consideration in the fabrication of nanoSQUID arrays is the localisation of the phase drop. In a Josephson junction this is well defined, however in weak links this is not always the case. In particular in the case of 2D bridges, the phase drop may spread over a scale of micrometers. If this extends over the shared side of the SQUID loops then there will also be direct bridge-bridge coupling. This may result in behaviour distinct from the SQUID-SQUID coupling behaviour previously discussed. This would further complicate the model.

7.3.2 Continuous Wave Measurements

In order to improve control of the sample we probe with a single probe tone at a constant frequency. The advantage of this method is that the input signal is well defined, as opposed to the VNA data where the frequency is continuously swept. When performing a measurement with a swept input frequency undesirable harmonics may be introduced into the signal.

The input port of the experiment was connected to an Anritsu MG3692B signal generator. The output was connected to an Anritsu MS2668C spectrum analyser. The probe tone was input at the resonant frequency of the sample. When the magnetic field is changed the resonant frequency of the sample should move. This results in a drop in the signal transmitted through the resonator. The change in amplitude of the output signal can then be mapped onto a change in resonant frequency of the sample.

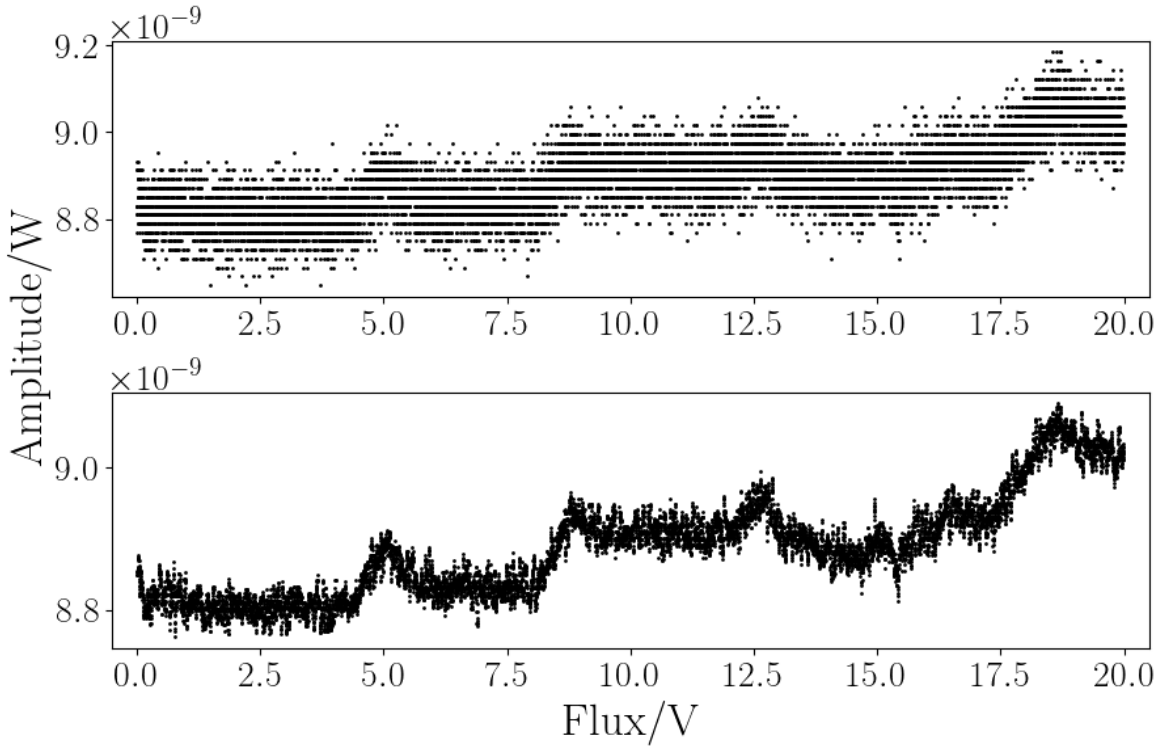

Figure 7.15: The measured amplitude of the transmitted signal as a function of applied field. The sweep was performed at $4.4\,\mathrm{K}$ in the forward direction. Top panel: Raw data. The horizontal bands are the result of the bin size of the spectrum analyser. In order to improve the signal to noise ratio a 100 point by point average has been used on the spectrum analyser. Lower panel: A 10 adjacent point average has been applied to the data. This effectively reduces the bin size.

The amplitude of the transmitted signal against the applied field is shown in figure 7.15. This sweep was performed under the same conditions as that shown in figure 7.10. The probe tone was at a frequency of $5.8904\,\mathrm{GHz}$ with a power of $-60\,\mathrm{dBm}$. In order to reduce the noise in the amplitude a point by point average with 100 iterations has been used on the spectrum analyser. The change in the amplitude of the transmitted signal is still of the order of the bin size of the spectrum analyser, as evidenced by the horizontal bands in the upper plot. We therefore apply a 10 adjacent point average to the data set, this is shown in the lower plot. There appears to be some structure in the measured signal.

The effect, however does not appear to be repeatable. Figure 7.16 shows a repetition of the measurement of the amplitude of the transmitted signal through the sample as a function of the applied flux. The curves are not similar and do not resemble the results of the VNA measurement shown in figure 7.10. This means the effect is likely purely the result of system noise. To study this we perform a sweep under the same conditions, but set the voltage source to only zero values. This is shown in figure

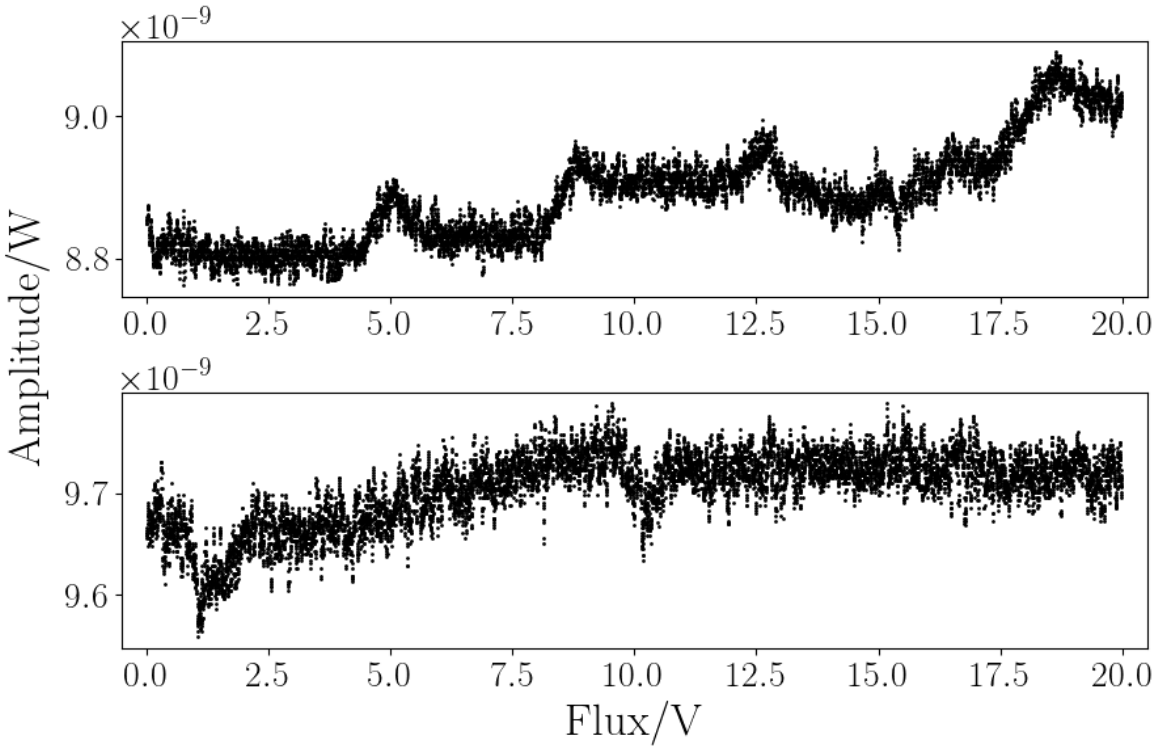

Figure 7.16: Repeatability of the measured amplitude of the transmitted signal as a function of applied field. The sweeps shown in the top and bottom panels were performed under the same conditions. A 10 adjacent point average has been applied to the data to reduce the bin size of the spectrum analyser.

7.17. The fluctuation in the curve is similar to that observed when the field is changed. This means that the fluctuations are likely not related to the sample.

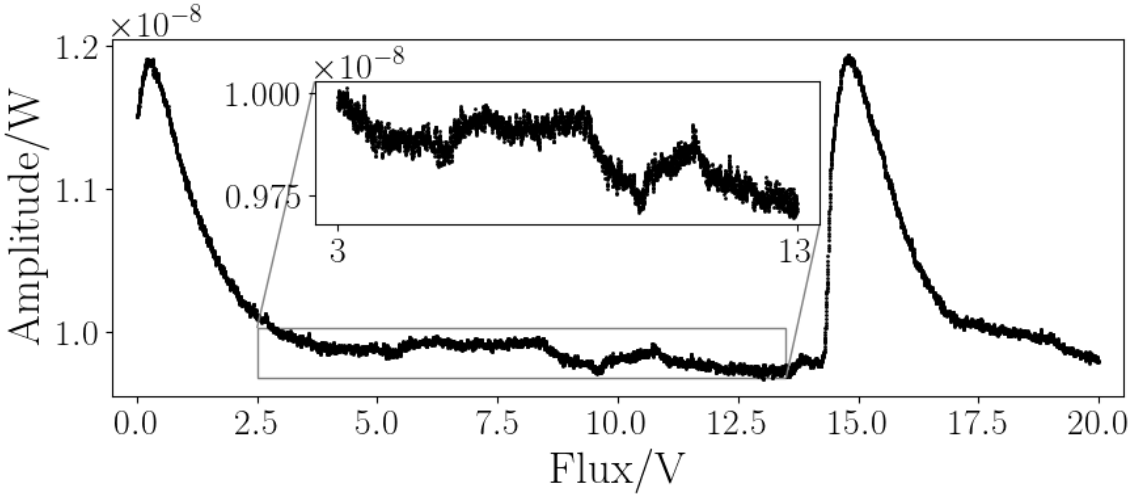

Figure 7.17: Control measurement of the amplitude of the transmitted signal. The voltage source only outputs zero volt values. Other than the current the system is identical to the previous sweeps. We note that the system has a similar level of fluctuation as shown when the field is changed. This means that the effect is likely not due to the sample. The large spikes are the result of temperature fluctuation following helium transfers. For consistency, this has also had a 10 point floating average applied.

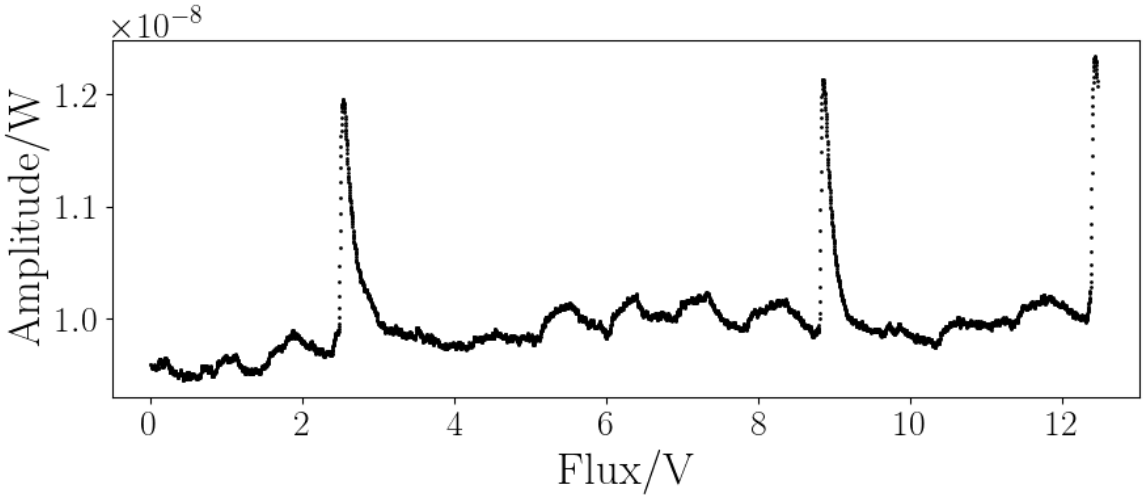

Figure 7.18: The amplitude of the transmitted signal. The point by point averaging has been increased by a factor of 10, to 1000 in order to improve the signal to noise ratio. The large peaks are the result of temperature instability during helium transfers. The behaviour observed still does not appear to be the result of the sample.

It is possible to improve the noise resolution of the spectrum analyser by increasing the number of

point by point averages employed in the data collection. In figure 7.18 the point by point averaging has been increased to 1000. This has reduced the noise, but is not sufficient to expose features related to the sample behaviour.

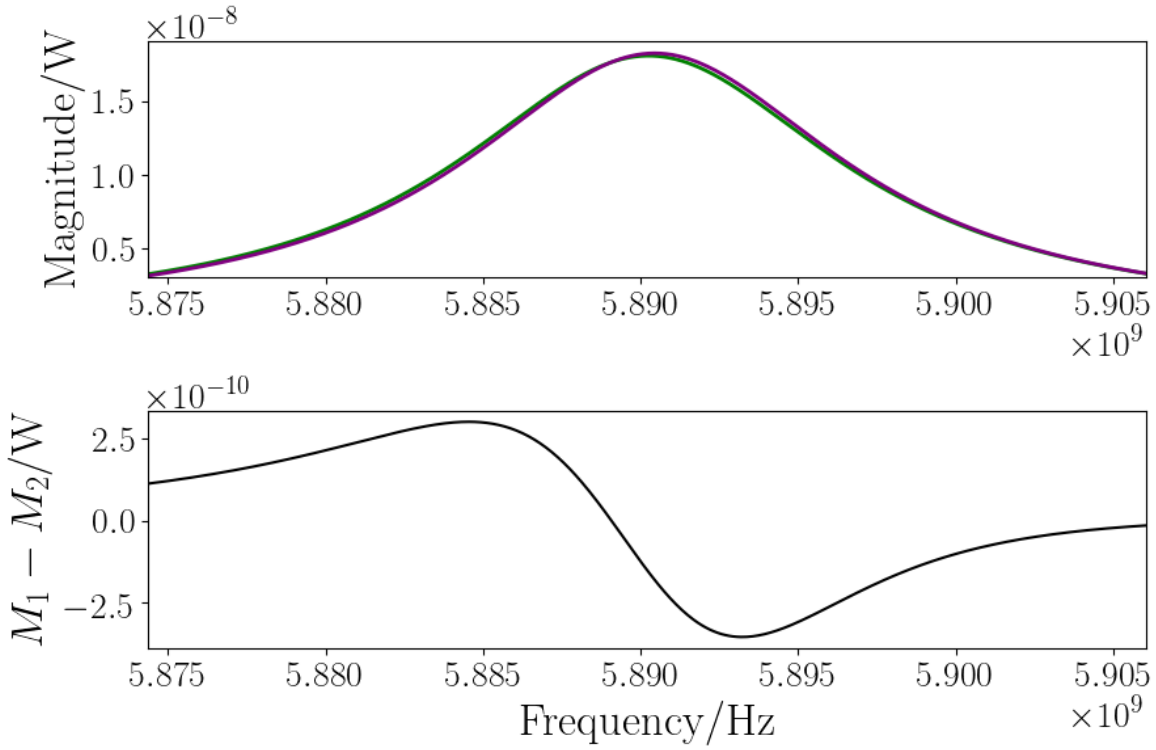

Figure 7.19: A comparison of 2 resonant modes. The modes are chosen at positions in coil voltage where the displacement between them is maximised. The modes have been fitted with a Fano function. Top panel: the fitted Fano resonance. The data is omitted to allow the difference between the fits to be more clearly observed. Lower panel: The difference between the amplitudes of the modes as a function of applied field.

We can compare this to the difference in amplitude expected from the VNA measurements. We choose 2 maximally displaced modes and compare the amplitude at different points. A Fano fit to the modes is shown in the top panel of figure 7.19. The lower panel shows the difference in the magnitudes of the resonance at each frequency. The data used for this analysis is from figure 7.10, which was performed under the same conditions as the continuous wave measurements. The difference in amplitude at the input frequency of $5.8904\,\mathrm{GHz}$ is $1.86 \times 10^{-10}\,\mathrm{W}$. This is of the order of the noise after averaging and is smaller than the fluctuations observed when the coil current was held constant.

It is possible to improve this experiment by moving the probe tone to the position of maximum gradient rather than maximum amplitude. Since the resonance has a high degree of symmetry the

direction of the resonant frequency shift is not ascertainable when the probe tone is input at the resonant frequency. Moving to the frequency where the gradient of the resonance is maximised would help remove this symmetry. From figure 7.19 we are able to determine the maximum difference. This is equal to $3.65 \times 10^{-10}\,\mathrm{W}$ at a frequency of $5.893\,\mathrm{GHz}$. This is a factor 2 improvement in sensitivity which, although appreciable, does not significantly move the signal from the noise level. We, therefore, did not repeat the experiment.

In this regime we are also sensitive to fluctuations in resonant frequency resulting from the temperature drift over time. This is not significant, but would impact the relatively precise tuning of the probe tone needed to produce sufficient sensitivity. For these reasons it was decided not to continue probing the transmitted amplitude of a constant frequency wave.

7.4 Comparison of Experiment and Theory

Figure 7.20 compares the expected frequency modulation curves for arrays of coupled and uncoupled SQUIDs to an array where the loop areas of the SQUIDs are not identical. The dimensionless inductance is high, in order to make the system hysteretic. The current phase relation of the weak links in the array has been assumed to obey the KO-1 relation. We would not expect this to be the case given the geometry of the bridges, however, the model should still be indicative of the array behaviour. The difference in loop areas of 2.5% between each SQUID is slightly larger than the deviation of the loop areas in the measured array. The coupling of $\alpha = 0.3$ is the expected coupling constant of the measured array. The chosen value of $\beta_{\mathrm{L}} = 2$ gives a large amount of hysteresis, whilst not being too large to destabilise the numerical solution algorithm. A distinction between these cases must be made in order to determine whether the measured sample behaviour is best explained by coupling or by loop area deviation alone. By inspection the behaviour does indeed seem to correspond most closely to the coupled array case.

Figure 7.21 shows a comparison of the experimentally observed frequency modulation curve and the curve modelled assuming a nearest neighbour interaction. The current phase relationship is assumed to follow the KO-1 theory. This accounts for some of the discrepancy between model and measurement. Both curves exhibit beating effects. The periodicity of the beating effect in the measured curve is hard to quantify due to noise and the varying background behaviour. However it appears to have a greater

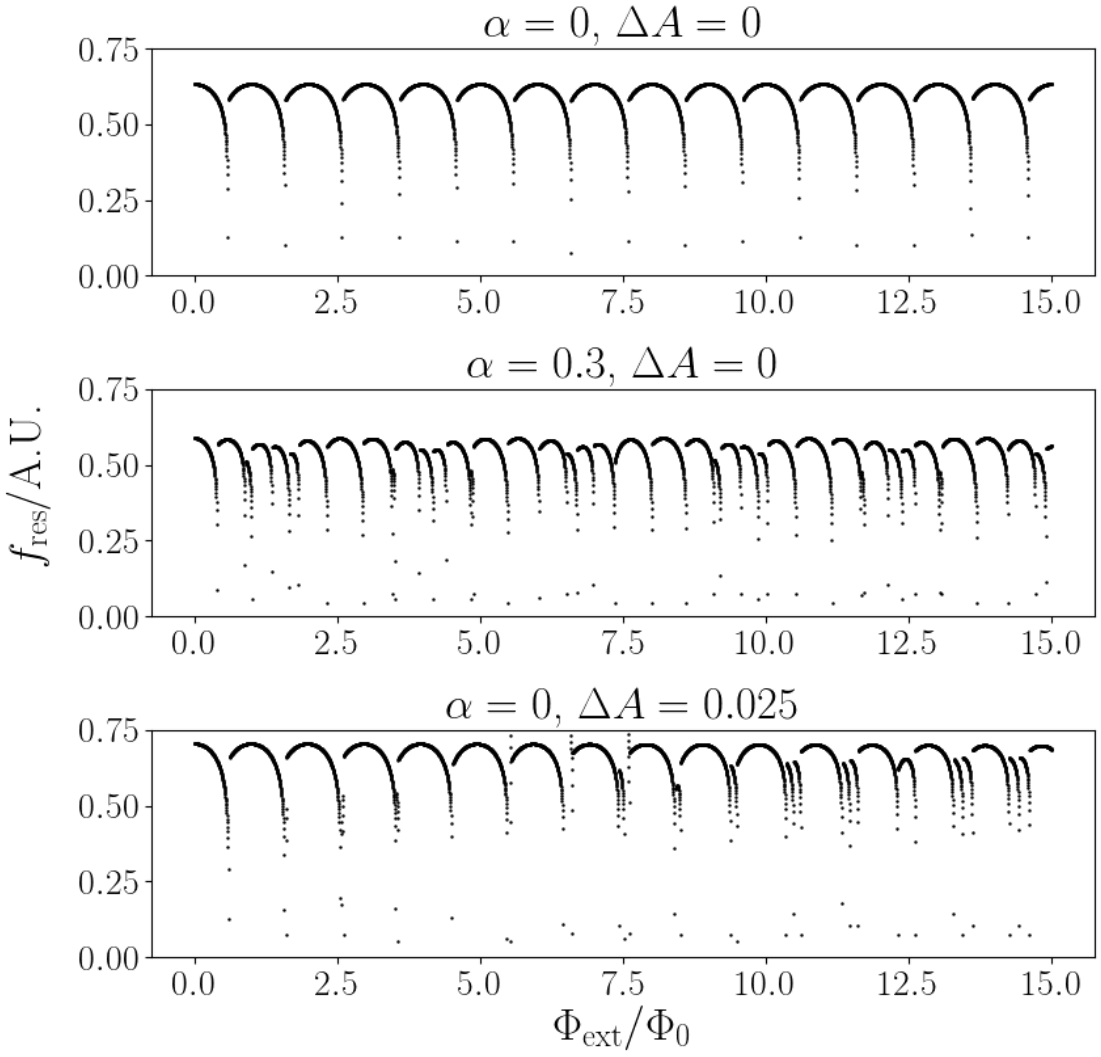

Figure 7.20: Modelled frequency modulation curves in the case of an uncoupled array of identical SQUIDs (top), an array of coupled identical SQUIDs (middle) and an array of uncoupled SQUIDs with differing loop areas. The difference in loop areas is 1.25% between each SQUID, resulting in a total 2.5% deviation across the array. The coupling in the coupled array is $\alpha = 0.3$.

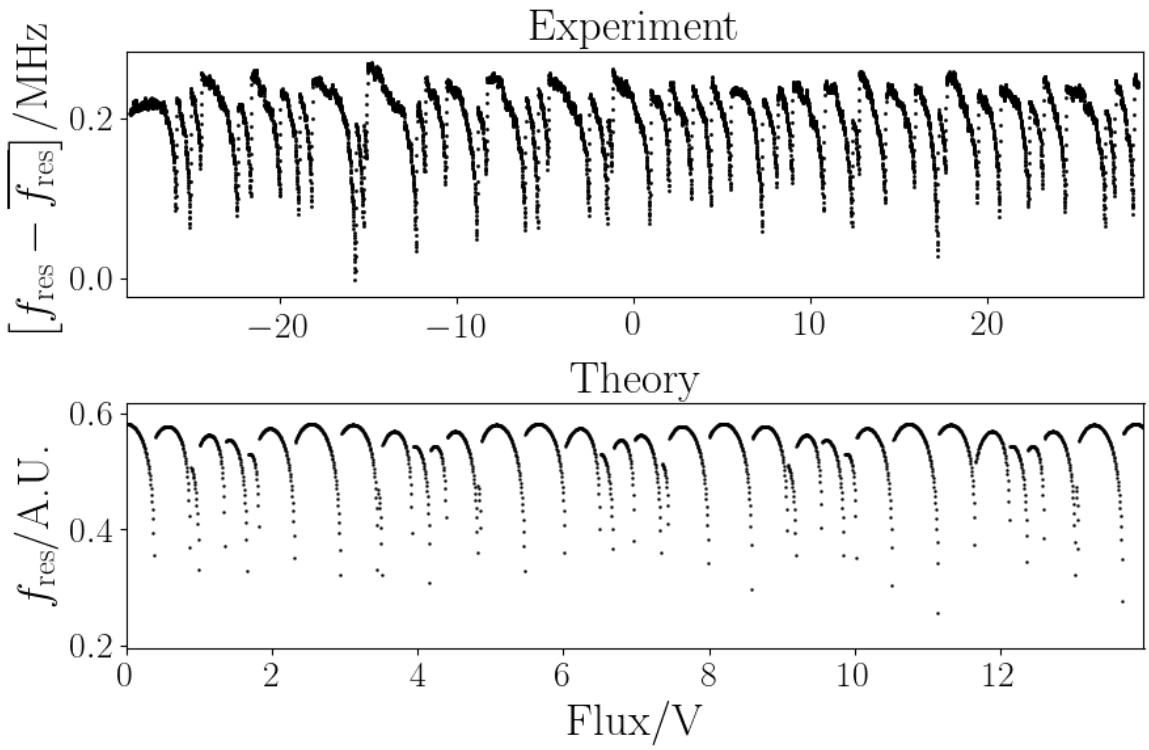

Figure 7.21: Comparison of the measured frequency modulation curve at $30\,\mathrm{mK}$ to the model assuming a nearest neighbour coupling of $\alpha = 0.3$. The current phase relation of the nanobridge is taken to be given by the KO-1 theory. In reality this is not expected to be the case. This accounts for the difference in the shape of the modulation fringes.

period than the modelled curve. The increased period may be because of an additional contribution from loop area deviation or due to an overestimation of the coupling parameter.

7.5 The Current Phase Relationship

The modelling is further complicated since we do not have precise knowledge of the current phase relation of the nanobridge.

We may try to find the current phase relation from our measurements, however, it is not obvious how to deconvolve the inductive contributions from each SQUID. As discussed in section 4, the resonant frequency of an array of SQUIDs is given by

$$f_{\mathrm{res}} = f_0 \left[1 + \sum_{i=1}^{N} \frac{a^{(i)}}{1 + \beta_{\mathrm{L}}^{(i)} \cos(\phi_{\mathrm{int}}^{(i)}) - \alpha \frac{\partial}{\partial \phi_{\mathrm{int}}^{(i)}} \left[(1 - \delta_{i,1})\, \phi_{\mathrm{int}}^{(i-1)} + (1 - \delta_{i,N})\, \phi_{\mathrm{int}}^{(i+1)} \right]} \right]^{-1/2} . \quad (7.2)$$

Equation 7.2 may be generalised to describe systems with non-sinusoidal current phase relationships by substituting the general current phase relation, $I(\phi)$ for the sinusoidal term to find,

$$f_{\text{res}} = f_0 \left[1 + \sum_{i=1}^{N} \frac{a^{(i)}}{1 + \frac{2\pi L_{\text{g}}}{\Phi_0} I'\left(\phi_{\text{int}}^{(i)}\right) - \alpha \frac{\partial}{\partial \phi_{\text{int}}^{(i)}} \left[(1-\delta_{i,1})\,\phi_{\text{int}}^{(i-1)} + (1-\delta_{i,N})\,\phi_{\text{int}}^{(i+1)} \right]} \right]^{-1/2}, \tag{7.3}$$

where $I'\left(\phi_{\text{int}}^{(i)}\right)$ is the derivative of the current phase relation for the i^{th} nanobridge. Rearranging gives,

$$\left(\frac{f_0}{f_{\text{res}}}\right)^2 - 1 = \sum_{i=1}^{N} \frac{a^{(i)}}{1 + \frac{2\pi L_{\text{g}}}{\Phi_0} I'(\phi_{\text{int}}^{(i)} - \alpha \frac{\partial}{\partial \phi_{\text{int}}^{(i)}} \left[(1-\delta_{i,1})\,\phi_{\text{int}}^{(i-1)} + (1-\delta_{i,N})\,\phi_{\text{int}}^{(i+1)} \right]}, \tag{7.4}$$

from which we can not simply separate the contribution of each SQUID to find $I\left(\phi_{\text{int}}^{(i)}\right)$.

In the weak coupling limit at low field we can make the approximation $\phi_{\text{int}}^{(i)} \approx \phi_{\text{int}}^{(i+1)}$. In this case we may rearrange equation 7.4 to find,

$$\frac{\Phi_0}{2\pi L_{\text{g}}} \left(\frac{3a f_{\text{res}}^2}{f_0^2 - f_{\text{res}}^2} - 4\alpha - 1 \right) = I'\left(\phi_{\text{int}}\right). \tag{7.5}$$

The superscript (i) has been dropped because the SQUIDs are assumed to be identical under the weak coupling and low field limits. The derivative here is with respect to ϕ_{int}. The integration therefore requires the solution of the transcendental equation. Since we do not know $I(\phi_{\text{int}})$ this is not tractable.

The term f_0 is expected to be constant. Our measurements, however, have shown varying background behaviour. This corresponds with the replacement of f_0 with an unknown function.

The gradient of the current phase relation is plotted in the lower panel of figure 7.22. In calculating this relation it has been assumed that the coupling and field are sufficiently low that the SQUIDs are identical. With a coupling strength of 0.3, this assumption is only valid at very low field.

That the nanobridge current phase relationship tends to linearity is illustrated by the low modulation depth. The modulation depth of an RF SQUID is dependent on the product of the geometric loop inductance and the gradient of the current phase relation. The loop geometry was sufficient to exhibit a modulation depth several orders of magnitude larger than that observed. A low gradient of the current phase relation agrees with the modelling of long 2D bridges by Vijay et al [37], who predict a hysteretic and approximately linear current phase relation.

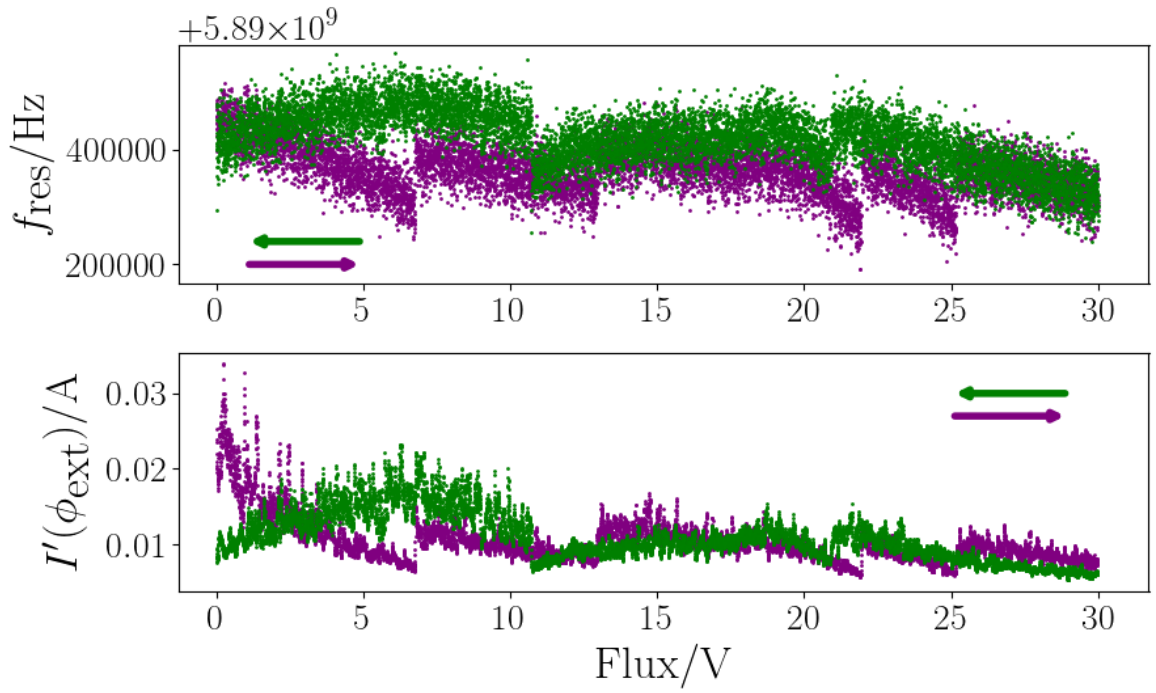

Figure 7.22: The gradient of the current phase relation for the RF SQUIDs. The SQUIDs are assumed to be identical. This assumption is only valid at very low applied field. The top panel shows the frequency modulation data used to calculate this curve.

7.6 Conclusion

We have measured modulation of the resonant frequency of a CPW resonator containing an array of 3 RF SQUIDs. The signal to noise ratio of the system was low, however averaging and background subtraction allowed us to obtain an observable signal.

The signal to noise ratio is low because of the use of nanobridges. For the geometry of nanobridge used we expect a relatively linear current phase relation [35]. The modulation depth is related to the derivative of the current phase relationship. Therefore this low nonlinearity is likely to be the cause of the low signal to noise ratio.

The modulation depth can be compared to that shown in figure 2.4, which has been calculated for a sample with the same SQUID and resonator geometries, but with Josephson junctions replacing the nanobridges.

Despite the difficulties arising from the small signal the measured behaviour resembles that predicted by the coupled SQUID model. The frequency ratio and the heights of the peaks on the FFT of the data also support the theory.

Chapter 8

Discussion

Measurements performed on a CPW resonator containing 2 arrays of 32 RF SQUIDs revealed some unexpected features in the frequency modulation curve. The measurements themselves predate the work in this thesis. The unexpected features observed were hysteretic jumps and a beating pattern. The effects were repeatable.

The features can not be well explained by either an inhomogeneous applied field or by large β_{L}. Large β_{L} would result in hysteretic jumps occurring at half flux values. In the experiment the jumps were observed at all values of applied flux. We have studied the inhomogeneity of the applied field in a separate experiment and found that the inhomogeneity is not significant enough to explain the beating effect.

In this thesis we show that both the jumps and the beating effect instead arise as a consequence of a coupling between nearest neighbours in the array. The parameters used in the model were calculated from the geometry of the measured sample. The model and the experiment are in good qualitative agreement. The measurements and the model are shown in figures 2.11 and 4.6 respectively.

The origin of the coupling is believed to be a shared phase drop along the shared side. The features arise due to disorder in the flux configuration of the array which is the result of an edge effect. The hysteretic effects caused by the coupling are to the detriment of the nonlinearity.

The experiment was originally performed on a resonator containing 64 SQUIDs. Due to the complexity of the system, a precise fit to the data was not possible. Therefore a further experiment was performed on a resonator containing only 3 SQUIDs. In the new sample the Josephson junctions had been replaced by nanobridges. Again a precise fit was not possible, however reasonable qualitative

agreement between the model and the measurement was observed. A comparison of the measurement to the model is shown in figure 7.21.

In nanobridge SQUID array the nanobridges exhibited a high degree of hysteresis in the current phase relation. This inhibited complete control of the SQUID state. The relative linearity of the current phase relation of the nanobridges in comparison to that of Josephson junctions has meant that the modulation depth of the array was low. Therefore it has been necessary to employ averaging to improve the signal to noise ratio.

The current phase relationship of the nanobridges is not as well defined as that of a Josephson junction; the function is sensitive to the geometry of the bridge. Along with the significant hysteresis this has prevented a fit of the model to the new data. In modelling the nanobridge SQUIDs it has been assumed that nanobridges are well described by the KO-1 theory. It is expected that using a more accurate form of the current phase relationship would improve the agreement between measurement and theory.

It is possible to examine the beating effect more closely. Comparing the measured beat period with that predicted by the coupled SQUID model shows good agreement. The agreement between the measured beat period and the period predicted by loop area deviation shows poor agreement. This further supports the model. To improve this it is necessary to perform measurements over a greater number of flux quanta with a greater degree of control than was achieved. The control was limited by hysteresis in the current phase characteristics.

In order to further our understanding of the system, further measurements of short arrays of RF SQUIDs with Josephson junctions should be taken. The choice of Josephson junctions should reduce the hysteresis and increase the modulation depth. This should result in a more controllable system. It is necessary to perform further measurements on the DC characteristics of the nanobridges in order to obtain the current phase relation. However these measurements will be subject to thermal hysteresis. In an RF SQUID the inductive short provides a conduction path that protects the bridge from thermal hysteresis. Therefore DC measurements may not truly represent the current phase relation of the bridge when embedded in a SQUID loop. The lack of thermal hysteresis is illustrated by the retention of a Lorentzian line-shape at all applied fields. The lack of an observed volcano nonlinearity means that the circulating current in the SQUID loop does not cause energy dissipation in the nanobridge.

We have shown that SQUID arrays are sensitive to deviation in loop area. The phase difference

caused by such a deviation creates a region of increased disorder centred on the deviation. We have proposed a method for the removal of the edge effect by introducing shunt inductors into the SQUID loops.

A further effect that has not been considered is that the linear form of the coupling assumed here may form only the first term in an expansion. In stronger coupling the effect may not preserve this linearity. It is possible that in the strong coupling regime it may be energetically favourable for the array to switch into a configuration with zero current along the shared branches [70]. This would result, effectively, in a change in the number of SQUIDs in the array. In this switching regime we would indeed expect to observe jumps. Further modelling should be performed to understand how such a system would behave.

A model assuming a nearest neighbour coupling shows good qualitative agreement with the initial experiment performed on arrays of 32 SQUIDs with reasonable parameters. The model is able to reproduce both the observed jumps and the observed beating effect. The agreement with the experiment performed on short arrays of nanoSQUIDs is weaker. However the model resembles the data more closely than other models which neglect the coupling. The period of the beating effect predicted by the model of coupled SQUIDs matches closely to that observed in the experiment. Both the experiment performed previous to this work and the experiment described in this thesis support the model.

The reduced agreement to the theory of the sample containing nanobridge SQUIDs may be due to the substitution of Josephson junctions for nanobridges, which lead to poor control. Another possibility is that the increased coupling strength means that the assumption of linearity is no longer valid.

A repetition of the experiment with a greater level of control over the sample is expected to provide further insight into the model. This may then allow for more precise analysis of arrays of nonlinear elements. In turn, this allows for optimisation of the design and performance of such devices.

Appendix A

Python Instrument Control Manual

The python instrument control programs contain a list of drivers for various instruments. It is an ongoing project and should be constantly developed as new applications are needed. It was developed in Python 2.7.

The driver should be imported into a measurement script. An instance of the class should be made and then the functions can be called to issue commands. The drivers use a PyVISA backend.

There are different levels of programs. Level 1 programs consist of a list of function definitions. To ensure back compatibility these should not be altered (although new functions can be added). Level 2 drivers contain some commonly used combinations of functions, for instance those needed to set up, trigger and save data from a VNA sweep. To ensure back compatibility these should also not be altered. These are not necessary to use the programs, but make life easier. Level 3 programs are where the measurement is performed. The drivers should be imported and functions called as necessary.

I have tried to use the format 'filename' for the filename, 'ClassName' for the class name and 'functionName' for the functions. There are some deviations from this, which are hard to retrospectively amend.

This document will not contain an exhaustive list of all the functions. The drivers themselves can be inspected to find the complete function list.

In the case of multiple identical instruments the GPIB address of the desired instrument needs to be specified.

A.1 List of Functions

These will follow the format

filename

ClassName(inputs)

functionName(inputs)

Description

Not all files contain classes. Inputs enclosed in ” must be entered as a string.

A.1.1 Ancillary Scripts

Path: T:\Instrument Control\Instruments\drivepy-master\Programs\Jacob

These are some additional scripts for use alongside the drivers.

VNAGUI

A front panel for the VNA for remote use. Open the script and run it. It has only basic functionality.

directory

Adds the driver folder to the current working directory. This needs to be copied to your current working directory. It should be the first import file in a measurement script.

A.1.2 Level 1

Path: T:\Instrument Control\Instruments\drivepy-master\Drivers

Level 1 drivers import pyVISA. They are self contained and are not used directly.

AnalogueInput

analogueInput(channel number, sample rate, number of samples)

Interface with PXI. I have not used this extensively, so have not developed the program fully. The program is able to take data, but the format or structure of the program may be improved.

Get_Data

Get(channel, collection time [s], device address)

Interface with the analogue input DAQ. This could also benefit from some development. The program works but has not been extensively used.

signalgenerator

SignalGenerator(Address='GPIB0::2'/'GPIB0::5')

constantWave(f)

Sets the generator to constant wave mode at a frequency of f GHz.

sweep(f1, f2)

Sweeps from f1 to f2 in GHz.

output('on'/'off')

Turns output on or off.

power(P)

Sets the power level in dB.

spectrumanalyzer

SpectrumAnalyzer()

setSpan(f, unit)

Sets span width. Units are optional. The default is GHz.

setCenter(f, unit)

Sets centre frequency. Units are optional. The default is GHz.

setStartFreq(f, unit)

Instead of specifying centre and span it is possible to specify start and stop. Units are optional. The default is GHz.

setStopFreq(f, unit)

Sets stop frequency. Units are optional. The default is GHz.

setAttenuation(True/False, A)

Turns attenuation on or off. A is optional, and defaults to 10dB.

setAverages(n)

Sets the number of averages.

average('on'/'off')

Turns averaging on or off.

universalcounter

Controls the universal counter instrument. Each class performs a different type of measurement which can be set up by calling functions within the class. I have not used this driver extensively and am unhappy with the format. It should be developed further.

UniversalCounter()

Totalize()

Frequency()

vna

The VNA calibrates. If a command is sent whilst the instrument is calibrating it will return a timeout error. Commands should therefore be sent in the form:

```
while i==0:
    try:
        VNA.command()
        i=1
    except:
        time.sleep(5)
```

VNA()

setAttenuation(A)

Sets port 1 attenuation in dB.

setAttenuation2(A)

Sets port 2 attenuation in dB.

setPower(P)

Sets power in dB.

setStartFrequency(f)

Sets start frequency in GHz.

setStopFrequency(f)

Sets stop frequency in GHz.

setCenterFrequency(f)

Sets centre frequency in GHz. Alternative to start and stop.

setSpanFrequency(f)

Sets span frequency in GHz. Alternative to start and stop.

setAveraging('on'/'off')

Turns point by point averaging on or off.

setNumberOfAveraging(n)

Sets the number of averages.

setVideoBW(f)

Slows or speeds the trace at the expense of noise. Options are 10, 100 or 1000.

getTrace()

Depending on the type of measurement performed, returns either frequency, magnitude, attenuation1, power or frequency, magnitude, phase, attenuation1, power as lists.

wavegenerator

WaveGenerator(address='GPIB0::9'/'GPIB0::10')

setPower(p)

Sets output voltage (not power).

setUnit('VRMS'/'VPP'/'DBM')

Sets unit of p.

setFreq(f)

Sets wave frequency in Hz.

output('on'/'off')

Turns output on or off.

func('SIN'/'SQU'/'PULS'/'RAMP'/'NOIS'/'DC'/'USER')

Set the specified wavefunction.

offset(v)

Add an offset to the wavefunction.

arbitraryWave(l)

Defines the USER wave function. l is a list of data points between -1 and +1.

yokogawa7651

Yokogawa7651(address='GPIB0::7'/'GPIB0::11')

setVoltage(v)

Sets the voltage to the correct range for the specified voltage then sets the voltage in volts.

output('on'/'off'/0/1)

Turns the output on or off.

A.1.3 Level 2

Path: T:\Instrument Control\Instruments\drivepy-master\Programs\Jacob

Level 2 programs have level 1 programs as an import. They are intended to be used as drivers to standardise some commonly used functions and to help reduce repetition in the code.

savescript

SaveScript forces data to be saved in the same format. As well as being convenient programatically, this is useful for future analysis. It is straightforward to write scripts to deal with a standardised data format. All lines except those containing the data set start with '#'. Each parameter is clearly specified, and is therefore easily searchable by an analysis script in python.

SaveScript('path', 'filename')

VNA(attenuation, power, frequency, magnitude, phase)

Appends VNA data to the file specified in the class instance. Phase is an optional parameter. Frequency and magnitude are lists.

Yokogawa(voltage, 'Coil'/'MC')

Appends the Yokogawa voltage to the specified file. 'Coil'/'MC' is an optional text input to describe what the Yokogawa is connected to. Options are not limited to 'Coil' or 'MC'.

Thermometry('SQUIDs'/'MC'/'both')

Appends thermometry information to the specified file.

SG(f,p)

Appends the signal generator information to file. f is frequency, p is power.

SA(f,p)

Appends spectrum analyser data to the file. f is a list of frequencies, p is a list of powers.

Now()

Appends timestamp to the file.

Text('text')

Appends any additional text to the file.

vnasweep

sweep('path', 'filename', f_start, f_stop, power, attenuation1, attenuation2)

Performs a VNA sweep then saves the data to the specified file. attenuation1 and attenuation2 are optional and default to 0dB.

temperaturecontrol

ReadThemometry()

Reads and returns the MC thermometer.

TemperatureControl(T_low, T_high, v)

Puts a voltage across the MC heater using the Yokogawa to heat the fridge. T_low is the lowest acceptable temperature and T_high is the highest. The function performs an

algorithm to find the voltage that will keep the MC at a constant temperature somewhere in the specified window. The parameter v is optional. It defaults to 2V. It determines a low level voltage that the algorithm will fall to. The algorithm will search between this value and the maximum voltage of the Yokogawa, so it is important that v is not set too high. Setting v too low will result in the algorithm running a little slow. The algorithm looks at the current temperature and the temperature gradient and adjusts the voltage accordingly. In general it works well.

TemperatureLimit(T_low, T_high, v)

Turns the Yokogawa on or off to keep it in the specified temperature window. It is best used as a high limit in the vicinity of T_c. The parameter v is optional. It defaults to 8V. It is the Yokogawa voltage.

TransferDetect(T)

This function is as yet untested and so may need some tweaking. T is the pre-measurement temperature. It reads a new temperature and looks for a significant deviation, indicating a transfer. If there is a significant system, it checks periodically until the temperature has stabilised. It then restarts the measurement.

sourceanalyzersweep

sweep('path', 'filename', f_start, f_stop, n_steps, power, averaging, span)

Performs a VNA like sweep with the signal generator and the spectrum analyser. Averaging and span are optional parameters.

A.1.4 Level 3

Level 3 programs are the programs that call level 1 and 2 programs. These are the programs that should be edited to perform the desired measurement. In this section I will give an example program to set a coil voltage, trigger a VNA sweep and save the data:

```
import time
import numpy as np
#Point the program to the drivers
```

```
import directory
#First level import
import vna
import yokogawa7651
#Second level import
import vnasweep
import savescript
#Create classes
vna=vna.VNA()
yoko=yokogawa7651.Yokogawa7651('GPIB0::11')
#Ensure we take all data
np.set_printoptions(threshold=np.nan)
#Use a loop to catch timeout errors due to calibration
i=0
while i==0:
    try:
        vna.setNumberOfAveraging(100)
        vna.setAveraging('on')
        i=1
    except:
        time.sleep(3)
        print 'VNA error. Calibrating'
#Set the coil voltage
yoko.setVoltage(5)
yoko.output('on')
path='G:\Example Folder'
filename='VNAtrace' + '.txt'
#Create save file
SS=savescript.SaveScript(path, filename)
```

```
#Save text to file
SS.Text('Experimental␣Description')
#Save coil voltage to file
SS.Yokogawa(v, coil_or_mc='Coil')
#Save thermometry data
SS.Thermometry(which='mc')
#Take and save VNA sweep from 5GHz to 6GHz with power -10dB and
#attenuations of 0dB
vnasweep.sweep(path, filename, 5, 6, -10, 0, 0)
yoko.output('off')
```

Appendix B

Python Code for Numerical Modelling

Here we give the code used to numerically solve the transcendental equation for a sample containing multiple arrays of SQUIDs. This class can be called to obtain the magnetic moments of the SQUIDs in the array, the internal fluxes or the resonant frequency of the whole array.

```
#Class structure. Calculates moment, resonant frequency and
#internal flux.
from scipy.optimize import fsolve
from scipy.optimize import broyden1
import numpy as np
import random
from sys import stdout
class IntFlux(object):
    def __init__(self, beta, a, n, narray, mini, maxi, nsteps,
                 dfieldsquid=0, dfieldarray=0, errorcheck=5e-6,
                 phienoise=0, impurities='off',nimpurities=2,
                 impuritymagnitude=0.01, betadeviation=0.0,
                 betaarray='off', edgeInductor=1., sweep='both',
                 Lr=1, junctiontype='jj'):
        self._beta=beta
        self._a=a
```

```
        self._n=n
        self._narray=narray
        self._dfieldsquid=dfieldsquid
        self._dfieldarray=dfieldarray
        self._mini=mini
        self._maxi=maxi
        self._nsteps=nsteps
        self._edgeInductor=edgeInductor
        self._Lr=Lr
        self._junctiontype=junctiontype
        self._phienoise=phienoise

        shift=[]
        for i in range(narray):
            for s in range(n):
                shift.append(1+(s*dfieldsquid)+(i*dfieldarray))
        if impurities=='on':
            for i in range(nimpurities):
                shift[int((i+1)*n/nimpurities)-1]=(1+
                impuritymagnitude)
        self._shift=shift
        b=[]
        if betaarray.lower()=='off':
            dev=beta*betadeviation
            for i in range(n*narray):
                b.append(beta+dev*random.random())
        elif betaarray.lower()=='on':
            b=beta
        self._b=b
```

```
initialguessUP=[]
for i in range(n*narray):
    initialguessUP.append(mini)
PHIUP=[]
PHIDOWN=[]
phieUP=[]
phieDOWN=[]
indexesUP=[]
indexesDOWN=[]
phieb=np.linspace(mini,maxi,nsteps)
print 'Sweeping up '
for i in range(nsteps):
    phie=phieb[i]+phienoise*random.random()
    self._phie=phie
    phi=  fsolve(self.equation, (initialguessUP))
    if all([-errorcheck<x<errorcheck for x in
        self.equation(phi)]):
        PHIUP.append(phi)
        phieUP.append(phie)
        initialguessUP=(phi)
    else:
        try:
            phi=  broyden1(self.equation, (initialguessUP))
        except:
            pass
        if all([-errorcheck<x<errorcheck for x in
            self.equation(phi)]):
            PHIUP.append(phi)
            phieUP.append(phie)
```

```
                initialguessUP=(phi)
            else:
                indexesUP.append(i)
        if i % (nsteps/200.) == 0:
            stdout.write("\r%d" % int(100*i/nsteps)+
            '%␣Complete␣\r')
            stdout.flush()
    if sweep.lower()=='up':
        self._phiList=PHIUP
        self._phieList=phieUP
    else:
        print '\nSweeping␣down'
        initialguessDOWN=(initialguessUP)
        for i in range(nsteps):
            phie=(maxi-i*(maxi-mini)/nsteps+
            phienoise*random.random())
            self._phie=phie
            phi=  fsolve(self.equation, (initialguessDOWN))
            if all([-errorcheck<x<errorcheck for x in
                self.equation(phi)]):
                PHIDOWN.append(phi)
                initialguessDOWN=(phi)
                phieDOWN.append(phie)
            else:
                try:
                        phi=  broyden1(self.equation,
                        (initialguessDOWN))
                except:
                    pass
```

```
                    if all([-errorcheck<x<errorcheck for x in
                        self.equation(phi)]):
                        PHIDOWN.append(phi)
                        phieDOWN.append(phie)
                        initialguessDOWN=(phi)
                    else:
                        indexesDOWN.append(i)
                if i % (nsteps/200.) == 0:
                    stdout.write("\r%d" % int(100*i/nsteps)+
                    '% Complete \r')
                    stdout.flush()
                    stdout.write("\r%d" % int(100*i/nsteps)+
                    '% Complete \r')
                    stdout.flush()
            phiList=PHIUP+PHIDOWN
            phieList=phieUP+phieDOWN
            if len(PHIDOWN)==0:
                print 'Error: empty array'
                quit()
        if len(PHIUP)==0:
            print 'Error: empty array'
            quit()
        if sweep.lower()=='both':
            self._phiList=phiList
            self._phieList=phieList
        if sweep.lower()=='down':
            self._phiList=PHIDOWN
            self._phieList=phieDOWN
    def nonlinearity(self, invar):
```

```
        if self._junctiontype.lower()==('jj' or
        self._junctiontype.lower()=='josephson junction'):
            retvar=np.sin(invar)
        elif (self._junctiontype.lower()=='wl' or
        self._junctiontype.lower()=='weak link' or
              self._junctiontype.lower()=='nb' or
              self._junctiontype.lower()=='nanobridge'):
            retvar=np.cos(invar/2)*np.arctanh(np.sin(invar/2))
        return retvar


    def equation(self, phi):
        eq=[]
        for u in range(self._narray):
            eq.append((phi[self._n*u]+self._b[u*self._n]*
            self.nonlinearity(phi[u*self._n])-
            self._edgeInductor*self._a*(phi[(u*self._n)+1])-
            self._phie*self._shift[u*self._n]))
            if self._n>2:
                for x in range(self._n-2):
                    eq.append(phi[u*self._n+x+1]+
                    self._b[u*self._n+x+1]*
                    self.nonlinearity(phi[u*self._n+x+1])-
                    self._a*(phi[u*self._n+x])-
                    self._a*(phi[u*self._n+x+2])-
                    self._phie*self._shift[u*self._n+x+1])
            eq.append(phi[(u+1)*self._n-1]+
            self._b[((u+1)*self._n)-1]*
            self.nonlinearity(phi[(u+1)*self._n-1])-
            self._edgeInductor*self._a*(phi[(u+1)*self._n-2])-
```

```
            self._phie*self._shift[((u+1)*self._n)-1])
        return eq

    def magneticMoment(self):
        squid=np.linspace(-1,self._n*self._narray-1,
        self._n*self._narray+1)
        moment=[]
        for i in self._phiList:
            moment.append([np.sin(x) for x in i]+[0])
        return(moment,squid)

    def fres(self):
        phitot=[]
        for i in range(len(self._phiList)):
            phitot.append(sum(self._phiList[i]))
        f=(abs(np.diff(phitot)/np.diff(self._phieList))
        +self._Lr)**-0.5
        fx=[x/(2*np.pi) for x in self._phieList[0:-1]]
        return(fx,f)

    def internalFlux(self):
        phiei=[]
        phii=[]
        for i in np.transpose(self._phiList):
            phiei.append([x/(2*np.pi) for x in self._phieList])
            phii.append(i)
        return(phiei, phii)
```

Bibliography

[1] I. A. A. Alfaleh. *Engineering Superconducting Resonators for Quantum Circuits*. PhD thesis, Royal Holloway, University of London, September 2015.

[2] C. D. Shelly, P. See, J. Ireland, E. J. Romans, and J. M. Williams. Weak link nanobridges as single flux quantum elements. *Superconductor Science and Technology*, 30(9):095013, 2017.

[3] B. Ho Eom, P. K. Day, H. G. LeDuc, and J. Zmuidzinas. A wideband, low-noise superconducting amplifier with high dynamic range. *Nat Phys*, 8(8):623–627, 08 2012.

[4] A. L. Rakhmanov, A. M. Zagoskin, S. E. Savel'Ev, and F. Nori. Quantum metamaterials: Electromagnetic waves in a Josephson qubit line. *Phys. Rev. B*, 77(14):144507, April 2008.

[5] A. B. Zorin. Josephson traveling-wave parametric amplifier with three-wave mixing. *Phys. Rev. Applied*, 6:034006, Sep 2016.

[6] T. Mao and Z. D. Wang. Quantum simulation of topological majorana bound states and their universal quantum operations using charge-qubit arrays. *Phys. Rev. A*, 91:012336, Jan 2015.

[7] A. M. Zagoskin, D. Felbacq, and E. Rousseau. Quantum metamaterials in the microwave and optical ranges. *ArXiv e-prints*, January 2016.

[8] A. M. Zagoskin, R. D. Wilson, M. J. Everitt, S. E. Savel'ev, D. R. Gulevich, J. Allen, V. K. Dubrovich, and E. Il'ichev. Spatially resolved single photon detection with a quantum sensor array. *Scientific Reports*, 3:3464 EP –, 12 2013.

[9] M. Jerger, S. Poletto, P. Macha, U. Hübner, A. Lukashenko, E. Il'ichev, and A. V. Ustinov. Readout of a qubit array via a single transmission line. *EPL (Europhysics Letters)*, 96:40012, November 2011.

[10] H. Asai, S. Kawabata, A. M. Zagoskin, and S. E. Savel'ev. Quasi-Superradiant Soliton State of Matter in Quantum Metamaterials. *ArXiv e-prints*, May 2016.

[11] H. Asai, S. E. Savel'ev, S. Kawabata, and A. M. M. Zagoskin. Effects of lasing in a one-dimensional quantum metamaterial. *Phys. Rev. B*, 91:134513, Apr 2015.

[12] M. A. Nielsen and I. L. Chuang. *Quantum Computation and Quantum Information: 10th Anniversary Edition*. Cambridge University Press, New York, NY, USA, 10th edition, 2011.

[13] I. M. Georgescu, S. Ashhab, and F. Nori. Quantum simulation. *Rev. Mod. Phys.*, 86:153–185, Mar 2014.

[14] R. P. Feynman. Simulating physics with computers. *International Journal of Theoretical Physics*, 21(6):467–488, 1982.

[15] M. Caleap and B. W. Drinkwater. Metamaterials: supra -classical dynamic homogenization. *New Journal of Physics*, 17(12):123022, 2015.

[16] A. B. Zorin, M. Khabipov, J. Dietel, and R. Dolata. Traveling-wave parametric amplifier based on three-wave mixing in a josephson metamaterial. In *2017 16th International Superconductive Electronics Conference (ISEC)*, pages 1–3, June 2017.

[17] X. Zhou, V. Schmitt, P. Bertet, D. Vion, W. Wustmann, V. Shumeiko, and D. Esteve. High-gain weakly nonlinear flux-modulated josephson parametric amplifier using a squid array. *Phys. Rev. B*, 89:214517, Jun 2014.

[18] N. E. Frattini, V. V. Sivak, A. Lingenfelter, S. Shankar, and M. H. Devoret. Optimizing the Nonlinearity and Dissipation of a SNAIL Parametric Amplifier for Dynamic Range. *Physical Review Applied*, 10(5):054020, Nov 2018.

[19] T. Dixon, J. W. Dunstan, G. B. Long, J. M. Williams, P. J. Meeson, and C. D. Shelly. Capturing complex behaviour in josephson travelling wave parametric amplifiers, 2019.

[20] B. E. A. Saleh and M. C. Teich. *Fundamentals of Photonics*. Wiley Series in Pure and Applied Optics. Wiley, 2007.

[21] A. B. Zorin and Y. Makhlin. Period-doubling bifurcation readout for a josephson qubit. *Phys. Rev. B*, 83:224506, Jun 2011.

[22] M. T. Bell and A. Samolov. Traveling-Wave Parametric Amplifier Based on a Chain of Coupled Asymmetric SQUIDs. *Physical Review Applied*, 4(2):024014, August 2015.

[23] Y. Zolotaryuk and I. O. Starodub. Fluxon mobility in an asymmetric SQUID array. *ArXiv e-prints*, November 2014.

[24] T. Weißl, B. Küng, E. Dumur, A. K. Feofanov, I. Matei, C. Naud, O. Buisson, F. W. J. Hekking, and W. Guichard. Kerr coefficients of plasma resonances in josephson junction chains. *Phys. Rev. B*, 92:104508, Sep 2015.

[25] R. D. Bock, J. R. Phillips, H. S. J. van der Zant, and T. P. Orlando. Influence of induced magnetic fields on the static properties of one-dimensional parallel josephson-junction arrays. *Phys. Rev. B*, 49:10009–10012, Apr 1994.

[26] M. Tinkham. *Introduction to Superconductivity: Second Edition*. Dover Books on Physics. Dover Publications, 2004.

[27] B. D. Josephson. Possible new effects in superconductive tunnelling. *Physics Letters*, 1(7):251 – 253, 1962.

[28] O. Yaakobi, L. Friedland, C. Macklin, and I. Siddiqi. Parametric amplification in josephson junction embedded transmission lines. *Phys. Rev. B*, 87:144301, Apr 2013.

[29] N. Boulant, G. Ithier, P. J. Meeson, F. Nguyen, D. Vion, D. Esteve, I. Siddiqi, R. Vijay, C. Rigetti, F. Pierre, and M. H. Devoret. Quantum nondemolition readout using a josephson bifurcation amplifier. *Phys. Rev. B*, 76:014525, Jul 2007.

[30] R. Vijay, M. H. Devoret, and I. Siddiqi. Invited review article: The josephson bifurcation amplifier. *Review of Scientific Instruments*, 80(11), 2009.

[31] M. H. Devoret, A. Wallraff, and J. M. Martinis. Superconducting Qubits: A Short Review. *eprint arXiv:cond-mat/0411174*, November 2004.

[32] J. Clarke and F. K. Wilhelm. Superconducting quantum bits. *Nature*, 453(7198):1031–1042, 06 2008.

[33] E. A. Tholén, A. Ergül, K. Stannigel, C. Hutter, and D. B. Haviland. Parametric amplification with weak-link nonlinearity in superconducting microresonators. *Physica Scripta*, 2009(T137):014019, 2009.

[34] K. K. Likharev. Superconducting weak links. *Rev. Mod. Phys.*, 51:101–159, Jan 1979.

[35] E. M. Levenson-Falk, N. Antler, and I. Siddiqi. Dispersive nanoSQUID magnetometry. *Superconductor Science and Technology*, 29(11):113003, sep 2016.

[36] L. Hao. Quantum detection applications of NanoSQUIDs fabricated by focussed ion beam. *Journal of Physics: Conference Series*, 286:012013, mar 2011.

[37] R. Vijay, J. D. Sau, M. L. Cohen, and I. Siddiqi. Optimizing anharmonicity in nanoscale weak link josephson junction oscillators. *Phys. Rev. Lett.*, 103:087003, Aug 2009.

[38] O. W. Kennedy, J. Burnett, J. C. Fenton, N. G. N. Constantino, P. A. Warburton, J. J. L. Morton, and E. Dupont-Ferrier. Tunable Nb superconducting resonator based on a constriction nano-squid fabricated with a Ne focused ion beam. *Phys. Rev. Applied*, 11:014006, Jan 2019.

[39] I. O. Kulik and A. N. Omel'Yanchuk. Contribution to the microscopic theory of the Josephson effect in superconducting bridges. *ZhETF Pisma Redaktsiiu*, 21:216, February 1975.

[40] K. D. Usadel. Generalized diffusion equation for superconducting alloys. *Phys. Rev. Lett.*, 25:507–509, Aug 1970.

[41] Dibyendu Hazra. Nanobridge superconducting quantum interference devices: Beyond the josephson limit. *Phys. Rev. B*, 99:144505, Apr 2019.

[42] M. Faucher, T. Fournier, B. Pannetier, C. Thirion, W. Wernsdorfer, J. C. Villegier, and V. Bouchiat. Niobium and niobium nitride squids based on anodized nanobridges made with an atomic force microscope. *Physica C Superconductivity*, 368, 11 2001.

[43] A. Blois, S. Rozhko, L. Hao, J. C. Gallop, and E. J. Romans. Heat propagation models for superconducting nanobridges at millikelvin temperatures. *Superconductor Science and Technology*, 30(1):014003, 2017.

[44] J. Clarke and A. I. Braginski. *The SQUID Handbook: Fundamentals and Technology of SQUIDs and SQUID Systems*. Wiley, 2006.

[45] J. G. Park, A. T. Cayless, and P. A. de Groot. The inductances of RF SQUIDS and the period of their response to applied magnetic flux. *Journal of Physics D: Applied Physics*, 18(10):1949–1965, oct 1985.

[46] H. Weinstock. *SQUID Sensors, Fundamentals, Fabrication and Applications*. Nato Science Series E:. Springer Netherlands, 1 edition, January 1996.

[47] Q. Zhang, H. Wang, G. Li, X. Tang, J. Ren, W. Peng, and Z. Wang. Geometric dependence of washer inductance for nbn dc squids. *IEEE Transactions on Applied Superconductivity*, 28(7):1–4, Oct 2018.

[48] M. Hosoya, E. Goto, N. Shimizu, N. Miyamoto, and Y. Harada. Inductance calculation system for superconducting circuits. *IEEE Transactions on Magnetics*, 25(2):1111–1114, March 1989.

[49] M. Göppl, A. Fragner, M. Baur, R. Bianchetti, S. Filipp, J. M. Fink, P. J. Leek, G. Puebla, L. Steffen, and A. Wallraff. Coplanar waveguide resonators for circuit quantum electrodynamics. *Journal of Applied Physics*, 104(11):113904, 2008.

[50] H. A. Wheeler. Transmission-line properties of parallel strips separated by a dielectric sheet. *IEEE Transactions on Microwave Theory and Techniques*, 13(2):172–185, March 1965.

[51] C. P. Wen. Coplanar waveguide: A surface strip transmission line suitable for nonreciprocal gyromagnetic device applications. *IEEE Transactions on Microwave Theory and Techniques*, 17(12):1087–1090, December 1969.

[52] K. Watanabe, K. Yoshida, T. Aoki, and S. Kohjiro. Kinetic inductance of superconducting coplanar waveguides. *Japanese Journal of Applied Physics*, 33(Part 1, No. 10):5708–5712, oct 1994.

[53] U. Fano. Effects of configuration interaction on intensities and phase shifts. *Phys. Rev.*, 124:1866–1878, Dec 1961.

[54] B. Luk'yanchuk, N. I. Zheludev, S. A. Maier, N. J. Halas, P. Nordlander, H. Giessen, and C. T. Chong. The fano resonance in plasmonic nanostructures and metamaterials. *Nat Mater*, 9(9):707–715, 09 2010.

[55] M. Galli, S. L. Portalupi, M. Belotti, L. C. Andreani, L. O'Faolain, and T. F. Krauss. Light scattering and fano resonances in high-q photonic crystal nanocavities. *Applied Physics Letters*, 94(7), 2009.

[56] L. D. Landau and E. M. Lifshitz. *Mechanics*. Course of Theoretical Physics. Butterworth-Heinemann, third edition, 1976.

[57] E. A. Tholén. *Intermodulation in microresonators: for microwave amplification and nano-scale surface analysis.* PhD thesis, KTH School of Engineering Sciences, 2009.

[58] J. S. Hedges, M. J. Adams, B. F. Nicholson, and N. G. Chew. Power dependent effects observed for a superconducting stripline resonator. *Electronics Letters*, 26(14):977–979, July 1990.

[59] J. Fröhlich and T. Spencer. The kosterlitz-thouless transition in two-dimensional abelian spin systems and the coulomb gas. *Communications in Mathematical Physics*, 81(4):527–602, 1981.

[60] J. R. Kirtley, C. C. Tsuei, Ariando, H. J. H. Smilde, and H. Hilgenkamp. Antiferromagnetic ordering in arrays of superconducting π-rings. *Phys. Rev. B*, 72:214521, Dec 2005.

[61] M. Watanabe and D. B. Haviland. Quantum phase transition and coulomb blockade with one-dimensional squid arrays. *Journal of Physics and Chemistry of Solids*, 63(6–8):1307 – 1310, 2002. Proceedings of the 8th {ISSP} International Symposium.

[62] J. Johansson and D. B. Haviland. Random background charges and coulomb blockade in one-dimensional tunnel junction arrays. *Phys. Rev. B*, 63:014201, Dec 2000.

[63] A. Ergül, T. Weißl, J. R. Johansson, J. Lidmar, and D. B. Haviland. Spatial and temporal distribution of phase slips in josephson junction chains. *Scientific Reports*, 7(1):11447, 2017.

[64] D. B. Haviland, K. Andersson, P. Ågren, J. Johansson, V. Schöllmann, and M. Watanabe. Quantum phase transition in one-dimensional josephson junction arrays. *Physica C: Superconductivity*, 352(1):55 – 60, 2001.

[65] P. Delsing, C. D. Chen, D. B. Haviland, Y. Harada, and T. Claeson. Charge solitons and quantum fluctuations in two-dimensional arrays of small josephson junctions. *Phys. Rev. B*, 50:3959–3971, Aug 1994.

[66] C. D. Chen, P. Delsing, D. B. Haviland, Y. Harada, and T. Claeson. Flux flow and vortex tunneling in two-dimensional arrays of small josephson junctions. *Phys. Rev. B*, 54:9449–9457, Oct 1996.

[67] M. Watanabe, D. B. Haviland, and R. L. Kautz. Control of the electromagnetic environment for single josephson junctions using arrays of dc squids. *Superconductor Science and Technology*, 14(10):870, 2001.

[68] M. Watanabe and D. B. Haviland. Small-Capacitance Josephson Junctions: One-Dimensional Arrays and Single Junctions. *arXiv e-prints*, pages cond–mat/0301340, Jan 2003.

[69] K. E. Porsch. *Exploring the period doubling bifurcation in a superconducting resonator*. PhD thesis, Royal Holloway, University of London, 2017.

[70] A. B. Zorin. Private communication, 2015.

[71] G. Long. *Studies of phenomena arising from the non-linearity of the Josephson junction*. PhD thesis, Royal Holloway, University of London, September 2018.

[72] I. Siddiqi, R. Vijay, M. Metcalfe, E. Boaknin, L. Frunzio, R. J. Schoelkopf, and M. H. Devoret. Dispersive measurements of superconducting qubit coherence with a fast latching readout. *Phys. Rev. B*, 73:054510, Feb 2006.